The Ionomer-Catalyst Interfacial Interactions during Electrochemical CO_2 Reduction

An operando approach

Msc. Thesis

Charley Thomas Bakker

Delft University of Technology

TU Delft

The Ionomer-Catalyst Interfacial Interactions during Electrochemical CO_2 Reduction

An operando approach

by

Charley Thomas Bakker

to obtain the degree Master of Science,
in Sustainable Energy Technology,
at the Delft University of Technology,
to be defended publicly on Thursday July 7, 2022 at 10:30 AM.

Student number:	4557298	
Project duration:	November 3, 2021 – July 07, 2022	
Thesis committee:	Dr. T. Burdyny (MECS)	TU Delft, supervisor
	Prof. Dr. H. Geerlings (MECS)	TU Delft
	Dr. B. Bera (TP)	TU Delft
Daily Supervisors:	Dr. M. Li (MECS)	TU Delft
	ir. H.P. Iglesias van Montfort (MECS)	TU Delft

This thesis is confidential and cannot be made public until July 7, 2022.

TU Delft

Preface

Back in November 2021, when I started my master thesis at the Materials for Energy Conversion and Storage (MECS) group, I had no clue about electrochemical CO_2 reduction whatsoever. Luckily I had two excellent daily supervisors, Aaron and Hugo, who helped me along the way.

Aaron showed me how to do scientific work in general, from doing experiments to processing the data. Despite me losing almost every single part of his flow cell and its attributes, somehow Aaron remained patient and forgiving. Even when I broke his only reference electrode, and did not want to admit it, he still managed to remain calm. Aaron is an incredible educator, and really takes the time to teach his students. Thank you Aaron for all your hard work and assistance every time I needed it! Good luck with your next steps!

Hugo introduced me to the world of infrared spectroscopy. I did not have any prior knowledge or experience in this field, but Hugo made me comprehend the general working principles in just a few minutes time. Hugo is a very talented educator and was always available if I needed help (even with 2 other students that needed supervision). He guided me along the way, from sputtering crystals to making beautiful plots and so much more. Thank you Hugo for all your efforts during the last 8 months!

I want to thank Dr. Burdyny for granting me the opportunity to do my thesis at his group and for being my supervisor during the last 8 months. Also thank you for taking the time to discuss my project and brainstorming for new ideas during the halfway meeting!

Besides my supervisors, I want to thank Marcel Bus, Mark Sassenburg, Erdem Irtem, Bart Boshuizen, Joost Middelkoop, Herman Schreuders, Georgy Filonenko, and all the other PostDoc's, PhD's and techicians for their help and fun conversations during the coffee breaks.

I want express my gratitude to Prof. Geerlings, Dr. Bera and once again Dr. Burdyny for taking the time to be a part of my defense committee.

I also want to say a word of thanks to the other master and bachelor students at the MECS group. Thanks for all the laughs and conversations we shared and good luck with your next steps in your early careers!

And last but not least, I want to thank my girlfriend, mom and dad for listening to all my worries, frustrations, doubts and successes I had during the last 8 months. Your support was much needed!

Charley Thomas Bakker
Delft, June 2022

Abstract

Electrochemical CO_2 reduction (CO_2R) provides the opportunity to mitigate our fossil-carbon dependence, by using CO_2 as an alternative source to produce value-added chemicals. Especially multi-carbon (C_{2+}) products are industrially of high value and hence a promising candidate for CO_2R products. Copper is uniquely capable of producing these value-added C_{2+} products. Currently, the application of CO_2R technology is hampered by low selectivity and rates of C_{2+} products. Ionomers, or ion-conducting polymers, are used in the catalyst layer to optimize the local reaction environment. In particular Nafion, a cation exchange ionomer, has proven to promote C_{2+} formation, but the mechanism behind it remains unclear. For this thesis, we focused on elucidating the role of the Nafion ionomer in altering product distribution on copper. A planar Cu electrode was used, onto which the Nafion was drop-casted. Atomic force microscopy was used to observe the restructuring of the ionomer during CO_2R, while attenuated total reflection surface enhanced infrared spectroscopy (ATR-SEIRAS) enabled us to observe adsorbed chemical intermediate species during electrochemical CO_2R. Flow cell experiments were performed to study the effect of the ionomer on product distribution and activity. The addition of Nafion significantly increased formation towards ethylene, due to stabilization of the atop-CO intermediate. The ionomer layer underwent restructuring during CO_2R, where it is expected that the hydrophilic domain of the ionomer takes over the surface interactions from the hydrophobic backbone, due to electrowetting of the catalyst. With the insights gained in this thesis we elucidated the interactions between the ionomer and catalyst during electrochemical CO_2R, which relates to the fundamental understanding required for designing advanced catalyst layers in the gas diffusion electrode.

Contents

Preface ii

Abstract iv

Nomenclature viii

List of Figures 1

List of Tables 5

1 Introduction 6

2 Literature Review 10
2.1 Working Principles of Electrochemical CO_2R . . . 10
2.1.1 Electrolyte . . . 11
2.1.2 Flow Cell Configurations . . . 12
2.1.3 Performance metrics . . . 13
2.1.4 Thermodynamics . . . 14
2.1.5 Anode Reactions . . . 15
2.1.6 Cathode reactions . . . 16
2.1.7 CO_2R products . . . 18
2.1.8 Membranes for CO_2R . . . 18
2.1.9 Electrode structures . . . 19
2.2 Copper catalyst . . . 22
2.2.1 Unique electrocatalytic property . . . 22
2.2.2 CO_2R reaction mechanisms on Cu . . . 23
2.3 Ionomers in CO_2R . . . 25
2.3.1 Application of ionomers in CO_2R . . . 25
2.3.2 Anion Exchange ionomers incorporated into catalyst layer . . . 25
2.3.3 Perfluorinated sulfonic-acid ionomers . . . 26
2.3.4 Phase-Separated Morphology of PFSA ionomers . . . 27
2.3.5 Chemical-mechanical energy balance of PFSA ionomers . . . 28
2.3.6 Proton Transfer Mechanism in PFSA Ionomers . . . 29
2.3.7 PFSA thin films . . . 30
2.3.8 Dispersion and adsorption characteristics of PFSA ionomers . . . 31
2.3.9 Application of Nafion in CO_2R Electrolyzers . . . 31

3 Materials and Methods 35
3.1 Electrochemical CO_2R experiment . . . 35
3.1.1 Electrochemical impedance spectroscopy . . . 36
3.1.2 Chronoamperometry . . . 37
3.1.3 Capacitance measurements . . . 37
3.2 Gaseous products analysis . . . 37
3.3 Liquid products analysis . . . 37
3.4 Catalyst preparation . . . 38
3.5 Drop-casting ionomer . . . 38
3.6 In-situ Atomic Force Microscopy . . . 39
3.7 ATR SEIRAS . . . 40
3.8 XPS . . . 41

4 Results and Discussion **42**
4.1 Elucidating ionomer morphology . . . 42
4.1.1 Ionomer morphology of different loadings . . . 42
4.1.2 Effect of solvent on morphology of Nafion film . . . 44
4.1.3 The evolution of bare copper surface under electrochemical conditioning . . . 44
4.1.4 Electrolyte effect on ionomer morphology . . . 45
4.1.5 Ionomer restructuring during CO2R . . . 47
4.2 Effect of ionomer on local reaction environment . . . 49
4.2.1 Nafion enhancing CO adsorption on Cu . . . 49
4.2.2 Intermediate and carbonate region . . . 51
4.3 Effect of the Nafion thin film on activity and selectivity . . . 53
4.3.1 CO, C_2H_4 and CH_4 product distribution . . . 53
4.3.2 H_2 and $HCOO^-$ product distribution . . . 54
4.4 Intrinsic activities . . . 55
4.5 Chemical composition analysis . . . 56
4.6 Relative double layer capacitance . . . 57

5 Conclusion **59**
5.1 Recommendations . . . 62

References **67**

6 Appendix **68**
6.1 NMR spectra . . . 68
6.2 XPS . . . 68
6.3 Cyclic voltammetry . . . 68
6.4 EIS measurements . . . 69

Nomenclature

Abbreviations

Abbreviation	Definition
PFSA	Perfluorinated sulfonic-acid
PEM	Polymer electrolyte membrane
CO_2R	Carbon dioxide reduction
IPCC	Intergovernmental Panel on Climate Change
CCS	Carbon capture and storage
CCU	Carbon capture and utilization
GDE	Gas diffusion electrode
C_{2+}	Multi carbon compounds
*CO	Chemisorbed CO
AEM	Anion exchange membrane
CEM	Cation exchange membrane
MEA	Membrane electrode assembly
BPM	Bipolar membrane
HER	Hydrogen evolution reaction
SHE	Standard hydrogen electrode
Ag/AgCl	Silver silver-chloride
RHE	Reversible hydrogen electrode
CL	Catalyst layer
MPL	Microporous layer
MPS	Microporous substrate
GDL	Gas diffusion layer
PTFE	polytetrafluoroethylene
PVC	Polyvinylchloride
DFT	Density functional theory
TEM	transmission electron microscopy
XPS	X-ray photospectroscopy
EW	Equivalent weight
QAPPT	quaternary ammonium poly(N-methyl-piperidine-cop-terphenyl)
QNM	Quantitative Nanoscale Mechanical
FTIR	Fourier Transform Infrared
AFM	Atomic Force Microscopy
HPLC	High-performance liquid chromatography
NMR	Nuclear magnetic resonance
ATR SEIRAS	Attenuated total reflectance surface enhanced infrared spectroscopy
EDTA	Ethylenediaminetetraacetic acid
Sccm	standard cubic centimeters per minute
EIS	Electrical impedance spectroscopy
MeOH	Methanol
IPA	Iso-propanol
GISAXS	Grazing-incidence X-ray scattering
ECSA	Electrochemical surface area

Symbols

Symbol	Definition	Unit
FE	Faradaic efficiency	[%]
R_u	Uncompensated resistance	Ohm]
j	Current density	A m^{-2}
α	Charge transfer coefficient	-
η	Activation overpotential	V
$R_{subscript}$	Resistance overpotential	Ohm
ΔG_f^o	Gibbs free energy	kJ mol^{-1}
ΔH_f^o	Enthalpy of formation	kJ mol^{-1}
ΔS_f^o	Enthalpy of formation	kJ mol^{-1} K^{-1}
C	Capacitance	Farad
Q	Charge	Coulombs
E	Potential	Volts
I	Current	Ampere
c	Concentration	ppm
z	Number of electrons	-
V	Volume	m^3
P	Pressure	Pascal
R	Universal gas constant	m^3 Pa mol^{-1} K^{-1}
T	Temperature	Kelvin
F	Faraday Constant	Coulomb mol^{-1}
M_w	Molecular weight	g mol^{-1}
ρ	Density	g mL^{-1}
R_a	Average roughness	nm
P_{gas}	Permeability of gas	mol cm^{-1} s^{-1}
S_{gas}	Solubility of gas	mol cm^{-1} s^{-1}
D_{gas}	Diffusion coefficient gas	cm^2 s^{-1}

List of Figures

1.1 Comparison of temperature variation from real data vs simulated situation with only natural influences. Period from 1850-2020. Reproduced from IPCC [2] 6
1.2 Oxidation state of single-carbon molecules. As highly reduced single-carbon molecules are oxidized (burned) energy is generally released. By means of electro-reduction the highly oxidized forms of carbon can be upgraded to higher energetic molecules, or highly reduced states. 7

2.1 Basic principle of CO_2R. The anode (+) is where water is converted into oxygen, the cathode (-) where carbon dioxide and protons are converted into products, the membrane through which ions can be transferred, the electrolyte consisting of solvent and ions. The anode and cathode are connected to an external power source. 11
2.2 This figure shows aqueous flow cell configurations. The numbers in figures refer to 1) cathode, 2) anode, 3) membrane, 4) anolyte, 5) catholyte. Sub-figure 'a' is a configuration in which CO_2 is first saturated in the catholyte before it enters the electrolyzer, typically by bubbling CO_2 gas. Here CO_2 diffuses from the flowing bulk catholyte to the catalytic surface. Sub-figures c,b and d are based gas-fed CO_2 systems, which requires a gas diffusion electrode. Reproduced from Garg *et al.* [10]. 13
2.3 Categorized metal groups for CO_2 reduction, where yellow is most selective for formate production, green for carbon monoxide, blue for hydrogen and red for aldehydes, alcohols and hydrocarbons products. 16
2.4 Reproduced from Nitopi *et al.* [16]. 18
2.5 Schematic representation of a typical GDE used in CO_2R. The current collector contains flow channels, which are indicated by the white rectangles. 19
2.6 This figures illustrates how CO_2R is fundamentally different for planar and GDE electrodes. a) proton concentration as function of current density. b) shows how the concentration of CO_2 depletes faster in a H-cell compared to a GDE. c) shows pH as function of current density. d) H-cell type of CO_2 diffusion mechanism. e) GDE diffusion mechanism of CO_2. Reproduced from Burdyny & Smith [17]. 20
2.7 a) Binding energy of CO* and H* reaction intermediates with various metals. Reproduced from Bagger et al. [36]. b) Partial current density and faradaic efficiency of copper as a function of the cathodic potential tested in a H-cell. Reproduced from Peterson et al. [37] 22

2.8 Reaction pathways to common products of CO_2R with copper. Blue arrows lead to formation of either CO or CH_4, orange and purple arrows to $CHOO^-$, black arrows to CH_3OH, gray arrows to C_2H_4 and green arrows to C_2H_5OH. Section a) pathways of CO_2 to single-carbon products. b) pathways to multi-carbon products, c) pathway of CO_2 insertion into metal-H bond to formate. Reproduced from [38] 23
2.9 a) Sustainion, b) QAPPT. Reproduced from Salvatore *et al.* [26]. 26
2.10 Three common PFSA ionomers. Reproduced from Shin *et al.* [48] 27
2.11 a) This figure illustrates how the phase-separated morphology segregates the hydrophilic and hydrophobic regions. The hydrophilic region is made up of a network of hydrogen bonded molecules. The negative charge on the sulfonate side group enables cation-exchange through this region. b) PFSA ionomer phase-separated morphology with a hydrophobic backbone and hydrophilic side chain. 27
2.12 a) This figure shows how the water content depends on the water activity. The water activity is defined as 0 when there is no water present, while a water activity of 1 defines a maximum absorption of water. As swelling increases, a fraction of water is so-called bound water and not mobile, while another fraction is free water and able to dynamically move. The swelling is associated with an deformation of the ionomer matrix. b) This figure shows two transfer mechanisms, the first being vehicular motion of molecules at dominant at low hydration. The other transport mechanism is structurally based, sometimes referred to as Grotthuss hopping and dominant at high hydration. Reproduced from Kusoglu & Weber [47]. 29
2.13 a) Orientation of Nafion thin and ultra thin films on hydrophilic or metallic substrates [47]. b) Nano-domain and molecular orientation driven by confinement [61]. 30
2.14 This figure shows the surface morphology of Nafion thin films on SiO_2 substrates, produced by self-assembly. Nafion was dispersed in a combination of water and iso-propanol. Reproduced from [62]. 31
2.15 This figures illustrates the enhancing effect of COR and CO_2R of a ionomer thin film on Cu (CIPH, catalyst:ionomer planar heterojunction), applied in a GDE. a) shows the increased partial current density of Cu COR towards ethylene. b) shows the increased summed partial current density towards carbon monoxide and ethylene on Cu catalyst. c) without CIPH, d) with CIPH. Reproduced from de Arquer *et al.* [8]. 32
2.16 This figure shows the effect of cations and Nafion thin films on CO_2R. a) FE and CD of Naf1100/Cu + Cs+, b) FE and CD of bare Cu + Li+, c) FE and CD of Naf1100/Cu + Cs+, d) FE and CD of bare Cu + Cs+. e) Comparison of water concentrations of bare and ionomer coated catalysts, f) comparison of CO_2R performance of Nafion coated samples. g) Summary of the effects of thin films and pulsed electrolysis. Reproduced from Kim *et al.* [6]. 33

3.1 a) Exploded-view drawing of the CO_2R flow cell. 1, 13: stainless steel endplates. 2,8: PTFE flow chambers. 3,5,7,10,12: gaskets. 4: nickel-mesh anode. 6: nafion-115 membrane. 9: Ag/AgCl reference electrode. 11: copper cathode + stainless steel current collector. b) This schematic illustrates the flow cell configuration. 36
3.2 Experimental setup used for flow cell CO_2R experiments. This aqueous-based system pumped the electrolyte at a 20 mL/min rate, and continuously bubbled 10 sccm CO_2 into the catholyte. The gas-tight catholyte was connected to a liquid-trap, which was connected to a GC. 36
3.3 Setup for in-situ electrochemical AFM. 39
3.4 a) ATR SEIRAS experimental setup. b) Germanium crystal with a 40 nm thin layer of copper. 40

4.1 AFM images of ionomer on copper. a) bare copper, b) 0.05wt%, c) 0.1wt%, d) 1wt% , e) 5wt% ionomer. The density of dry Nafion: 2.05 g cm^{-3} [68]. The estimated film thicknesses were b) 38 nm, c) 77 nm, d) 770 nm, e) 4170 nm. Propanol was used as the solvent. Image size 5x5 micrometer. 43
4.2 AFM height images of bare copper and drop-casted 0.1wt% Nafion dispersions on copper in methanol and iso-propanol solvent. The average roughness from left to right: 1.5, 2.2, 5.3 nm. Image size 1x1 µm. Height images made with ScanAsyst Fluid+ AFM probes in 0.1 M $KHCO_3$ electrolyte. Note that these were different spots, on the same sample. The general features are however representative. 44
4.3 This time sequence shows the same location on a bare copper sample under negative conditioning. Image size is 5x5 micrometer. A constant current of 2.85 mA cm^{-2} was applied. 45
4.4 In situ AFM scans of bare copper coated with ionomer. The red squares are zoomed-in in figure 4.5. Average roughness Ra for bare copper = 12 nm, Nafion coated = 10.3 nm, Nafion coated + 0.1M $KHCO_3$ = 10.3 nm, Nafion coated + 0.1M $KHCO_3$ after 30 min = 12.1 nm, Nafion coated + 0.1M $KHCO_3$ after 60 min = 11.3 nm, Nafion coated + 0.1M $KHCO_3$ after 7 min = 11 nm. Bare and Nafion scans were made with ScanAsyst Air probe, the other scans with ScanAsyst Fluid+ probe. 46
4.5 Swelling model for Nafion. These images are zoomed selections of the scans in figure 4.4. The feature indicated by 33 nm is with respect to its base. 46
4.6 In-situ AFM images of ionomer-coated copper after applying constant current. 0.1 M $KHCO_3$ electrolyte, saturated with CO_2 was used. Red squares indicates the area over which the average roughness Ra, respectively 19.7 and 13.7 nm from left to right. was determined. Ionomer loading was 8 µg cm^{-2}, constant current of 2.85 mA cm^{-2} was applied. ScanAsyst Fluid+ probe was used. 47

4.7 Time sequence of Nafion morphology on copper. The image size for the top row is 5x5 µm, the bottom row is 1x1 µm. Average roughness of the bottom row from left to right: 10.3, 17.6, 9.83, 8.66 nm. The Nafion loading was 8 µg cm^{-2}. A constant current of 2.85 mA cm^{-2} was applied. 48
4.8 Left: Absorbance spectrum of Nafion coated Cu during CO_2R. Right: Absorbance spectrum of bare Cu. A 40 nm layer of copper was sputtered on a germanium crystal. 49
4.9 Absorbance heatmaps of Nafion coated copper (a) and bare copper (b). 51
4.10 ATR SEIRAS spectra of common carbonate intermediates region during CO_2R. Left: ionomer coated copper, Right: bare copper. 52
4.11 Accumulated faradaic efficiencies per potential for ionomer-coated (left) and bare copper (right). Note that the potential on the x-axis is spaced evenly, which is not the actual spacing. 53
4.12 Faradaic efficiencies and partial current densities towards carbon monoxide (column a), ethylene (column b) and methane (column c). 54
4.13 Faradaic efficiencies and partial current densities of hydrogen (column a) and formate (column b). 55
4.14 Intrinsic activities of a) hydrogen, b) carbon monoxide, c) methane, d) ethylene, e) formate. 55
4.15 Comparison between atomic ratio's of Naf/Cu samples before and after experimental work. Chronoamperometry was performed at 4 potentials, each with a duration of 1800 sec. The data of four Naf/Cu samples were averaged in this analysis, each evaluated at three different spots of 400 µm in diameter. In appendix 6.2, two XPS survey spectra shown as example. 56
4.16 a) Bare Cu positive current vs scan rate (mV s^{-1}) for. b) Naf/Cu positive current vs scan rate (mV s^{-1}). 57

5.1 a) This figure shows how the ionomer limits CO permeability, which could lead to re-adsorption of CO. b) Case for bare copper 60
5.2 a) This figure shows how an increased cation concentration could stabilize the *CO. b) Case for bare copper. 61
5.3 a) illustrates the proposed stabilization of Nafion of *CO intermediate with dipole-dipole bonds. b) Shows how bare copper results in a lower activity towards CO, C_2H_4 and CH_4. 61

6.1 NMR spectra 68
6.2 XPS surveys 68
6.3 Cyclic voltammetry averaged for bare and the ionomer coated copper. 69
6.4 EIS measurement. Solution resistances were typically between 15 and 25 ohms, both both Naf/Cu as well as 69

List of Tables

2.1 Anodic reactions in aqueous media. Standard electrode potentials E^0 evaluated at pH = 0. 16
2.2 This table shows common C1-C3 CO_2 reduction reactions. The potentials are calculated using the Gibbs free energy, using tabulated data from Engel [20], calculated at pH = 0. 17
2.3 List of references where the effect of the ionomer was investigated. The description of the catalyst indicates if it is an ionomer film (planar) or catalyst ink (GDE). Noticeably, Nafion is the most common entry. 25

4.1 This table shows the capacitance of bare Cu and Naf/Cu before and after 1 hour chronoamperometry at -1.9V vs Ag/AgCl reference electrode. 58

5.1 Comparison of product distribution on bare Cu and Naf/Cu. 62

1

Introduction

As modern society is technologically advancing, our material and energy dependence on fossil carbon remains. In 2019, there was a globally average dependence of 80.2% on fossil fuels [1]. The anthropogenic carbon dioxide emissions from burning fossil fuels causes an enhanced greenhouse gas effect. While carbon dioxide is not the only contributing greenhouse gas, the sixth assessment report from the Intergovernmental Panel on Climate Change (IPCC), inline with the current scientific consensus, is clear about the the contribution of carbon dioxide to global warming: carbon dioxide is the major greenhouse gas that is inducing this climate change.According to the IPCC, humankind is largely responsible for this as can be seen in figure 1.1.

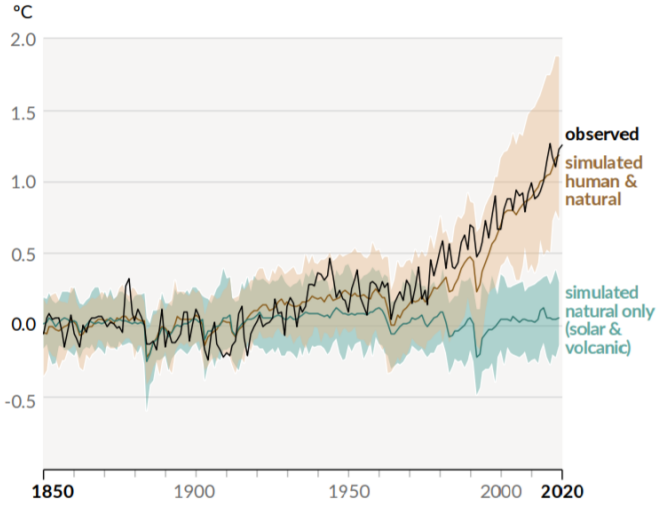

Figure 1.1: Comparison of temperature variation from real data vs simulated situation with only natural influences. Period from 1850-2020. Reproduced from IPCC [2]

From the period of 1850-1900, the global temperature has increased 1.06 °C till the period of 2010-2019. Of that increase carbon dioxide had the largest share, a contribution of +0.79 °C, among all atmospheric gases and aerosols [2]. Many countries have committed via climate agreements to reduce their CO_2 emissions with respect to 1990 levels, to limit the global warming to a relatively safe level of 1.5 °C above pre-industrial levels.

The first step in achieving these monumental goals, is to decarbonize society, so there is no net increase of anthropogenic carbon dioxide in the atmosphere. Beyond global decarbonization, atmospheric carbon dioxide concentration can be decreased by Carbon Dioxide Removal. Here, carbon dioxide can be extracted from the atmosphere via a natural way using afforestation, or by means of technology that separates carbon dioxide from the other constituents in the atmosphere and sequester it, typically underground. However, many critical industries for producing plastics, textiles, paints, detergents, lubricants, and many more products require some sort of carbon feedstock. These industries currently rely on fossil-carbon, and with decarbonization of society, they should inevitably become fossil-carbon independent. To keep our standard of living, an alternative source of carbon should be used. Carbon Capture and Utilization (CCU) provides a solution to this problem, and in addition helps to mitigate global warming. With CCU, carbon dioxide is purposefully utilized for production of critical materials, chemicals or fuels.

When carbon containing sources like fossil fuels or biomass are burned, the organic compounds are converted towards more oxidized states which releases the energy that we utilize. Figure 1.2 shows the relative oxidation states of several single-carbon forms. While CO_2 is the most oxidized form of carbon (oxidation state of +4), i.e. very stable under atmospheric conditions, with sufficient driving force and the right conditions, CO_2 is possible to be valorized into more energetic products via CO_2 reduction (CO_2R). This reduction can be electrochemically driven, using a voltage, which is called electrochemical CO_2R. Besides electrons, protons are also required to to convert CO_2. Water can provide the reaction environment for CO_2R and is easy to access, so aqueous solutions are most often used as electrolyte solvent for CO_2R.

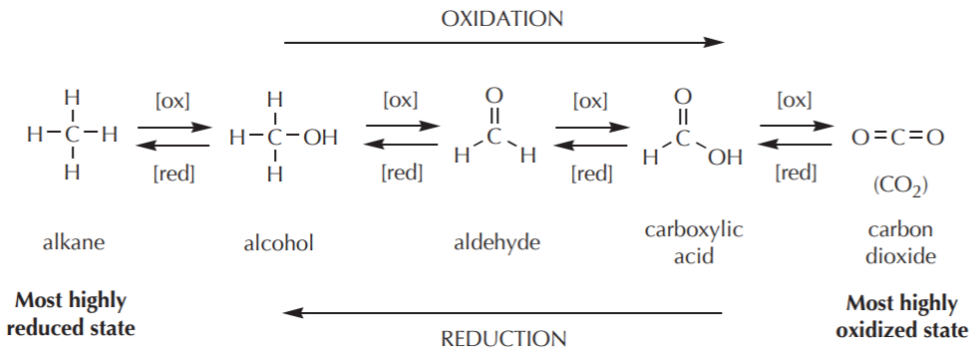

Figure 1.2: Oxidation state of single-carbon molecules. As highly reduced single-carbon molecules are oxidized (burned) energy is generally released. By means of electro-reduction the highly oxidized forms of carbon can be upgraded to higher energetic molecules, or highly reduced states.

Due to recent scientific advances, carbon capture and utilization technology has experienced considerable progress [3]. Besides, the cost of sustainable energy is declining ever still [1]. Electrochemical CO_2R enables to utilize atmospheric CO_2 as an alternative to our dependency on fossilized carbon. This relatively new technology has yet to be commercialized. Lees *et al.* [4] reported that commercially viable electrolyzers should operate at industrially relevant current densities (J > 200 mA/cm2), high Faradaic efficiencies (FE > 80%) and low cell potentials (E < 3 V), for about 20 years [5].

Issues like low product selectivity and activity should be solved to lift this technology to a higher technology readiness level. This can be achieved by means of optimized electrolyzer and electrode design, better catalyst materials, or modification of the catalyst layer. It is widely accepted by the scientific community, that the employment of the gas diffusion electrode is paramount for successfully reaching the industrial aims. The gas diffusion electrode enables a much more efficient CO_2 supply than its predecessors like the planar and porous electrodes, which results in significantly higher rates of CO_2R. Part of the catalyst layer of GDE in CO_2R electrolyzers, are so-called ionomers. Ionomers are ion-conducting polymers that are added to the catalyst layer to immobilize the catalyst and modify the local reaction environment around the catalyst. Since the local reaction environment, among other factors, determines the formation of products, the ionomer has a significant effect on the selectivity and activity of CO_2R reactions. Multi-carbon products like ethylene and ethanol are widely-used and valuable chemicals, hence are promising candidates for economically attractive CO_2R. While there is evidence pointing towards the CO_2R promoting effects of ionomers towards C_{2+} products [6–8], a convincing scientific explanation is lacking. Fundamental studies on the ionomer-catalyst interactions are essential to gain insights into the highly complex interactions of GDE-based high-current densities systems, hence the motivation behind this thesis.

Objectives

This thesis aims to elucidate the ionomer-catalyst interfacial interactions, and its effect on CO_2R reactions. The effect of the ionomer on product distribution, will be investigated using a multifaceted experimental approach. The following research questions will be addressed:

- How does the surface morphology of a Nafion ionomer on Cu change under a negative applied potential?
- How does the ionomer influence formation of chemical intermediate species during electrochemical CO_2R?
- How does the ionomer alter the product distribution?

Approach

Understanding the role of ionomer-catalyst interactions is essential to guide the design of an optimal catalyst layer for stable CO_2R at high current density. With the employment of powerful operando techniques, i.e. operando electrochemical atomic force microscopy (AFM) and ATR surface-enhanced infrared spectroscopy (ATR-SEIRAS), this thesis aims at eludicating the ionomer-catalyst interactions by examining the chemical interface (copper-Nafion) and morphological evolution of the ionomer surface during the CO_2R conditions. In addition, the effect of the ionomer on activity and selectivity is investigated by CO_2R experiments in a flow cell.

Scope

While a better understanding of the ionomer-catalyst interfacial interactions is ultimately of great importance to the GDE, a planar electrode design was chosen, because i) it allows for studying the ionomer-catalyst interactions and CO_2R effects, without introducing additional complexities like flooding and salt precipitation related to GDEs, ii) enables to study the same interface with CO_2R experiments, operando infrared spectroscopy and in-situ atomic force microscopy. We choose to study one catalyst, polycrystalline copper, and one ionomer, Nafion.

Structure of thesis

This thesis provides an elaborate literature review (chapter 2) about the working principles of CO_2R, the unique electrocatalytic property of copper and an overview of the use of ionomers in CO_2R technology. Secondly in chapter 3 the materials and methods will be described. In chapter 4 the results will be presented along with a discussion. Finally, in chapter 5 the conclusion of this research will be given.

2

Literature Review

This review provides an explanation of the general working principles of the overarching technology in this thesis; electrochemical CO_2 reduction (chapter 2.1). In chapter 2.2.1 the unique electrocatalytic property of copper is described. The last chapter 2.3, provides the reader the current state-of-the-art of ionomers in CO_2R research.

2.1. Working Principles of Electrochemical CO_2R

In CO_2 electrolyzers, carbon dioxide is converted into value-added products, such as ethylene, ethanol, and carbon monoxide. In the presence of a catalyst and appropriate reaction conditions, carbon dioxide gains electrons, which is called a reduction reaction - this side is called the cathode. At the other side of the electrolyzer, the oxidation reaction takes place at the anode. The electrolyte and the ion-exchange membrane transfers ions between both sides. Since the reactions at both sides are non-spontaneous, an external voltage is required to drive the reactions. This external voltage should be generated by renewable power sources, for the technology to be considered carbon-neutral. A schematic of the basic principle of CO_2R is shown in figure 2.1.

Oxidation reactions at the solid-liquid interface around the anode, release electrons from electrochemically active species. The electrons released at the anode are conducted through an external circuit towards the cathode, where they react with CO_2. The electrodes are made of catalyst material, which lower the kinetic barrier of certain reaction. While the reaction conditions like temperature, pressure and concentrations can shift the thermodynamic equilibrium of the reaction according to Le Chatelier's principle [9], the applied potential and the type of catalyst can only change the rate of the

reactions towards the thermodynamic equilibrium.

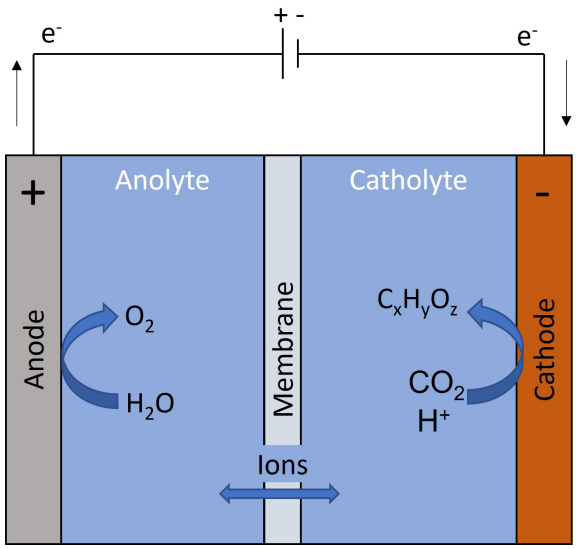

Figure 2.1: Basic principle of CO_2R. The anode (+) is where water is converted into oxygen, the cathode (-) where carbon dioxide and protons are converted into products, the membrane through which ions can be transferred, the electrolyte consisting of solvent and ions. The anode and cathode are connected to an external power source.

2.1.1. Electrolyte

Within the realm of liquid electrolytes, the electrolyte generally consists of three components, the electrolyte or salt, the solvent and the electrochemically active species (CO_2). The electrolyte should have (1) a high solubility for the reactant (CO_2), (2) good conductivity of ions, (3) electrochemically stable and compatible with the electrode material, (4) low viscosity to allow for good rates of CO_2 mass transfer and (5) be safe to handle and store [10]. Typically water is used as a solvent for the electrolyte, because it sufficiently satisfies the aforementioned properties and on top of that can act as a proton donor to supply protons for CO_2R. Two widely used electrolytes for CO_2R are bicarbonates (HCO_3^-) and hydroxides (OH^-). Other aqueous electrolytes include borate salts [11], halides [12], phosphates [13] and sulfates [14].

It should be mentioned that the (counter)ions of the electrolyte are not merely balancing charge carriers, but also have interactions with other species present in the solution, can be a reactant, and interact with the catalyst to form the electrical double layer. For example hydroxides are oxidized at the anode, and bicarbonates form an equilibrium with carbon dioxide and carbonates. Cations are part of the electrical double layer at the cathode interface, where identity and the size of these cations influence the reaction itself [15].

The solubility of CO_2 in aqueous solutions is relatively low (c = 34 mM at room temperature) [16]. Steady conversion of CO_2 into hydrocarbons becomes mass transport limited as current density is increased. Increasing current densities eventually depletes dissolved carbon dioxide at the active sites faster than the CO_2 can be resupplied from the bulk. Reported mass transport limited current densities

for aqueous-fed systems are 35 mA cm^{-2} and 100 mA cm^{-2} for C_1 and C_2 products, respectively [17].

$KHCO_3$ is one of the most commonly reported aqueous inorganic salt electrolytes for CO_2R. In the 1950s CO_2 was captured by using hot solutions (+100 °C) of potassium carbonate (K_2CO_3) [18]. By swinging the pressure back and forth, CO_2 was absorbed and desorped by the the carbonate solution, in which $KHCO_3$ was formed. Later, $KHCO_3$ was used as electrolyte for CO_2. When $KHCO_3$ is added to water, it forms an bicarbonate buffer, where HCO_3^- is in equilibrium with CO_2 according to equation 2.1.

$$CO_2(g) + H_2O \rightleftharpoons CO_2(aq) + H_2O \rightleftharpoons H_2CO_3 \rightleftharpoons HCO_3^- + H^+ \tag{2.1}$$

Although there are other aqueous solutions, like amine solutions, which have a higher solubility for CO_2 [19], $KHCO_3$ has the benefit of large scale availability and low cost, and is easy to handle, store and prepare. Another benefit of $KHCO_3$ is that it is compatible with most electrode materials, which other electrolytes like sulfides, sulfates and halides often lack. At low electrolyte concentrations (< 0.1 M $KHCO_3$), the weak buffering capacity causes the pH of the electrolyte near the reaction surface to quickly rise and thereby favoring C_{2+}-products to form and suppress H_2 and CH_4 product formation [10].

2.1.2. Flow Cell Configurations

CO_2R electrolyzers are either liquid- or gas-fed. Figure 2.2 shows several types of flow cells. Figure 2.2a and b are liquid-fed, meaning the catholyte is flowing through the cell. The CO_2 can be supplied by the flowing catholyte, in which CO_2 is saturated outside the electrolyzer by bubbling CO_2 through the solution. However with a more integrated design CO_2 can be supplied in gaseous form, where you would use a gas diffusion electrode (figure 2.2b,c,d). By employing this type of electrode researchers have been able to drastically increase the current densities of CO_2R. This electrode type can be used in both liquid-fed (figure 2.2b), as well as in vapor-fed electrolyzers (figure 2.2c and 2.2d).

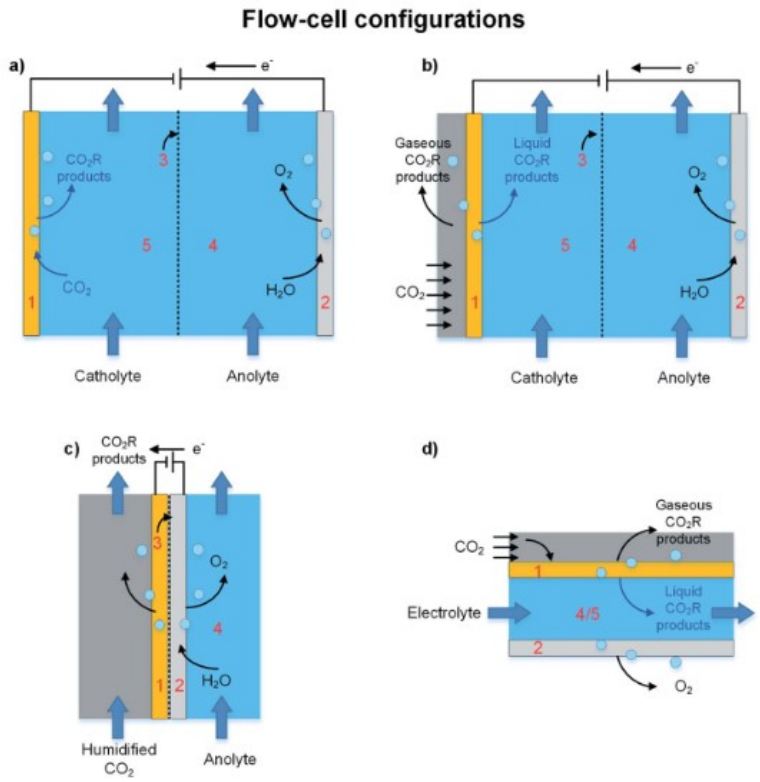

Figure 2.2: This figure shows aqueous flow cell configurations. The numbers in figures refer to 1) cathode, 2) anode, 3) membrane, 4) anolyte, 5) catholyte. Sub-figure 'a' is a configuration in which CO_2 is first saturated in the catholyte before it enters the electrolyzer, typically by bubbling CO_2 gas. Here CO_2 diffuses from the flowing bulk catholyte to the catalytic surface. Sub-figures c,b and d are based gas-fed CO_2 systems, which requires a gas diffusion electrode. Reproduced from Garg *et al.* [10].

2.1.3. Performance metrics

The rate at which the reactions proceed in electrochemistry is synonymous with current, expressed in Amperes. The current divided by the geometric area of the electrode is called the current density, where the partial current density indicates how much of that total current is consumed for a specific product. The faradaic efficiency is the amount of current that is consumed by a product, divided by the total current consumed by all reactions and multiplied by 100% to get percentages. The current density depends on the energy supplied to the system, or in other words the potential. The theoretical amount of energy/potential you need can be calculated using the Gibbs free energy change of the reaction. This is the minimal energy requirement of the reaction to proceed, and is given in units of Volts versus a specified reference reaction. The current and potential are related via the Butler-Volmer equation:

$$j = j_0 \cdot \left\{ exp\left[\frac{\alpha_a z F \eta}{RT}\right] - exp\left[\frac{\alpha_c z F \eta}{RT}\right] \right\} \tag{2.2}$$

where j is the electrode current density [A m^{-2}], j_0 exchange current density [A m^{-2}], T is temperate [K], z is number of electrons involved in the electrode reaction, F is Faraday constant, R is universal gas constant, α_c is the cathodic charge transfer coefficient [-], α_a is the anodic charge transfer coefficient

[-], η is the activation overpotential [V]. Besides the activation overpotential, there are other resistances that contribute to the total overpotential R_{total}. This overpotential equals the resistances summarized in the reaction below:

$$R_{total} = R_{cathode} + R_{anode} + R_{ions} + R_{membrane} + R_{bubble,cathode} + R_{bubble,anode} + R \tag{2.3}$$

$R_{cathode}$ and R_{anode} are the resistances of the activation overpotentials for CO_2R, R_{ions} are the ohmic losses due to conduction of ions, $R_{membrane}$ is the resistance of ion transport across the membrane, $R_{cathode\ and\ anode,\ bubbles}$ is the loss of active electrode area due to formation of bubbles, R is the sum of electrical resistances in the external circuit. The energy that is lost, indicated by the overpotential, does not contribute to the formation of the products.

2.1.4. Thermodynamics

The operation of CO_2 electrolyzers is a non-spontaneous process. This is denoted by a negative value standard cell potential E^o_{cell}, expressed in Volts vs a reference reaction. The ^{o} denotes standard state, meaning 25 °C and 1 bar of pressure. The standard hydrogen electrode (SHE) forms the basis of electrochemisty, as the reaction at this electrode (hydrogen evolution reaction) is arbitrarily set to 0 V. It enables to define the standard electrode potentials for other reactions, because they can be referenced to the SHE reaction (at 0 V). The redox reaction of the SHE reference, is defined at a platinized platinum electrode in an acidic solution of 1 M [H^+] and a pressure of the hydrogen gas of 1 bar [20].

The E^o_{cell} is calculated by the sum of the standard reduction potential $E^o_{reduction}$ and standard oxidation potential $E^o_{oxidation}$. The standard reduction and oxidation electrode potentials are calculated with the gibbs free energy of formation ΔG^o_f, which is defined as:

$$\Delta G^o_f = \Delta H^o_f - T\Delta S^o_f \tag{2.4}$$

where T the temperature, ΔH^o_f the standard enthalpy of formation [kJ mol^{-1}] and ΔS^o_f the standard entropy of formation [kJ $mol^{-1}K^{-1}$] can be experimentally measured. For a redox reaction, the standard gibbs free energy [kJ mol^{-1}] of the reaction $\Delta G^o_{f,reaction}$ is calculated by subtracting the ΔG^o_f of the of reactants from the products, both multiplied by their respective number of moles in the reaction. The $\Delta G^o_{f,reaction}$ is expressed in Joules, which can be converted to standard electrode potential E^o (in units V vs SHE) via the following formula:

$$\Delta G^o = -z \cdot F \cdot E^o \tag{2.5}$$

where z is the number of moles involved in the reaction, F is Faraday's constant. In practice when measuring the potential of the working or counter electrode, so called reference electrodes are used which have stable and well-known electrode potentials against SHE. Two examples are the saturated calomel electrode (SCE) and silver-silver chloride electrode. The SCE is a reference electrode that consists of a platinum wire inserted into a moist paste of liquid mercury (calomel; Hg_2Cl_2) and KCl. The silver-silver chloride (Ag/AgCl) reference electrode consists of a silver wire coated with a very thin layer of AgCl that is dipped into a chloride ion solution with a fixed concentration. The standard electrode potentials against SHE of these reference electrodes are well-known constants.

Another experimentally convenient scale for expressing the potential is called the reversible hydrogen electrode (RHE). It is defined as the potential of platinum in the solution of any pH value. To express another electrode reference like Ag/AgCl into an electrode potential in RHE scale, the pH should thus be known. For example when an Ag/AgCl reference electrode is used in an experiment:

$$E_{RHE} = E_{Ag/AgCl} + \frac{RT}{F} ln(10) \cdot pH + E^o_{Ag/AgCl} - I \cdot R_u \tag{2.6}$$

where $E_{Ag/AgCl}$ is the measured potential, the product multiplied by the pH is 0.059 [V pH^{-1}] at room temperature, $E^o_{Ag/AgCl}$ is the standard electrode potential against the SHE, I is the current and R_u is the uncompensated resistance. The $i \cdot R_u$ term represents the solution ohmic resistance between the reference and working electrode. At open circuit potential, the current between the reference and working electrode is usually very small, in the order of nA. This changes during operation, where there is a significant current flow between the reference and working electrode. Hence, the distance and electrolytic conductivity cause a potential drop, $i \cdot R_u$

2.1.5. Anode Reactions

During every electrochemical reaction, the oxidation and reduction proceed at the same rate. Therefore, the slowest reaction determines the rate of both, which is mathematically formulated by the Butler-Volmer equation 2.2. The type of oxidation reaction depends on the reaction conditions like electrolyte, catalyst, pH of solution and applied potential. Most flow cell configurations use an aqueous anolyte, examples of which can be seen in figure 2.2. Water oxidation products include oxygen, protons (acidic media) and water (alkaline media). Commonly used anolytes include hydroxides [21], while acidic electrolytes are less common [22]. Vass *et al.* [23] found that alkaline anolytes represent $\approx$ 62% of the inspected literature references form the last 5 years, $\approx$ 36% neutral anolytes and only $\approx$ 2% acidic media. Furthermore they found that the three most commonly used anode catalysts were in the order of Ir>Ni>Pt.

Table 2.1: Anodic reactions in aqueous media. Standard electrode potentials E^0 evaluated at pH = 0.

Reaction	E^0 (V vs RHE)	Product
$2\,H_2O(l) \longrightarrow 2\,O_2(g) + 4\,H^+ + 4\,e^-$	1.23	Oxygen + Protons
$4\,OH^-(aq) \longrightarrow O_2(g) + 2\,H_2O(l) + 4\,e^-$	0.40	Oxygen + Water

The minimal reduction potential that is required for the water to be oxidized into the products is 1.23 V vs SHE. Due to ohmic losses and sluggish kinetics, the practical potential is typically higher for the reaction to proceed. The anodic reaction thus significantly contributes to the overall cell potential, but is often not studied in papers on CO_2R. For this thesis, the anode was not studied and assumed to be not limiting the rate of the overall redox reaction.

2.1.6. Cathode reactions

The first comprehensive overview of electrochemical CO_2 reduction of various metal surface was published in 1985 by Yoshio Hori et al [24]. The various catalytic metal surfaces were classified into four groups. The first group of metals (Cd, In, Sn, Hg, Tl, Pb, Bi) primarily produced formate ($CHOO^-$). The second group of metals (Zn, Ga, Pd, Ag, Au) mainly catalyzed towards the formation of carbon monoxide (CO). The third group (Ti, Fe, Ni, Pt) primarily produced hydrogen (H_2) and copper (Cu) formed the last group and that uniquely stands out in catalyzing the formation towards aldehydes, alcohols and hydrocarbons. The categorized groups are shown in the periodic table of elements in figure 2.3

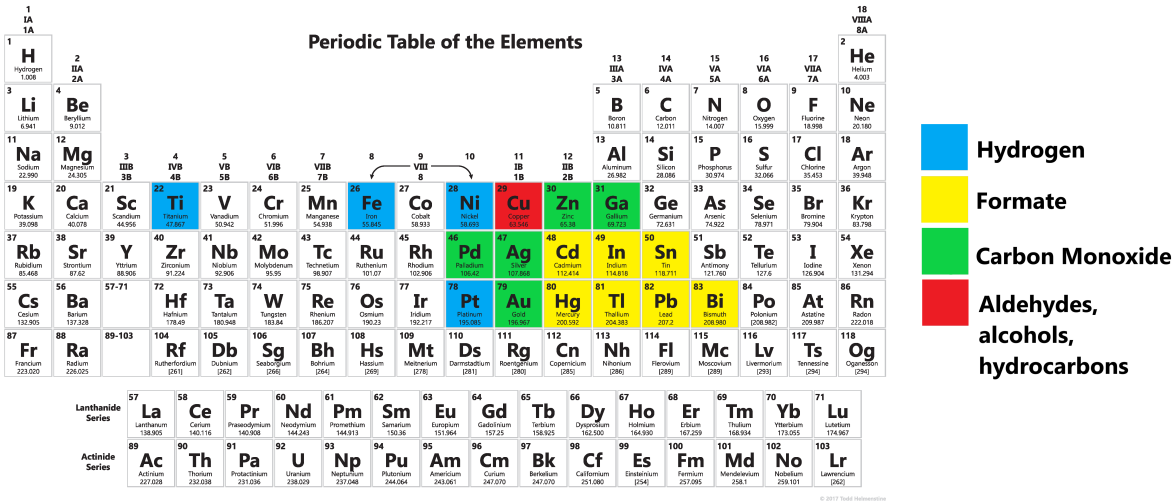

Figure 2.3: Categorized metal groups for CO_2 reduction, where yellow is most selective for formate production, green for carbon monoxide, blue for hydrogen and red for aldehydes, alcohols and hydrocarbons products.

In table 2.2, the reactions towards these products and their thermodynamic potentials are summarized. Here the reactions are ordered starting with the lowest the number of protons and electrons required for the reaction.

Table 2.2: This table shows common C1-C3 CO_2 reduction reactions. The potentials are calculated using the Gibbs free energy, using tabulated data from Engel [20], calculated at pH = 0.

Reaction	E^0 (V vs RHE)	Product
$CO_2(g) + 2H^+ + 2e^- \longrightarrow CO(g) + H_2O(l)$	-0.10	Carbon Monoxide
$CO_2(g) + 2H^+ + 2e^- \longrightarrow HCOOH(aq)$	-0.12	Formic Acid
$CO_2(g) + 6H^+ + 6e^- \longrightarrow CH_3OH(aq) + H_2O(l)$	0.03	Methanol
$CO_2(g) + 8H^+ + 8e^- \longrightarrow CH_4(g) + 2H_2O(l)$	0.17	Methane
$CO_2(g) + 4H^+ + 4e^- \longrightarrow C(s) + 2H_2O(l)$	0.21	Graphite
$2CO_2(g) + 2H^+ + 2e^- \longrightarrow (COOH)_2(s)$	-0.47	Oxalic Acid
$2CO_2(g) + 10H^+ + 10e^- \longrightarrow CH_3COOH(aq) + 3H_2O(l)$	0.11	Acetic Acid
$2CO_2(g) + 10H^+ + 10e^- \longrightarrow CH_3CHO(aq) + 3H_2O(l)$	0.06	Acetaldehyde
$2CO_2(g) + 12H^+ + 12e^- \longrightarrow C_2H_5OH(aq) + 3H_2O(l)$	0.09	Ethanol
$2CO_2(g) + 12H^+ + 12e^- \longrightarrow C_2H_4(g) + 4H_2O(l)$	0.08	Ethylene
$2CO_2(g) + 14H^+ + 14e^- \longrightarrow C_2H_6(g) + 4H_2O(l)$	0.14	Ethane
$3CO_2(g) + 16H^+ + 16e^- \longrightarrow C_2H_5CHO(aq) + 5H_2O(l)$	0.09	Pripionaldehyde
$3CO_2(g) + 18H^+ + 18e^- \longrightarrow C_3H_7OH(aq) + 5H_2O(l)$	0.10	Propanol

While the goal of CO_2R is to convert CO_2 into more reduced species, it is unavoidable that the other reactant, the proton, reacts with another proton in what is known as the hydrogen evolution reaction (HER) (equation 2.7). In alkaline conditions, water can be reduced to hydrogen, with a hydroxide ion as a byproduct (equation 2.8). These reactions are 'parasitic', since they do not contribute to CO_2R and moreover produce hydrogen and hydroxide which respectively increase downstream processing costs and react with CO_2 molecules. A general goal in CO_2R research is to suppress the hydrogen evolution reaction.

$$2H^+ + 2e^- \longrightarrow H_2 \tag{2.7}$$

$$2H_2O + 2e^- \longrightarrow H_2 + 2OH^- \tag{2.8}$$

Besides the kinetics and selectivity issues, physical processes like dissolving the gas into the aqueous phase and subsequent migration to and adsorption of those species at the active sites increases mass transfer resistance. The sum of these losses, combined with the desire to run the reaction at industrially required current densities require the reaction to proceed at higher potential than theoretically should be feasible. The 'extra' potential that is needed is called the overpotential.

In CO_2R research, a focus is on lowering this overpotential and improve product selectivity, which can be achieved in various ways. One of them is to design better catalysts, that improve reaction kinetics and selectivity. Another method is to improve the mass transport of CO_2, which can be the limiting factor of the reaction. The GDE, for example, is an electrode design that improves the availability of CO_2, by decreasing the diffusion length of the CO_2 from the bulk to the active sites. Within the GDE, CO_2 gas first diffuses through the hydrophobic gas diffusion layer and then dissolves in the electrolyte

with a typical diffusion length of 50 nanometer to reach the catalytic site. This is fundamentally different than dissolving the CO_2 in the bulk electrolyte with a H-cell configuration, where the typical diffusion length from the bulk to the active sites is 50 micrometers [17].

2.1.7. CO_2R products

Conversion of CO_2 and H_2O using green electricity provides an sustainable route to producing value-added chemicals and fuels. Typical CO_2R products, like CO, CH_4, C_2H_4 are industrially important precursors to many chemicals in industry. One of the most promising heterogeneous catalysts is copper, that is uniquely capable of producing multi-carbon products (further explained in chapter 2.2.1), like ethylene, ethanol and propanol. Some industrially relevant multi-carbon products are shown in 2.4, where the multi-carbon products are shown in blue, which generally have a higher market price and energy content than single-carbon equivalents. Ethylene serves as an essential building block in the polymer industry for production of food packaging, bottles, bags and other plastic-based goods, antifreeze for airplane engines and wings, PVC pipes, etc. Ethanol is a widely used intermediate and solvent for other chemical processes, and additive for fuels. Propanol is used for fuels/additives, paints and coating additives. Acetic acid is a multicarbon product that is used as a food additive, adhesive and is used for paints.[16]

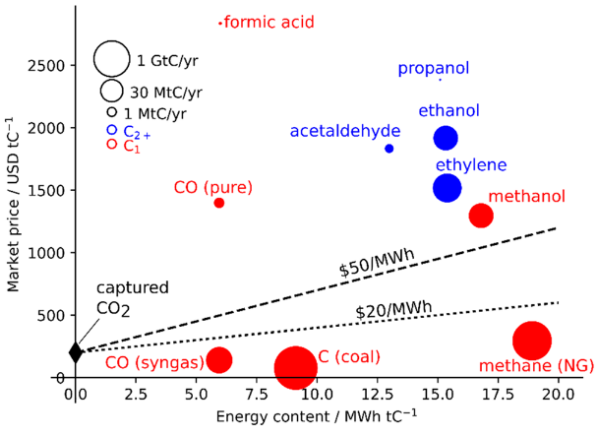

Figure 2.4: Reproduced from Nitopi *et al.* [16].

2.1.8. Membranes for CO_2R

Membranes are used to physically separate the anolyte from the catholyte to avoid mixing, while allowing transfer of certain ions. Furthermore, a membrane is used to avoid dangerous and/or counter-productive mixes of gases like oxygen (formation at the anode) and hydrogen (forms at the cathode). The properties of the membranes contribute to the overall efficiency and durability of the electrolyzer. Certain polymer materials are well known for their water transport and ionic conductivity, and thus suitable for membranes in CO_2R electrolyzers. There are two main types of membranes, i.e. anion- and cation-exchange membranes, where the names reveal their respective ionic selectivity. Anion-

exchange membranes (AEMs) are more commonly used in CO_2R electrolyzers, because they furnish alkaline media [25, 26] as opposed to cation-exchange membrane (CEMs). Electrolyzers where only membranes are present (no electrolytes) and the reactants are vapor-fed, are called membrane electrode assemblies (MEAs). The stacking of these two types of solid electrolytes, and adding catalyst in between, it is called a bipolar membrane. Here water is dissociated at the catalyst into protons and hydroxide, and separated via the CEM and AEM respectively. When the CEM faces the cathode and the AEM faces the anode, the configuration is called reverse bias. Here the BPM dissociates water into protons and hydroxide ions, that migrate to the cathode and anode respectively. When the CEM and AEM are switched, the configuration is called forward bias. Besides ion-exchange membranes there are also porous separators, which rely on separation based on size instead of polarity. [4, 26]

2.1.9. Electrode structures

Conventionally planar electrodes were used for CO_2R. This type of electrode is typically a metal foil or catalyst deposited carbon substrate, which is connected to the external circuit. With planar electrodes, the electrochemical active species diffuse through the electrolyte towards the active electrode surface and get converted into products. A setback of this type of electrode is that the current density is roughly an order of magnitude lower than with GDE. Planar electrodes are nevertheless still used to fundamentally study the CO_2R performance of catalysts, because they bypass complexities such as flooding and salt precipitation, as is the case with GDEs.

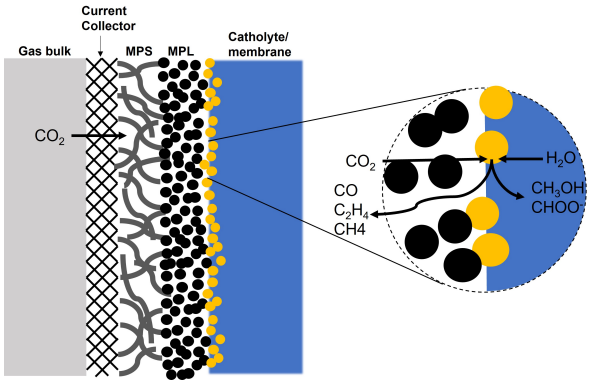

Figure 2.5: Schematic representation of a typical GDE used in CO_2R. The current collector contains flow channels, which are indicated by the white rectangles.

To achieve industrial relevant current densities of >200 mA cm^{-2}, the gas diffusion electrode is paramount for the operation of CO_2R electrolyzers. GDEs are porous, high-surface area materials that are permeable for gasses and impermeable for the electrolyte to prevent flooding, i.e. blocking of the gas-flow channels. It consists of two layers, namely the gas diffusion layer (GDL) and the catalyst layer (CL) (see figure 2.5). The GDL, consisting of a macroporous substrate (MPS) and microporous layer (MPL), allows gaseous reactants, like CO_2, and products to pass and prevent electrolyte from seeping in. The MPS is typically a carbon paper made up of electrically conducting fibres, and the

MPL consists of carbon particles mixed with hydrophobic polytetrafluoroethylene (PTFE). The latter is a polymer that makes the GDL side adjacent to the CL sufficiently hydrophobic, such that aqueous electrolyte is repelled from this layer and thereby allowing the layer to stay permeable for gasses [10, 27]. When electrolyte creeps into the GDL, gas permeation is hindered and the functionality of the GDE is inhibited. This phenomena is called ”flooding” and is one of the major issues relating to GDEs.

Figure 2.6 illustrates the differences in local reaction environment between planar (here interchangeable with H-cell, figure 2.6d,g) and gas diffusion electrodes (figure 2.6e,f,h). In figure 2.6a one can see that protons are quickly depleted as current density increases. Hydronium ions in the electrolyte are the first source for these protons. As hydronium ions quickly deplete, water reduction takes over the role of proton source. The protons react with CO_2 to form relevant products, or they parasitically react with other protons to form hydrogen. The hydroxide ions that are left rapidly increase the pH (figure 2.6c), which favors the formation of C_{2+} products with a copper catalyst [4, 10, 17, 28]. The fundamental difference between the operation with the gas diffusion electrode and planar/porous electrodes is that with a GDE the CO_2 is supplied through the electrode itself and enters the electrolyte close to the active catalytic surface (diffusion length $\approx$ 50 nm), as opposed to planar/porous electrodes where the electrochemically active dissolved CO_2(aq) diffuses from the bulk catholyte with a diffusion length of $\approx$ 50 µm [17] (see figure 2.6g,h). This is a roughly a 3-order of magnitude difference between the diffusion distance to the active catalytic sites. Simply stated, the supply of CO_2 with a GDE is much faster than with planar or porous electrodes and gets less quickly depleted (illustrated in figure 2.6b).

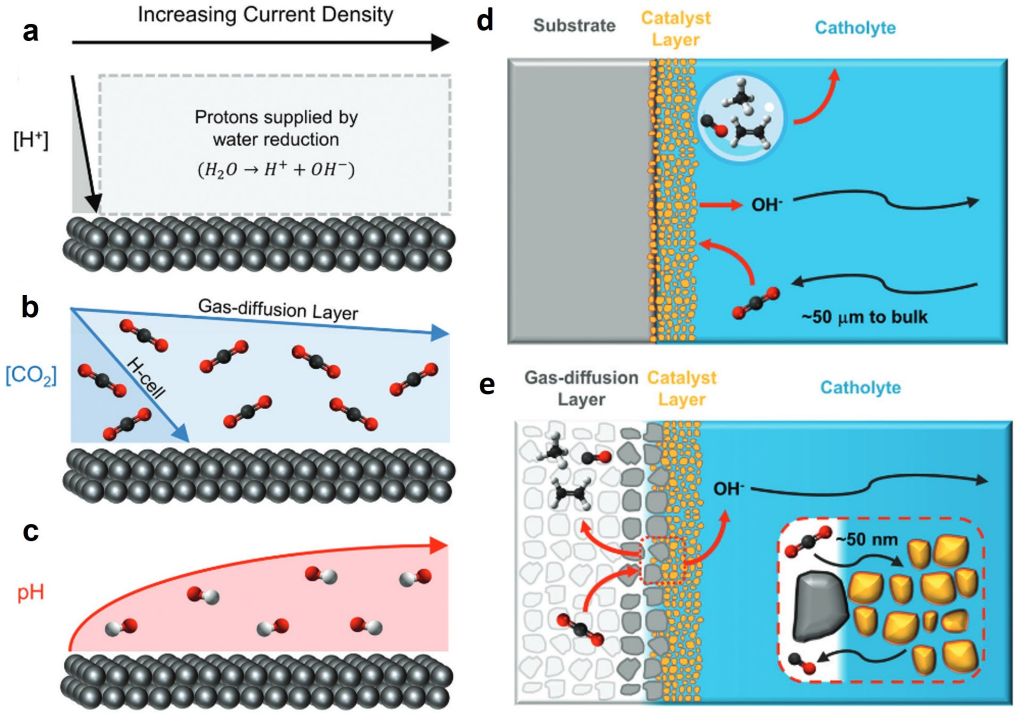

Figure 2.6: This figures illustrates how CO_2R is fundamentally different for planar and GDE electrodes. a) proton concentration as function of current density. b) shows how the concentration of CO_2 depletes faster in a H-cell compared to a GDE. c) shows pH as function of current density. d) H-cell type of CO_2 diffusion mechanism. e) GDE diffusion mechanism of CO_2. Reproduced from Burdyny & Smith [17].

Catalyst layer in GDEs

The catalyst layer consists of a network of catalyst, ionomers and other additives. The active catalyst material is immobilized by ionomers and additives. Ionomers are polymers where the an ionic groups are covalently bonded to the polymer backbone. These ionic groups are neutralized by mobile ions of opposite charge (counter-ions), which gives an ionomer its ion-conductive properties, a critical functionality for transporting ions in solid-electrolyte membranes. A widely used ionomer is Nafion, a certain type of perfluorinated sulfonic acid (PFSA) ionomer with cation-exchange properties. Ionomers serve several identified purposes: i) acts as a 'glue' to immobilize the catalyst and prevent delamination from the GDL (when ionomer and catalyst particles are mixed), ii) provide decoupled pathways for ion and gas transport, iii) play an essential role in altering the electrode performance by influencing local reaction environment such as pH and local concentration of cations. de Arquer *et al.* [8] showed that by spray-casting a Nafion film over the catalyst layer of a GDE, the CO_2 transport at the interface can be increased by a factor of 400 relative to the bulk. This resulted in a significant increase in activity and selectivity to ethylene and carbon monoxide, hence relevant given the aims of this thesis (see introduction 1).

2.2. Copper catalyst

This section of the literature review goes deeper into the catalyst that is used in this thesis: copper. It provides the explanation for the unique electrocatalytic property of copper (chapter 2.2.1), and concludes with the reaction mechanisms (chapter 2.2.2).

2.2.1. Unique electrocatalytic property

Scientists worldwide have been looking for better catalyst materials, that can achieve more selective product formation at lower overpotentials. With the presence of an appropriate catalyst and under an applied potential, CO_2 can be converted at industrially relevant current densities, into high-energy density and value-added multi-carbon products (C_2+) like ethylene (C_2H_4) and ethanol (C_2H_5OH), or into lower order carbon products like carbon monoxide (CO) and formate ($CHOO^-$). These carbon-based products are critical building blocks for the chemical industry. To date, copper is the only heterogeneous metal catalyst that has a propensity to electrocatalytically reduce CO_2 to C_{2+} products via a multi-electron reaction at considerable rates [4, 8, 10, 16, 29–32].

The moderate binding energy of copper for two key intermediate products, is believed to be the reason behind copper's unique catalytic nature. Two critical intermediates are carbon monoxide and protons, that respectively have a slightly negative and almost zero binding energy with copper (see figure 2.7a). Also the morphology of copper centers as well as their sizes and shapes influence the activity and selectivity towards higher order carbon products [33–35]. In figure 2.7b the activity and selectivity of copper as function of potential is shown. While copper is in oxidized form (CuO_x) under atmospheric or aqueous conditions, the copper-oxides are invariably reduced to metallic copper (Cu^0) under reductive conditions [16].

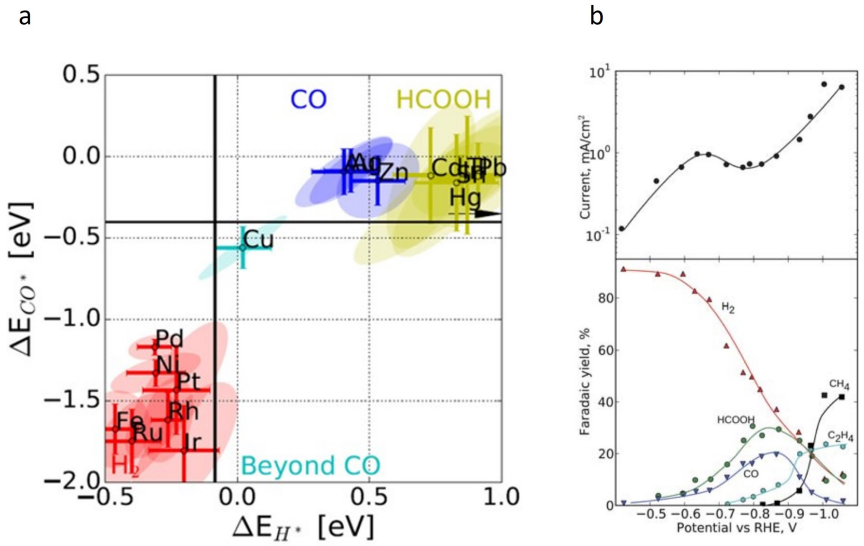

Figure 2.7: a) Binding energy of CO* and H* reaction intermediates with various metals. Reproduced from Bagger et al. [36]. b) Partial current density and faradaic efficiency of copper as a function of the cathodic potential tested in a H-cell. Reproduced from Peterson et al. [37]

2.2.2. CO_2R reaction mechanisms on Cu

Ever since Hori *et al.* [24] made the groundbreaking discovery of copper's unique ability to reduce CO_2 to a variety of (oxygenated) hydrocarbon products, researchers are trying to understand the reaction mechanisms involved [38]. In general, electrochemical reduction of CO_2 starts with the adsorption of CO_2 on the catalytic surface, denoted by $*CO_2$. After adsorption, the $*CO_2$ undergoes multiple proton-electron transfer steps to form intermediates. Intermediate species, a crucial one being *CO, can either be desorped which leads to the end-product, or can undergo additional proton-electron transfer or coupling steps, which leads to other products like CH_4 or C_2H_4. A comprehensive overview of CO_2R reaction pathways to CO, CH_4, CH_3OH, $CHOO^-$, C_2H_4 and C_2H_5OH was made by Kortlever *et al.* [38], see figure 2.8

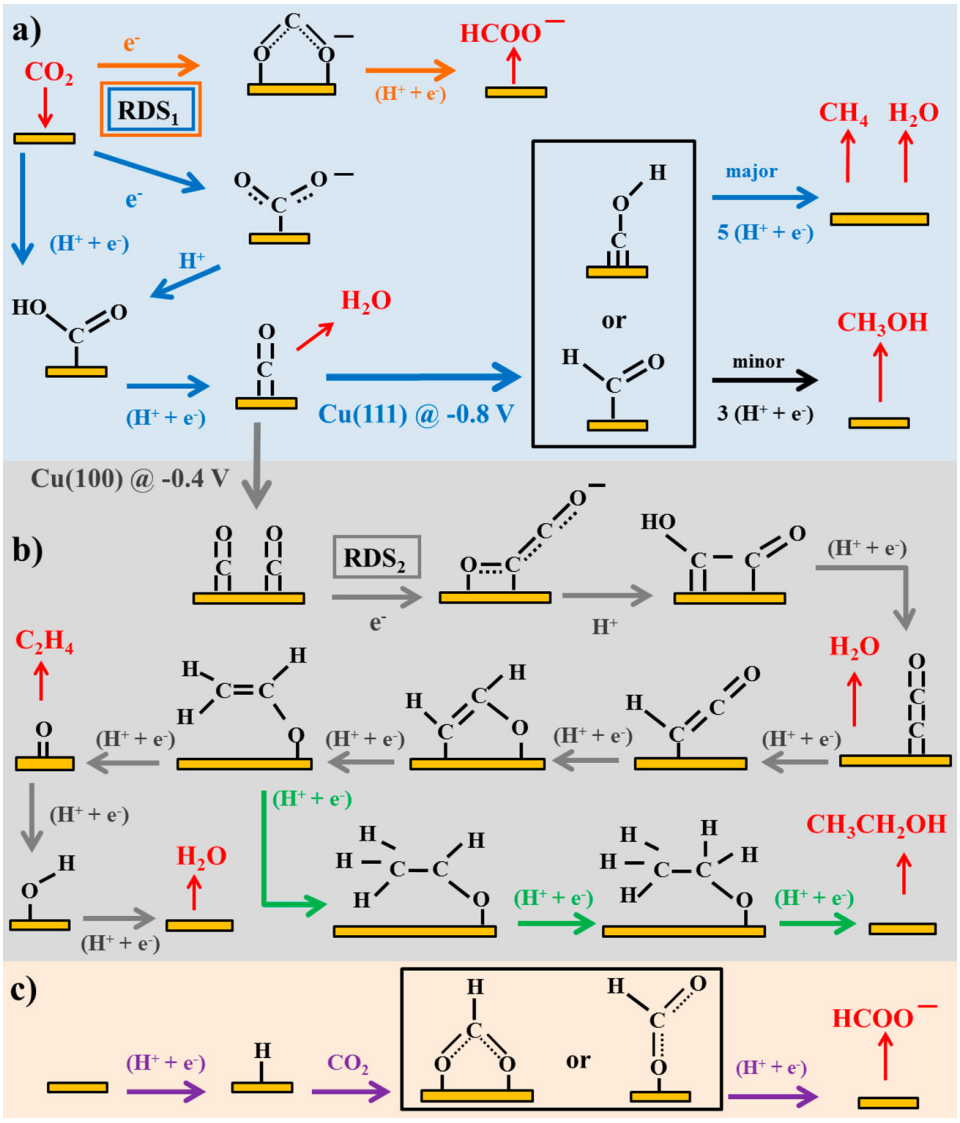

Figure 2.8: Reaction pathways to common products of CO_2R with copper. Blue arrows lead to formation of either CO or CH_4, orange and purple arrows to $CHOO^-$, black arrows to CH_3OH, gray arrows to C_2H_4 and green arrows to C_2H_5OH. Section a) pathways of CO_2 to single-carbon products. b) pathways to multi-carbon products, c) pathway of CO_2 insertion into metal-H bond to formate. Reproduced from [38]

In this comprehensive pathway, it is clear that the *CO intermediate plays an important role. This is supported by experiments of direct reduction of CO (COR), which leads to similar products and yields as CO_2R [16]. CO can be reduced to *CHO or *COH species, which leads to methane. In this step, an early breaking of the second C-O bond is implied, which is thermodynamically unfavorable to late breaking of this bond, according to DFT calculations ([37]). The thermodynamically favored late-breaking of this bond, leads to dimerization of the *CO intermediate yielding ethylene and ethanol after additional proton-electron transfers. Another interesting observation is that while the *CO intermediate can either be desorbed to yield carbon monoxide, or be dimerized to yield C_{2+} products, the path towards formate leads to a dead end.

2.3. Ionomers in CO_2R

In this section of the literature review, a closer look is taken into the application of ionomers in CO_2R. Firstly, an overview of ionomers used in CO_2R is provided. Next, a widely used class of ionomers, so called perfluorinated sulfonic acid ionomers, is explained in detail in chapters 2.3.3 to 2.3.8. Finally, two influential references about the application and effects of Nafion, the ionomer used for the experimental part of this thesis, are explained in chapter 2.3.9.

2.3.1. Application of ionomers in CO_2R

Ionomers are ion-conducting polymers with functional groups that facilitate ion transport, either anions or cations. The functional groups are oppositely charged with respect to the exchanged ions. Ionomers can be used as an additive in/on the catalyst layer, to immobilize the catalyst and tailor the micro-environment. When these ionomers are confined to nanometer-scale thin-films, interesting agglomeration and interfacial interactions can be expected. The chemical makeup and architecture of the ionomer determines the various interactions with the catalyst, solvent, dissolved species, gases and with other ionomers in the bulk. The ionomer layer undoubtedly influences the micro-environment like the concentration and presence of species, which inevitably influences the CO_2R performance. While there is a rising number of publications about the CO_2R promoting effects of ionomers (see table 2.3), the interfacial interactions between the catalyst and the ionomer are not yet understood.

Table 2.3: List of references where the effect of the ionomer was investigated. The description of the catalyst indicates if it is an ionomer film (planar) or catalyst ink (GDE). Noticeably, Nafion is the most common entry.

Ionomer(s)	Description of Catalyst	Effect of Ionomer	Reference
Nafion and Sustainion	Cu on PTFE (planar)	Increased FE to C_{2+}	Kim *et al.* [6]
Nafion	Cu Planar	88% FE_{CH4}	Pan & Barile [7]
Nafion	Cu and Ag based GDEs	Increased FE and CD to C_{2+}	de Arquer *et al.* [8]
Nafion	CoPc-based GDEs	FE_{CO} > 99%	Wan *et al.* [39]
Nafion	ZnO Planar	Increased FE_{CO}	Zeng *et al.* [40]
Nafion and PFAEM	Ag- and SnO_2- based GDEs	Increased FE_{CO}	Chen *et al.* [41]
Imidazolium ionomer	Ag Planar	Promoted HER	Koshy *et al.* [42]
Nafion	Cu-based porous and GDE	Increased FE_{CO}	Guzmán *et al.* [43]
FAA-3 and Sustainion	Cu-based GDE	Increased C_{2+}	Puring *et al.* [44]
Imidazolium	Sn-based GDE	Increased FE_{CHOOH}	Yang *et al.* [45]

2.3.2. Anion Exchange ionomers incorporated into catalyst layer

Anion exchange ionomers are highly conductive for OH^- and other anions. Hydroxide ions at the cathode can react with CO_2 towards undesired (bi)carbonates, but simultaneously impede proton reduction by increasing the local pH which is beneficial for CO_2R reactions. This ambiguous function could possibly be exploited in the catalyst layer of the cathode, either alone or in combination with CEM, to engineer an optimal local reaction environment. Examples of AEM are Sustainion and QAPPT (see figure 2.9). QAPPT is the abbreviation for quaternary ammonium poly(N-methyl-piperidine-co-p-terphenyl). Sustainion is a N-methylimidazolium-functionalized styrene polymer. AEMs are used in both zero-gap

electrolyzers [26] and flow-through electrochemical cells [6]. Kutz *et al.* [46] showed that by incorporating Sustainion into the catalyst layer of an Ag GDE, they could increase CO selectivity from 25% to 95%. The anion-conducting Sustainion repels protons, which results in this high CO yield.

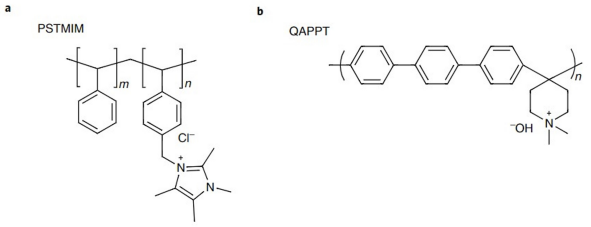

Figure 2.9: a) Sustainion, b) QAPPT. Reproduced from Salvatore *et al.* [26].

2.3.3. Perfluorinated sulfonic-acid ionomers

Perfluorinated sulfonic-acid (PFSA) ionomers are frequently a critical constituent of electrochemical energy conversion devices, for example as membrane and/or as catalyst layer additive in CO_2 electrolyzers. PFSA ionomers are well-known for their excellent proton-conductivity and chemical-mechanical stability. The name of perfluorinated sulfonic-acid (PFSA) ionomers can be derived from the observation that all hydrogen atoms on the carbon atoms have been replaced by a fluorine atom, hence perfluorinated, with an ether side chain terminated by a sulfonic acid group. The hydrophilic sulfonic acid group makes PFSA ionomers cation exchangeable. The most famous PFSA ionomer is Nafion (see figure 2.11), which was originally developed by DuPont Company back in the 1970s. It was discovered during research into sodium-ion conductors in the chlor-alkali industry. Since then, it has found other major applications in electrochemical energy conversion technology. Nafion is well known for its excellent proton-conductivity and chemical-mechanical stability which is why it is still, despite its age, extensively used as solid-electrolyte for energy storage and conversion devices.

Besides Nafion there are other PFSA ionomers, for example those by 3M, Solvay Speciality Polymers (Aquivion) and Asahi Glass (Flemion). PFSA ionomer structure is characterized by i) equivalent weight (EW), i.e. grams of drypolymer per mol ionic group, ii) side chain chemistry and length [47]. These two properties determine the physicochemical nature of the ionomer. Nafion has a fairly long side chain and high EW compared to other PFSA ionomers. The last major review on PFSA ionomers was done is 2017 by Kusoglu & Weber [47].

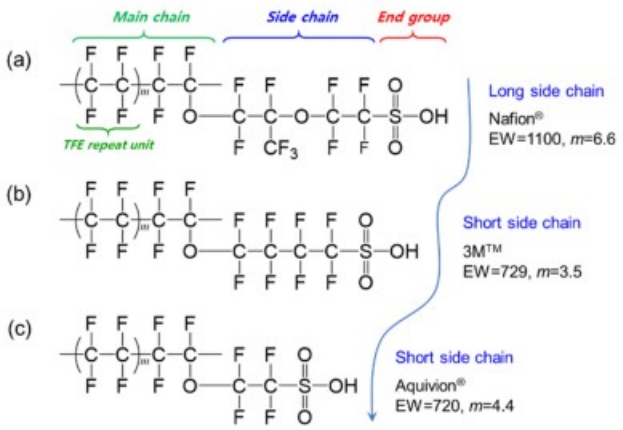

Figure 2.10: Three common PFSA ionomers. Reproduced from Shin *et al.* [48]

2.3.4. Phase-Separated Morphology of PFSA ionomers

PFSA ionomers consist of a hydrophobic polymerized tetrafluoroethylene (PTFE) backbone and tethered perfluorovinyl ether groups terminated with a sulfonic acid group (which makes it locally hydrophilic). The hydrophobicity of the backbone can be ascribed to fluorine's low polarizability and weak London dispersion forces. The chemical stability is due to fluorine's high electro-negativity which makes the C-F bonds very strong. The contrast in polarity between hydrophobic and hydrophilic domains is called the phase-separated morphology. This phase-separated morphology of PFSAs (see figure 2.11) is suspected to enable decoupled diffusion of CO_2 and water through the hydrophobic and hydrophilic domains, respectively. A high proton conductivity is observed when the ionomer is sufficiently hydrated , while the gas transport mechanism is more complex [47, 49]. The decoupled transport mechanisms could improve mass-transfer capabilities in the catalyst layer to promote CO_2R [4, 8, 50–53].

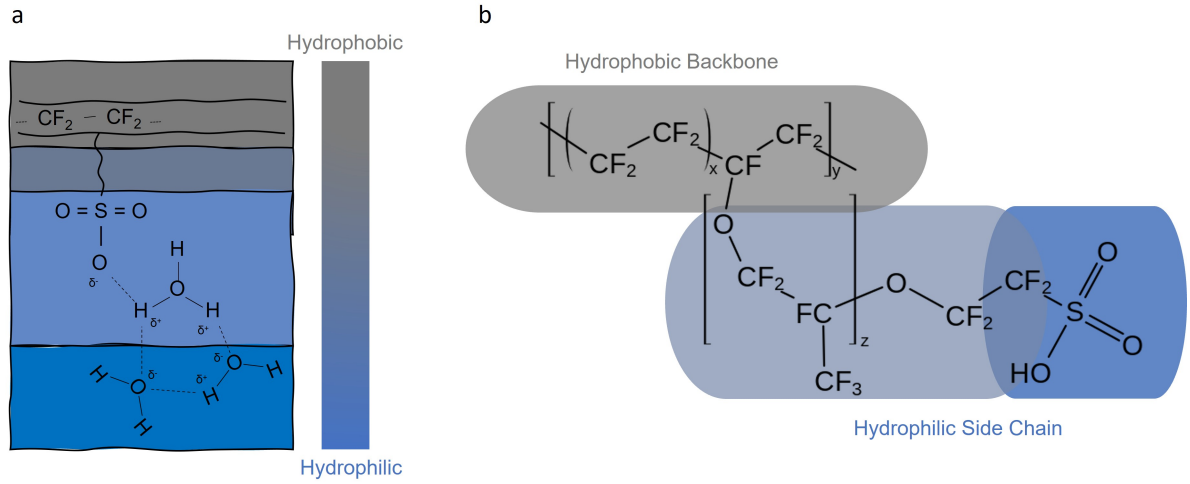

Figure 2.11: a) This figure illustrates how the phase-separated morphology segregates the hydrophilic and hydrophobic regions. The hydrophilic region is made up of a network of hydrogen bonded molecules. The negative charge on the sulfonate side group enables cation-exchange through this region. b) PFSA ionomer phase-separated morphology with a hydrophobic backbone and hydrophilic side chain.

Allen *et al.* [54] conducted a nanoscale study on the morphology of Nafion in dry and hydrated state, using analytical transmission electron microscopy (TEM) and cryogenic TEM tomography, respectively. For the dry-state, they revealed $\approx$ 3.5 nm in diameter spherical clusters for the hydrophilic sulfonic-acid containing phase. In contrast, the hydrated Nafion membrane consisted of an interconnected channel-type network, with a domain spacing of $\approx$ 5 nm, as revealed by cryogenic TEM. Nafion is able to swell up by approximately half its volume, by absorption of more than 20 water molecules per sulfonic-acid group, without losing structural stability [54].

2.3.5. Chemical-mechanical energy balance of PFSA ionomers

Sorption behavior of PFSA is the most important phenomenon affecting the transport and structural properties of [47]. Generally the higher the water content, the higher the ionic conductivity. The sorption capacity is quantified by the water content λ (see equation 2.9), defined as the number of moles of water per mole of sulfonic acid groups (mol H_2O / mol SO_3^-).

$$\lambda \equiv \frac{n(H_2O)}{n(SO_3)} = (\frac{\Delta M_{H_2O}}{M_p})\frac{EW}{\bar{M}_{H_2O}} \tag{2.9}$$

Here ΔM_{H_2O} is the difference in water mass between the initial and final measurement, M_p is the mass of the polymer, equivalent weight (EW) which is defined as the grams of dry polymer per ionic group (i.e. $g_{polymer}/mol_{ionic\text{-}group}$), and $\bar{M}_{H_2O}$ is the molar mass of water. The EW of Nafion is 1100, which means it has a fairly long side chain as compared to other PFSA ionomers. The water uptake capability decreases with an increasing EW [47], decreasing solvent polarity [55], contamination and aging [56], and mechanical compression [57]. The above effects can be considered to either increase propensity for dissolution or increase the backbone's resistance to deformation. The effects combined are the so called chemical-mechanical energy balance of the PFSA ionomer: "The water-uptake process is governed by the solvation energy of the ionic groups and chemical potential driving the external water molecules to attach to the hydrophilic ionic moieties of the membrane, which are counterbalanced by the deformation of the ionomer's hydrophobic matrix (i.e., the chemical-mechanical energy balance)" [47]. Deformation of the ionomer by the water-uptake process can be observed by atomic force microscopy, and is one of the primary aims of this thesis (see chapter 1).

The swelling and sorption process of a PFSA ionomer consists of complex interactions and results in a non-linear water uptake, which is nicely summarized in a review paper by Kusoglu & Weber [47]. Figure 2.12a shows the sorption isotherm where bound water has an activity of $\approx$ 0, and bulk-like domains with free water have an water activity of 1. The first stage is the adsorption of the counter-ion (H^+) and water on the fixed anionic site (SO_3^-). Since PFSA has a strong acid moiety, the proton gets donated to a water molecule and forms and hydronium ion (H_3O^+) [47]. After the formation of the primary hydration shell, the next phase is the clustering of more of these electrostatic interactions, which still have a restricted mobility. The addition of more water molecules ($\lambda \approx$ 2-3), increases water

mobility and eventually results in percolation, i.e. the interconnection of aqueous clusters. From this stage on, the ionomer exhibits better ion- and water-transport properties. Further swelling results in hydro-channels with bulk-like water behavior, which is called free-water swelling.

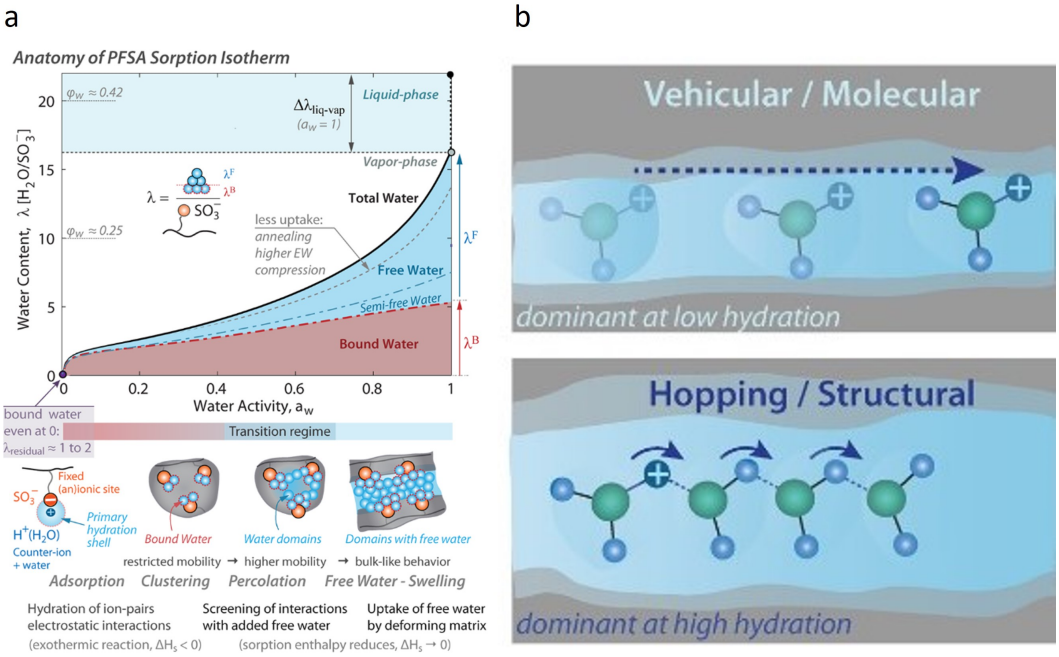

Figure 2.12: a) This figure shows how the water content depends on the water activity. The water activity is defined as 0 when there is no water present, while a water activity of 1 defines a maximum absorption of water. As swelling increases, a fraction of water is so-called bound water and not mobile, while another fraction is free water and able to dynamically move. The swelling is associated with an deformation of the ionomer matrix. b) This figure shows two transfer mechanisms, the first being vehicular motion of molecules at dominant at low hydration. The other transport mechanism is structurally based, sometimes referred to as Grotthuss hopping and dominant at high hydration. Reproduced from Kusoglu & Weber [47].

2.3.6. Proton Transfer Mechanism in PFSA Ionomers

As water content λ increases, proton conductivity increases [47]. The key in proton conduction in PFSA ionomers, is the formation of a hydrogen bonded network of water molecules that display amphotericity (i.e. it acts both as a proton donor (H_3O^+) and proton acceptor (H_2O)). The nature of proton conduction is possible due to either Grotthuss hopping (structural diffusion) or vehicular (molecular diffusion) (see figure 2.12b). Grotthuss hopping, also known as proton jumping, is where the proton diffuses through the hydrogen bonded network. Vehicular/molecular diffusion is the diffusion of hydronium ions through the water channels.

The proton transfer mechanism starts with the dissociation of the proton from the sulfonic acid group ($SO_3H \rightarrow SO_3^- + H^+$). Upon separation, subsequent solvation of this proton with water molecules results in a hydronium ion (H_3O^+). Additional water molecules create a larger hydration shell and ultimately allows for larger protonic species such as the Eigen- and Zundel-ion, $H_9O_4^+$ and $H_5O_2^+$, respectively to exist. With increasing water content λ, the hydrophilic water domains grow and eventually become interconnected, which is called percolation (see figure 2.12a). Increasing hydration extends the three-

dimensional hydrogen bonded network and increases proton mobility in the hydrophilic domains of the ionomer [47].

2.3.7. PFSA thin films

The aggregation states and physical properties of PFSA ionomer thin films are dependent on the thickness and interfacial effects with the substrate [47, 58]. Thin films are produced by various methods like spin-coating, self-assembly and drop-casting. Concentration, solvent, drying conditions, are some parameters known to be influencing the structure and subsequently the properties of PFSA thin films. As PFSA films decrease in thickness, initial bulk properties change due to effects like confinement resulting in stronger substrate-ionomer interactions [59]. A study by Kusoglu *et al.* [60] have demonstrated that due to confinement effects and wetting interactions, PFSA thin films (thicknesses ranging from 4 to 300 nm) exhibit a different morphology compared to the bulk PFSAs. Independent of the substrate, as the films' thickness decreased, initially there was a decrease in swelling followed by an increase for film thicknesses below ≈20 nm due to a disordering of the film hydrophilic/hydrophobic phase-separated structure (see bottom part of figure 2.13a).

Kushner *et al.* [61] found that the molecular orientation of PFSA ionomers in thin films is dependent on the substrate onto which it is casted. They found that on SiO_2 substrates, PFSA ionomers exhibit a nearly isotropic molecular and nanostructural orientation (see figure 2.13b). In constrast, thin films on gold and platinum display more parallel backbone orientations, relative to the substrate, with decreasing film thickness. $\langle S \rangle$ is the order parameter of the molecular structure, also referred to as Hermans order parameter in the X-ray scattering field, which is −0.5 if the molecule is parallel to the substrate 0 if isotropic, and 1 if perpendicular to the substrate. From their results it is clear there is difference in orientation between the backbone and side chain under confinement.

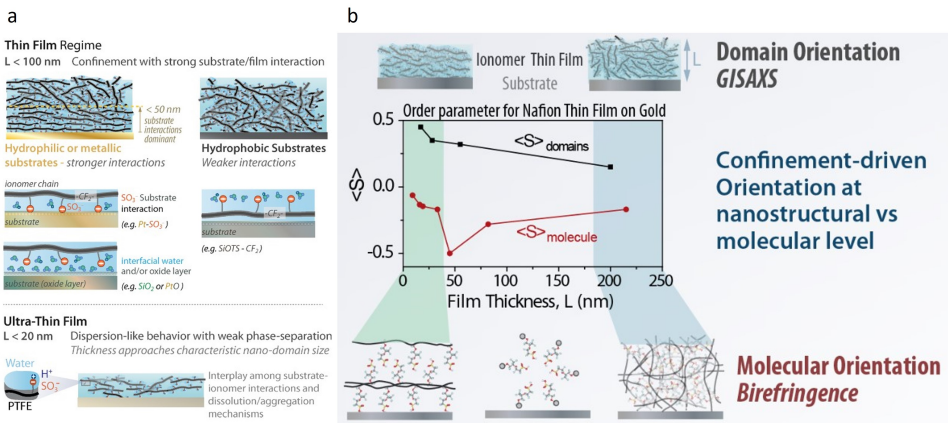

Figure 2.13: a) Orientation of Nafion thin and ultra thin films on hydrophilic or metallic substrates [47]. b) Nano-domain and molecular orientation driven by confinement [61].

2.3.8. Dispersion and adsorption characteristics of PFSA ionomers

While PFSA ionomers exhibit their functionality in solid form, they are produced by solution processing techniques. Dispersion media and processing conditions are thus important to consider. Paul [62] showed that the type of dispersion media influences agglomeration significantly for self-assembled Nafion thin films. In this study, SiO_2 substrates were exposed for 12 hours to a dilute concentration of 0.1wt% ionomer, with varying water to isopropyl alcohol contents. From their results (see figure 2.14) it is clear that the dispersion media influences the agglomeration and adsorption process during self-assembly casting method.

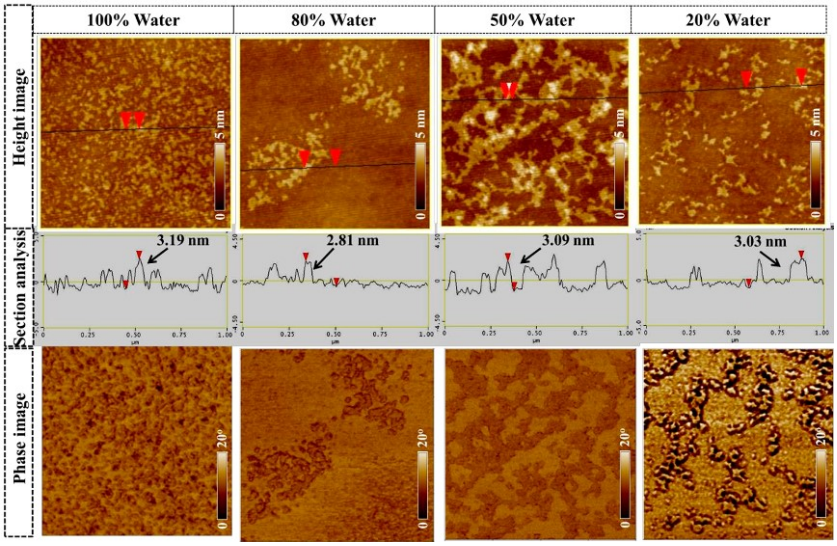

Figure 2.14: This figure shows the surface morphology of Nafion thin films on SiO_2 substrates, produced by self-assembly. Nafion was dispersed in a combination of water and iso-propanol. Reproduced from [62].

The colloidal structure of PFSA ionomers in dispersion depends on the solvent that is used. In polar solvents like water, methanol, ethanol and isopropanol (decreasing polarity), PFSA ionomers form colloids where the hydrophobic backbones interact with one another to minimze contact area with the solvent and the hydrophilic sulfonate groups ($-SO_3^-$) are likely exposed to the polar solvent. Berlinger *et al.* [63] found that ionomer adsorption depends on the solvent-driven interactions, rather than ionomer/surface interactions. In this study they found that increasing the water content in the solvent, promotes ionomer adsorption, which is likely a result of entropic hydrophobic interactions where ionomer contact area with water is inclined to minimize. Increasing polarity of the solvent induces increased ionomer aggregation and causes the ionomer to be less well-solubilized, driving adsorption on the substrate surface.

2.3.9. Application of Nafion in CO_2R Electrolyzers

In CO_2R conditions, the ionomer is in contact with an aqueous electrolyte and catalysts. Due to swelling, the ionic heads are increasingly surrounded by electrolyte, which enables ion- and water transport. In this hydrophilic environment, it can be expected that the hydrophobic backbones aggregate, in order to

minimize contact area with water. During CO_2R, the ionomer aggregation and catalyst particle interaction could dynamically change with local reaction conditions, due to the change of electrolyte properties (e.g. pH) and electrode wettability. As the catalyst surface becomes more negatively charged, anionic heads (sulfonate groups on PFSA) are expected to be repelled and thus affect the ionomer morphology. While the physical interactions are not well understood, the effects of ionomers on CO_2R performance are widely reported.

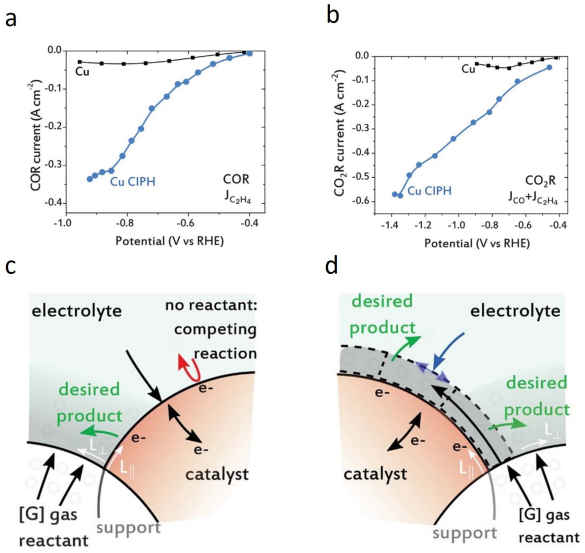

Figure 2.15: This figures illustrates the enhancing effect of COR and CO_2R of a ionomer thin film on Cu (CIPH, catalyst:ionomer planar heterojunction), applied in a GDE. a) shows the increased partial current density of Cu COR towards ethylene. b) shows the increased summed partial current density towards carbon monoxide and ethylene on Cu catalyst. c) without CIPH, d) with CIPH. Reproduced from de Arquer *et al.* [8].

The addition of ionomers to the catalyst layer can increase current densities of electrochemical CO_2RR towards multi-carbon product formation [4, 8, 44]. de Arquer *et al.* [8] found that by spray-casting ionomer solution on a copper GDE catalyst, the faradaic efficiency towards CO and ethylene increased significantly (see figure 2.15a and 2.15b) relative to a bare copper catalyst, while the HER was similar between both cases. Cu samples with ionomer yielded partial current densities towards ethylene and CO of 510 mA cm^{-2}, whereas bare Cu catalyst yielded only 50 mA cm^{-2}. Figure 2.15c shows a plausible explanation for the increased current density effect of the ionomer towards CO and ethylene. Reactants combine at 'reactive' three-phase boundaries (TPB) to form products. These reactive areas can be limited by mass transport of reactants like CO_2 and protons from the liquid bulk, but also by sluggish removal of products. The addition of the ionomer can effectively extend the reactive area, and change CO_2/H_2O ratio in favor of the CO_2RR. The authors claimed that the observed enhancement in current density towards CO_2R could be explained by a 400x increased CO_2 diffusion relative to the bulk electrolyte. Furthermore, they found that in a H-cell configuration, the addition of the ionomer yielded a slight improvement in reaction kinetics, as indicated by a higher current density at low overpotential. However, they also observed similar limiting current densities, implying that the ionomer layer does not improve diffusion limitations. This seems plausible, because with an H-cell the

dissolved CO_2 should still diffuse through the hydro-channels formed by the ionomer and is in essence identical to the case without ionomer.

Besides creating favorable conditions for CO_2R related reactions, the ionomer should ideally suppress competing reactions, like the hydrogen evolution reaction (HER). The reactant for the HER is water (or hydronium ions in acidic conditions), which is likewise a critical reactant for CO_2R reactions. Ionomers decrease water concentration relative to the bulk electrolyte (see figure 2.16e, 2.16), and typically have a higher CO_2 solubility than the aqueous electrolyte. The ratio CO_2/H_2O thus increases with a thin film ionomer layer compared to bare copper. This favors CO_2R over HER, which is evident from the results found by Kim *et al.* [6].

They showed that a Nafion film can increase CO_2R and suppress HER in a 0.1 M cation-HCO_3 electrolyte (figures 2.16a, c), with respect to bare copper (figures 2.16b,d). They demonstrated an increasing partial current corresponding to the formation of C_2H_4, C_2H_5OH and $HCOO^-$ with respect to an increase in atomic radius of the cation: $Li^+ < Na^+ < K^+ < Rb^+ < Cs^+$. They attributed this effect to the increases electrostatic field in the double layer, which increases with the a decreasing radius of the hydrated cation in the outer Helmholtz plane. This increase in electrostatic field stabilizes the adsorption intermediates with strong dipoles. Furthermore Kim *et al.* [6] showed by using pulsed electrolysis and bilayer cation- and anion-conducting ionomer coatings on a copper catalyst, the selectivity and activity towards C_{2+}-products could be increased. Their claim about the ionomer layer is that it modulates the micro-environment (CO_2/H_2O-ratio and pH) near the copper catalyst. The stacking of ionomer layers with different properties could optimize the micro-environment required for CO_2R (figure 2.16g). A visual explanation is shown in figure 2.16.

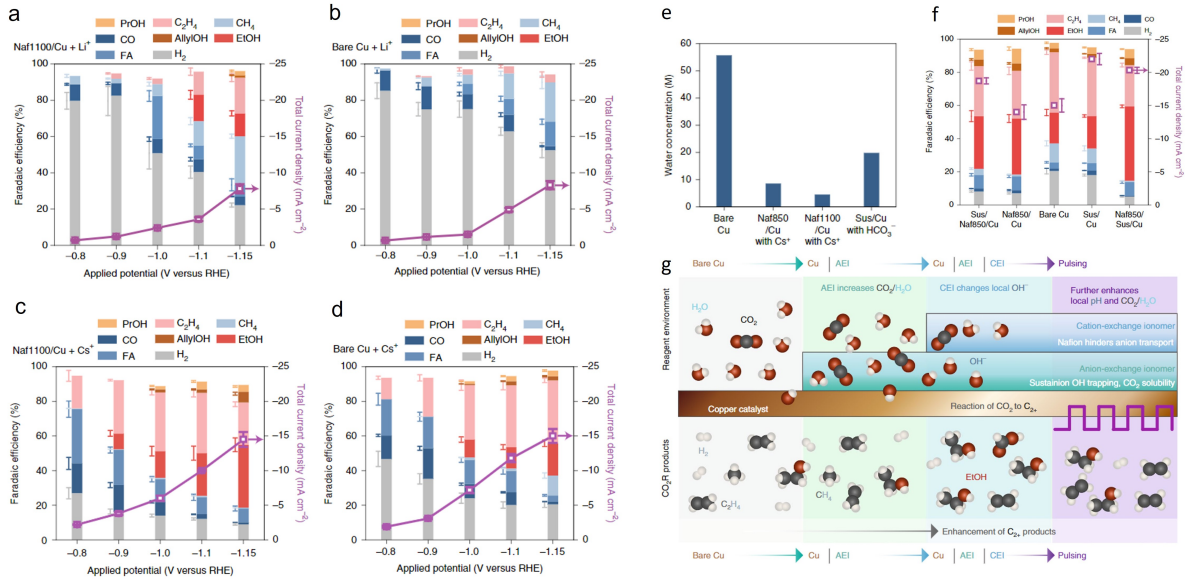

Figure 2.16: This figure shows the effect of cations and Nafion thin films on CO_2R. a) FE and CD of Naf1100/Cu + Cs+, b) FE and CD of bare Cu + Li+, c) FE and CD of Naf1100/Cu + Cs+, d) FE and CD of bare Cu + Cs+. e) Comparison of water concentrations of bare and ionomer coated catalysts, f) comparison of CO_2R performance of Nafion coated samples. g) Summary of the effects of thin films and pulsed electrolysis. Reproduced from Kim *et al.* [6].

While there are plenty of resources available on the positive effects of ionomers on CO_2R, there are also indications that ionomers do not promote CO_2R. Koshy *et al.* [42] found that the imidazolium-based ionomers did not impact CO_2R activity on a silver catalyst. Moreover the ionomer promoted the competing hydrogen evolution reaction, as opposed to bare Ag catalyst. This study indicates that the interaction between ionomer and catalyst provides an avenue to steer both the selectivity and activity.

3

Materials and Methods

3.1. Electrochemical CO_2R experiment

In this thesis, electrochemical CO_2R experiments were performed to get insights into the effect of the ionomer on product formation. Electrochemical experiments were conducted at ambient temperature with a flow cell (figure 3.2). Nickel-mesh was used as the anode, to which a copper foil was attached. The external voltage is provided by a potentiostat, a device that enables us to measure the voltage, current and other electrical metrics of their electrochemical experiment. The potentiostat controls the potential between the reference and the working electrode (cathode for CO_2R), and measures its resulting current. With a feedback mechanism, the voltage of the counter-electrode is adjusted so that the potential between the reference and working electrode is maintained. For the cathode a sputtered copper layer with a thickness of 150 nm on a copper plate was used as the cathode, and was stored under Argon gas before testing. A Nafion-115 (thickness: 127 µm) cation-exchange membrane was selected to separate the anolyte and catholyte. The anolyte was a 1 M KOH solution and for the catholyte a 0.1 M KHCO3 was chosen, both circulating at 20 mL min^{-1} through the flow cell. The 0.1 M $KHCO_3$ solution was first saturated (pH shifts from 8.3 to 6.8 due to bicarbonate equilibrium reactions) by continuously bubbling CO_2 for 30 minutes through the solution at 50 sccm. After saturating the solution with CO_2(aq), the gas flow rate was decreased to 10 sccm which was kept constant during the experiments. A small amount of chelating agent EDTA (2 mg / 100 mL) was added to the catholyte to scavenge and neutralize metals and other impurities in solution.

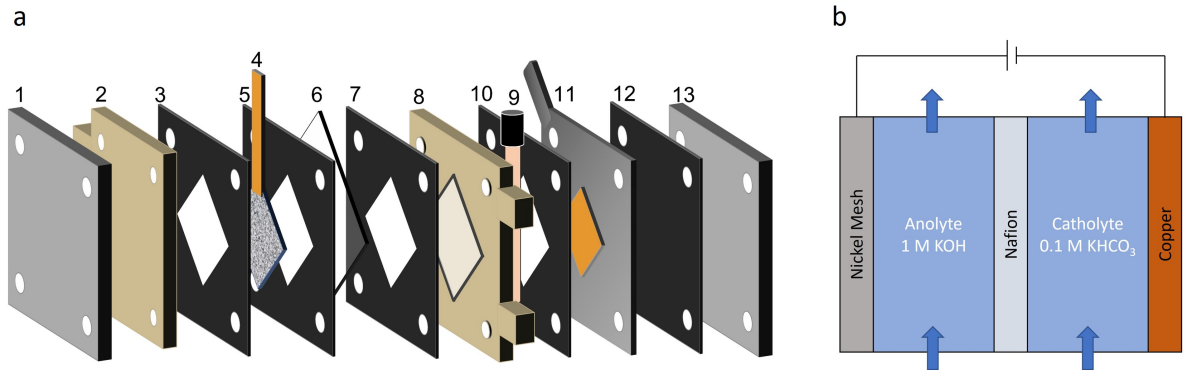

Figure 3.1: a) Exploded-view drawing of the CO_2R flow cell. 1, 13: stainless steel endplates. 2,8: PTFE flow chambers. 3,5,7,10,12: gaskets. 4: nickel-mesh anode. 6: nafion-115 membrane. 9: Ag/AgCl reference electrode. 11: copper cathode + stainless steel current collector. b) This schematic illustrates the flow cell configuration.

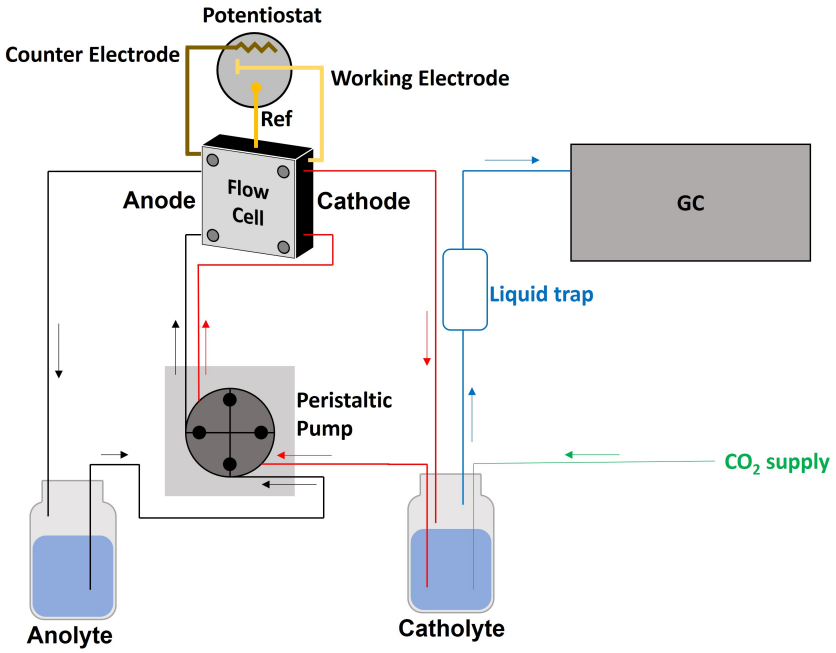

Figure 3.2: Experimental setup used for flow cell CO_2R experiments. This aqueous-based system pumped the electrolyte at a 20 mL/min rate, and continuously bubbled 10 sccm CO_2 into the catholyte. The gas-tight catholyte was connected to a liquid-trap, which was connected to a GC.

3.1.1. Electrochemical impedance spectroscopy

Electrochemical impedance spectroscopy (EIS) measurements were performed to determine the uncompensated resistance (R_u) between the reference (leakless Ag/AgCl, 3.4 M KCl) and working electrode. The real and imaginary part of impedance can be graphed in so-called Nyquist plots (see appendix figure 6.4), where the x-axis is the real part and the y-axis is the imaginary part of impedance. When doing EIS at high frequencies, the intersection of the measured impedance data is the uncompensated resistance between the reference and working electrode. The uncompensated resistance was measured using potentiostatic EIS, with a start frequency of 10^5 Hz, end frequency of 1 Hz, and the amplitude was 10% of the set potential of the corresponding experiment.

3.1.2. Chronoamperometry

Constant potential was applied during the experiments, hence the current (ampero) was measured (metry) in time (chrono). The flow-cell was connected via tubes to a gas chromatogram (GC) to measure the concentration of gaseous species. The system needed some time to reach steady state in the gas phase, because of the low volume flow from the pump. Typically after 4-6 gas injections of 5 min, the volume above the catholyte (head-space) was homogenized. After the gas injections, the experiment was stopped to obtain liquid samples in 1.5 mL Eppendorf tubes.

3.1.3. Capacitance measurements

The capacitance was measured before and after chronoamperometry. This was done by performing cyclic voltammetry at different scan rates, with vertex potentials in the non-faradaic region. It is important to ensure that there is no redox reaction taking place, because that enables to merely determine the surface charge at the double layer. At each of the 8 scan rates 5 cycles were made, and the scan rate was decreased from 500 mV s^{-1}, to 20 mV s^{-1}. The capacitance C was determined by calculating the slope of the fitted line through the data points:

$$C = \frac{Q}{E} = \frac{I}{\dot{E}} \tag{3.1}$$

where Q is the charge [C], E is the potential [V], I is the current [C s^{-1} = A], $\dot{E}$ is the scan rate [V s^{-1}].

3.2. Gaseous products analysis

Gaseous products were analysed with a GC, which measures the concentration of each component in a gas stream. Combining the data from the mass flow meter with the GC, the faradaic efficiencies (FEs) of the gas products could be calculated, using equation 3.2

$$FE(\%) = \frac{c \cdot z \cdot 10^{-6} \cdot \dot{V} \cdot 10^{-6} \cdot \frac{P}{RT} \cdot F}{I \cdot t} \cdot 100\% \tag{3.2}$$

where c is the concentration of gas [ppm], z is the number of electrons involved in the reduction reaction, $\dot{V}$ is the volumetric flowrate [mL·min], P is the pressure [Pa], R is the gas constant [m^3·Pa· mol^{-1}·K^{-1}], T is the temperature [K], F is Faraday's constant [C·mol^{-1}]. The first 10^{-6} constant is to convert ppm to a fraction, the second 10^{-6} constant is to convert mL to m^3.

3.3. Liquid products analysis

Analysis of liquid mixtures of different components, can be performed with high performance liquid chromatography (HPLC). The basic principle of HPLC is a difference in interaction of liquid components with a solid adsorbent material. The nature of these interaction are typically a combination of

hydrophobic, dipole-dipole and ionic. HPLC systems are equipped with a long column filled with this solid adsorbent, through which the liquid analyte and a mobile phase is pumped under high pressure (50-350 bar). This mobile phase is typically a mixture of solvents. Due to the difference in adsorption of components in the sample, there is separation between them. At the end of the column, a detector generates a signal proportional to the amount of separated products emerging from the column, and thus allows for quantitative analysis.

Liquid products' concentration were quantitatively analysed with high performance liquid chromatography (HPLC). Nuclear magnetic resonance (NMR) was also employed to confirm the findings from HPLC. The 1260 Infinity II LC system from Agilent Technologies was used, equiped with a variable wavelength detector (VWD, dual wavelength: 210 nm, 280 nm) and a refractive index detector (RID). HPLC analysis was done for formic acid, acetic acid, acetaldehyde, ethanol and propanol. The signal from HPLC analysis in ppm was converted into FE (%) with the formula below:

$$FE = \frac{c \cdot 10^{-3} \cdot V \cdot F \cdot z}{M_w \cdot C} \cdot 100\% \tag{3.3}$$

where c is the concentration from HPLC, 10^{-3} is the conversion factor [g L^{-1}], V is the volume [L], F is Faraday's constant [C mol^{-1} e^-], z is the number of electrons involved in the reaction [mol e^-], M_w is the molecular weight of the product [g mol^{-1}], C is the consumed charge [Coulombs].

3.4. Catalyst preparation

The copper catalyst was prepared using magnetron sputtering (AJA international ATC 2400 Sputtering System). Copper foils of 2x2 cm were used as a substrate, onto which a polycrystalline copper layer with a nominal thickness of 150 nm was sputtered at a 1.3 Å s^{-1} rate with a base pressure of 3 µbar.

3.5. Drop-casting ionomer

The ionomer was deposited via a drop-casting method. For producing thin ionomer films, a perfluorinated resin solution containing Nafion was used from Sigma-Aldrich. This solution contained 5 wt% Nafion in lower aliphatic alcohols (80-85%) like 2-propanol and water (15-20%). The exact weight of a single Nafion polymer is not generally reported, instead the 'weight' is expressed in equivalent weight (EW), which is defined as the grams of dry polymer per ionic group (i.e. $g_{polymer}/mol_{ionic\text{-}group}$). The nafion ionomer had an EW of 1100. The concentrated 5 wt% nafion solution was diluted with methanol to a solution 0.1 wt%, and 20 µL was dropped on a 4 cm^2 surface, which gave a 4 µg cm^{-2} ionomer loading.

3.6. In-situ Atomic Force Microscopy

Studying the morphology on ionomer thin films on copper can give insight into the agglomeration and swelling behaviour of ionomers. A better understanding of the ionomer-ionomer and ionomer-catalyst interactions can lead to better designed catalyst layers for electrochemical CO_2R processes. Atomic force microscopy (AFM) is a type of scanning probe microscopy. It consists of a sharp probe mounted on a cantilever, piezoelectric driver and a position sensitive photo-detector. During operation, the sharp probe is brought into close contact with the sample and interacts with the surface so as to give information about the topology. With the use of piezoelectric elements, a constant force or height of the cantilever is maintained during operation. Any interaction of the sample with the tip is registered by monitoring the displacement of the free end of the attached cantilever. This displacement is measured by photo detector that receives a light signal reflecting from the cantilever of the probe.

The Bruker Dimension Icon from Bruker Corporation was employed as the atomic force microscope. This is a high performance AFM device that enables researchers to produce high resolution imaging at nano- to microscale. For imaging in air and fluid, ScanAsyst Air and Fluid probes were used respectively. PeakForce tapping mode was employed to unravel the sample's height profile and nanomechanical properties, like adhesion, modulus and dissipation. Nanoscope and Nanascope analysis software was used for operation and data processing, respectively.

The ionomer coated copper sample was placed on copper foil, inside a teflon frame and covered with transparent tape. A hole was carefully pre-cut into the tape, so the ionomer surface was exposed to the electrolyte and AFM tip. The frame was filled with CO_2-saturated 0.1M $KHCO_3$ and a nickel ring was placed inside the electrolyte as the counter electrode. The copper foil and nickel ring were electrically wired to a potentiostat to conduct electrochemical experiments (see figure 3.3).

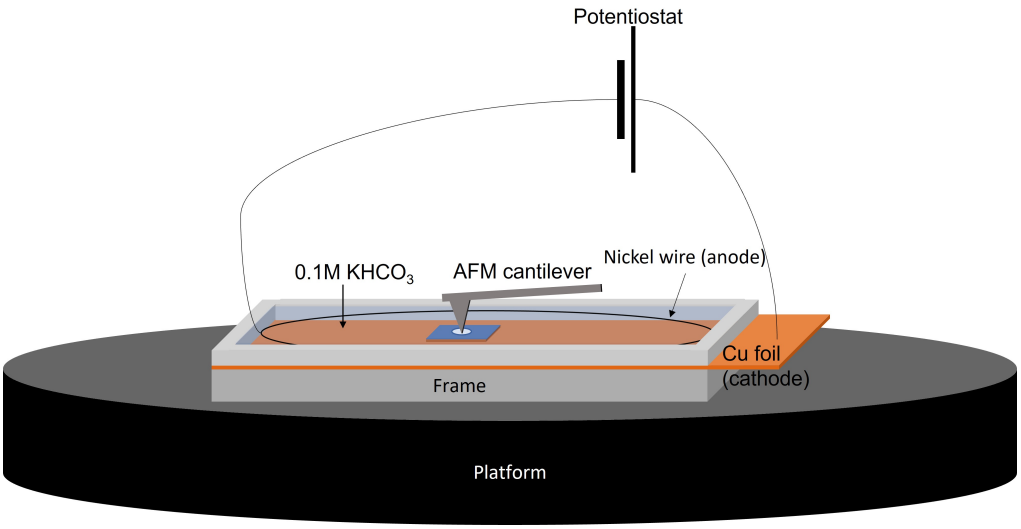

Figure 3.3: Setup for in-situ electrochemical AFM.

3.7. ATR SEIRAS

To study the ionomer-catalyst interfacial interactions, insights into the formation of intermediates and present species at the interface are critical. Infrared spectroscopy can provide these insights, and thus has been used to study CO_2R reactions [64–66].

The general working principle of absorption spectroscopy is based on the fact that chemical species absorb light at different wavelengths, resulting in a vibration. Since molecules have specific vibrational frequencies, it is possible to detect chemical species using this method. Raw data, a so called interferogram, contains interference of different signals, which can be mathematically differentiated by Fourier transformation to obtain actual absorption spectra, often referred to as Fourier Transform Infrared (FTIR). Attenuated total reflectance surface enhanced infrared spectroscopy (ATR-SEIRAS) is a technique where signal enhancement is achieved by functionalization of the crystal with a metal film. Infrared light passes through the crystal and is internally reflected at the copper electrolyte interface, while also producing an evanescent wave. At the interface, the evanescent wave excites surface plasmon polaritons at the Cu/electrolyte interface. This results in an increased electric field which decays exponentially from the surface. This increased electric field can increase absorption probabilities by an order of magnitude or even more.

ATR SEIRAS experiments were performed with a digital FT-IR spectrometer Vertex 70 by Bruker Optics. Germanium was used as ATR crystal, on which a thin copper layer of 40nm was sputtered (see figure 3.4b). A thin copper film of 40 nm was the appropriate thickness for i) measuring sufficient signal, ii) to not delaminate of Ge crystal surface. A graphite rod was used as counter electrode (anode) and a Ag/AgCl reference electrode was used to set the potential on the working electrode (Cu film, cathode) and measure the uncompensated resistance. A membrane-less setup was used, with $KHCO_3$ 0.1M solution (pH = 8.3) as electrolyte, which was saturated with CO_2 (pH = 6.8) at 10 sccm. A schematic can be seen in figure 3.4a. The measurements were done in the 1100-2400 cm^{-1} spectral range, with a resolution of 50 mV per spectrum.

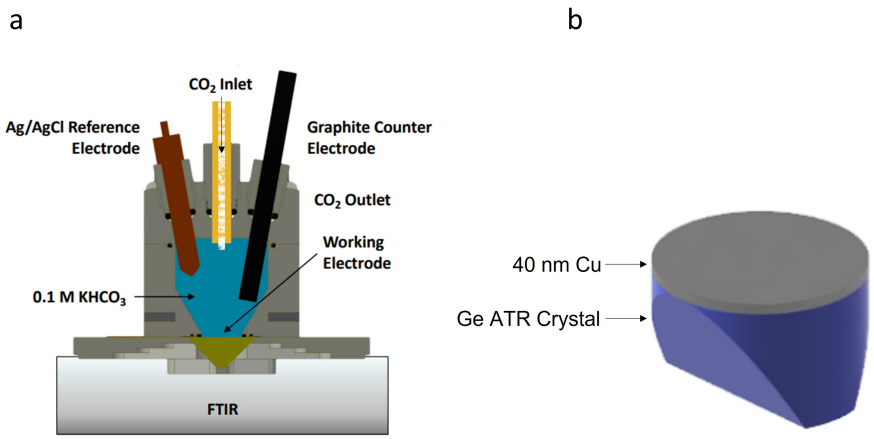

Figure 3.4: a) ATR SEIRAS experimental setup. b) Germanium crystal with a 40 nm thin layer of copper.

To control the working potential, a SP-200 Potentiostat from Biologic was used. EIS measurements were performed to determine the uncompensated resistance between the working (Cu) and reference electrode. Linear sweep voltammetry was performed, with steps of 50 mV per spectrum of 25 seconds from 0 V to -1.1 V vs RHE. Chronoamperometry measurements maintained a constant potential. More reductive potentials than -1.1 V vs RHE led to delamination of the copper foil from the Ge crystal.

3.8. XPS

X-ray photospectroscopy, or XPS, is a spectroscopy method that enables to quantify the elemental composition of surfaces. It relies upon Einstein's photoelectric effect, where an X-ray photon removes an electron from an atom. The kinetic energy of the removed photo-electron is measured by a so-called concentric hemispherical electron analyzer. The difference between the X-ray photon energy (known) and the kinetic energy of the ejected photo-electron (measured), the binding energy of the electron can be calculated. The binding energy is characteristic for the chemical nature of the parent electron, hence this gives information about the type of atom and thus the chemical composition of the surface. [67]

To study the surface chemical composition of the ionomer film, K-Alpha X-ray Photoelectron Spectrometer (XPS) System was used. This spectrometer allows to study samples in ultra-high vacuum. The Source gun type was a Al K Alpha, with a mean X-ray photon energy of 1486.69 eV [67], and a spot size of 400 µm. While the X-rays can penetrate more than 1 µm into materials, the depth of information (ejected photo-electrons) for this source of X-rays is somewhere between 1-12 nm. The pass energy, or the minimal energy required to detect photo-electrons, was 50 eV. An energy step size of 0.1 eV was used.

4

Results and Discussion

4.1. Elucidating ionomer morphology

We studied the ionomer morphology using atomic force microscopy. For all cases where the ionomer is used, a drop-casting method was used. The most important findings are:

- The nature of Nafion agglomeration depends on the dispersion solvent.
- The higher the ionomer concentration in the drop-casting solution, the smoother the surface becomes.
- The ionomer swells upon exposure to the electrolyte and the thin film is in the order of 20 nm - 30 nm.
- Negatively polarizing the Naf/Cu, leads to restructuring of the ionomer. It is proposed that the hydrophilic domains of the ionomer increase surface contact with the copper surface due to electrowetting, while the hydrophobic domains orient away from the surface.

4.1.1. Ionomer morphology of different loadings

We used atomic force microscopy to study the morphology of the ionomer on a copper surface. The copper surface was produced by plasma sputtering and had a nominal thickness of 150 nm. However, as one can see in figure 4.1, the maximum height difference in these figures is 400 nm, which was due to the rough surface onto which the layer of copper was sputtered. To study the ionomer morphology, a thin film had to be created so that distinct ionomer features could be identified. While a bare copper surface displayed a more rugged surface with smaller features, the addition of the ionomer smoothed

the surface. This could be seen from figure 4.1, where a comparison is made between ionomer coated surfaces. Evident from figure 4.1e is a nearly flat surface, which was produced with a 5 wt% ionomer loading. Using the density of dry Nafion at 25 °C, 2.05 g cm^{-3} [68], the film thicknesses were calculated with the equations below:

$$d_f = \frac{\rho_d \cdot w_f \cdot V_d}{\rho_{Naf} \cdot A_d} \tag{4.1}$$

where d_f is the estimated thickness of the film, ρ_d is the density of the dispersion, w_f is the weight fraction of the Nafion, V_d is the volume of dispersion dropped, ρ_{Naf} is the density of dry Nafion, A_d is the area covered by the dispersion. The ρ_d is calculated with the formula below:

$$\rho_d = w_f \cdot \rho_{Naf} + w_{f,s} \cdot \rho_s \tag{4.2}$$

where $w_{f,s}$ is the weight fraction of the solvent, ρ_s is the density of the solvent.

With the formula's above, the estimated thin film thicknesses were estimated (see caption of figure 4.1). In this thesis we studied the ionomer's dynamic morphology change during CO_2R. As one can see, the surfaces of figures 4.1d,e are nearly flat on this scale. We assumed these surfaces would not result in any observable restructuring during CO_2R conditions, due to the thicknesses of the films. Figures 4.1b,c showed more roughness and its thicknesses were in the thin film region (< 100 nm). As these films were closer to the catalytic surface, it was expected that any restructuring of the ionomer would be observable, hence they were chosen as suitable for studying the ionomer morphology.

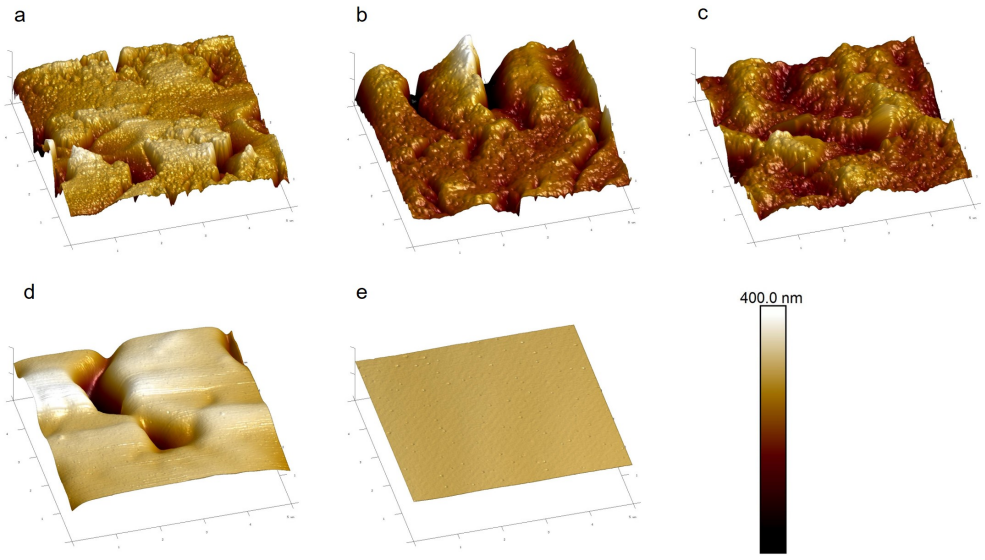

Figure 4.1: AFM images of ionomer on copper. a) bare copper, b) 0.05wt%, c) 0.1wt%, d) 1wt% , e) 5wt% ionomer. The density of dry Nafion: 2.05 g cm^{-3} [68]. The estimated film thicknesses were b) 38 nm, c) 77 nm, d) 770 nm, e) 4170 nm. Propanol was used as the solvent. Image size 5x5 micrometer.

4.1.2. Effect of solvent on morphology of Nafion film

When drop-coating ionomer thin films onto a substrate, the solvent impacts the nature of agglomeration (see chapter 2.3.8). We decided to compare iso-propanol and methanol solvents as dispersion media. Figure 4.2 shows the height images of bare copper and the ionomer coated samples. While the locations of these samples were different, general typical features were observed (indicated by the yellow circles). We noticed bigger Nafion agglomerates with IPA, than with MeoH. This observation is consistent with the findings by Paul [62], where the more polar the solvent (methanol > iso-propanol), the more the ionomer was inclined to minimize the surface area on the substrate and the flatter the surface. Besides qualitative observations, the difference in surface roughness can be expressed quantitatively by the arithmetic average roughness Ra (see values for average roughness in caption of figure 4.2). Below the formula for average roughness Ra, the arithmetic average of the absolute values of the surface height deviations measured from the mean plane.

$$Ra = \frac{1}{N}\sum_{j=1}^{N}|Z_j| \tag{4.3}$$

where N is the number of points evaluated, Z_j is the height of each point. We choose to continue with the ionomer dispersion in MeOH for this thesis, because i) it seemed to produce a more evenly coated ionomer thin film than IPA, ii) both MeOH and IPA could be suitable for studying the ionomer morphology. The experiments described in the following chapters, used thin films produced with drop-casting from a methanol solvent.

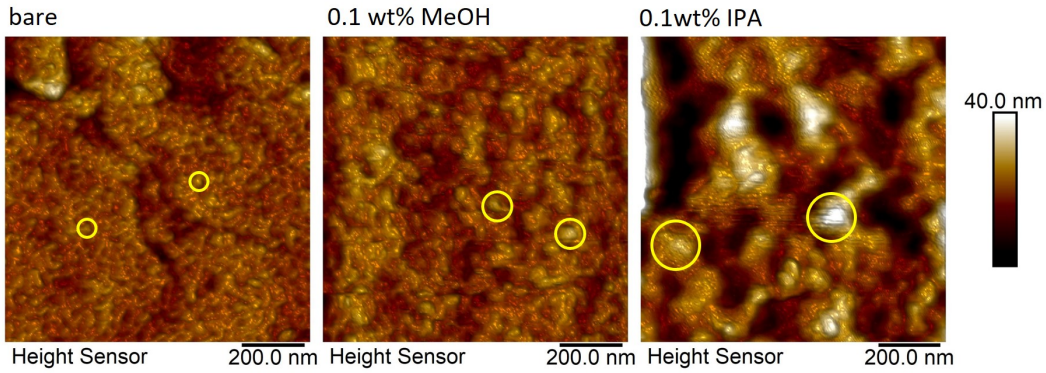

Figure 4.2: AFM height images of bare copper and drop-casted 0.1wt% Nafion dispersions on copper in methanol and iso-propanol solvent. The average roughness from left to right: 1.5, 2.2, 5.3 nm. Image size 1x1 µm. Height images made with ScanAsyst Fluid+ AFM probes in 0.1 M $KHCO_3$ electrolyte. Note that these were different spots, on the same sample. The general features are however representative.

4.1.3. The evolution of bare copper surface under electrochemical conditioning

The bare copper surface was studied under a low current density of 2.85 mA cm^{-2}. Operando measurements, in this context meaning simultaneously applying electricity and imaging, was not possible due to significant distortion of the AFM probe by formed bubbles at the surface. Instead, in-situ mea-

surements were performed, meaning the same location of the sample before and after electrochemical conditioning. Unfortunately it was not possible to produce more images, because of inevitable drift of the sample spot after retracting the AFM probe. Nevertheless, the results already reveal changes to the copper surface after 600 seconds.

After 600 seconds of electrochemical conditioning, the roughness of the copper increased, as can be seen in the graph on the right in figure 4.3. Further conditioning, lead to an even rougher copper surface. This is consistent with the findings several studies [69–71], where it was found that reduction of copper oxide led to a rougher surface with more uncoordinated sites. While the oxidized states of the copper were not researched in this thesis, it is well-established that copper rapidly oxidizes in air [16, 31]. This inevitable oxidation most definitely influences the restructuring of the copper during electrochemical conditioning. Generally, reduction of these oxidized states of Cu lead to rougher surfaces, which increases active surface area and thus the activity of the Cu [16, 34, 35, 72]. Also exposure to the water molecules is expected to result in oxidation.

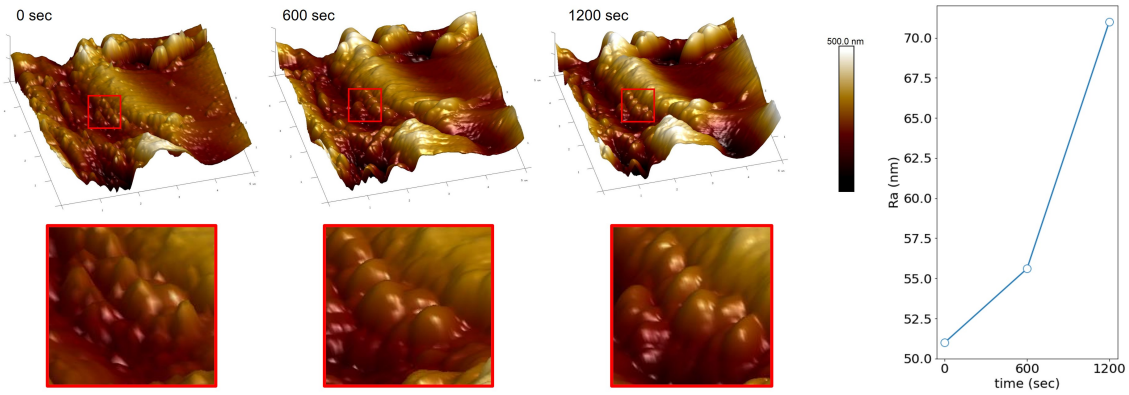

Figure 4.3: This time sequence shows the same location on a bare copper sample under negative conditioning. Image size is 5x5 micrometer. A constant current of 2.85 mA cm^{-2} was applied.

4.1.4. Electrolyte effect on ionomer morphology

The effect of the electrolyte on ionomer thin film morphology was studied using AFM. A bare copper surface (figure 4.4 Bare) was imaged before applying a thin film coating (figure 4.4 Nafion), using a drop-casting method. The ionomer loading was estimated to be 4 µg cm^{-2}, with an estimated thickness of 20 nm, calculated using equations 4.1 and 4.2. The addition of the ionomer resulted in a thin film atop of the copper, which can be seen in figure 4.5. The hilly features, indicated by the white angled arrows on the bare copper image in figure 4.5, became less well distinct from each other when the ionomer was added. On the right side of figure 4.5, a plausible explanation for this is shown. The ionomer coating covers the surface, hence filling the gaps between edges. As the electrolyte is added to the surface, the hilly features seem to grow smaller in size. This might well be a result of the ionomer absorbing water and swelling to grow in size. This swelling ionomer layer covers the underlying copper, which results in vanishing of these hilly features on the surface. This observation is visible among other hilly features spread across the surface as well.

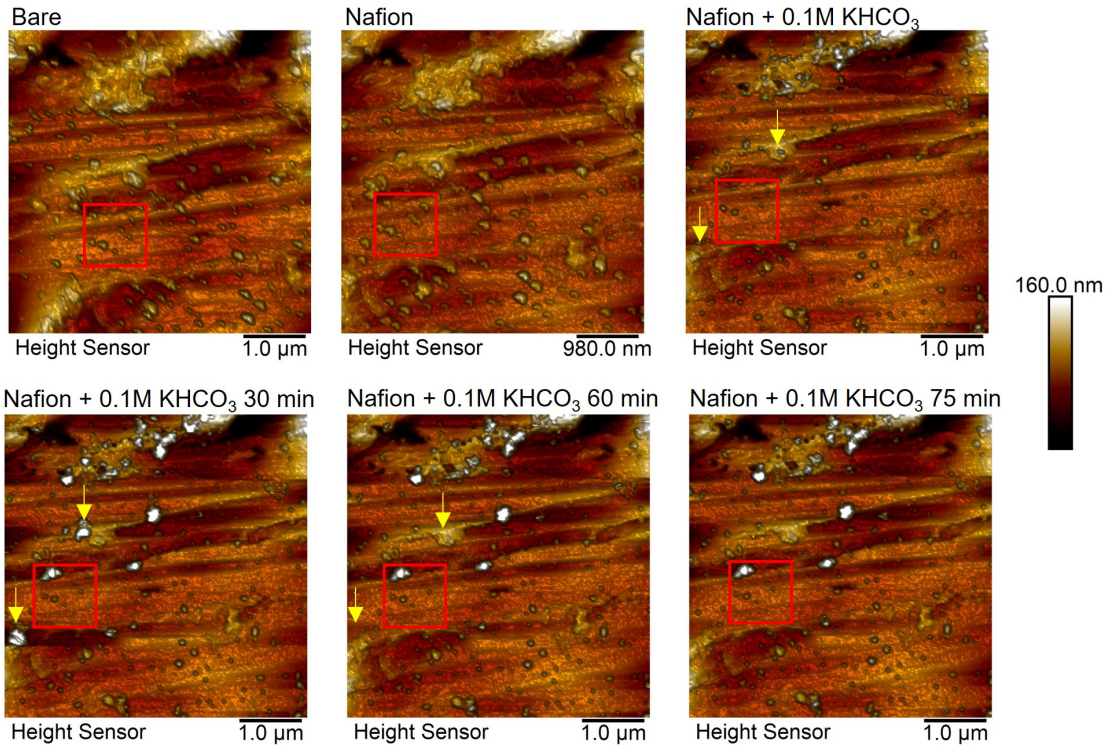

Figure 4.4: In situ AFM scans of bare copper coated with ionomer. The red squares are zoomed-in in figure 4.5. Average roughness Ra for bare copper = 12 nm, Nafion coated = 10.3 nm, Nafion coated + 0.1M $KHCO_3$ = 10.3 nm, Nafion coated + 0.1M $KHCO_3$ after 30 min = 12.1 nm, Nafion coated + 0.1M $KHCO_3$ after 60 min = 11.3 nm, Nafion coated + 0.1M $KHCO_3$ after 7 min = 11 nm. Bare and Nafion scans were made with ScanAsyst Air probe, the other scans with ScanAsyst Fluid+ probe.

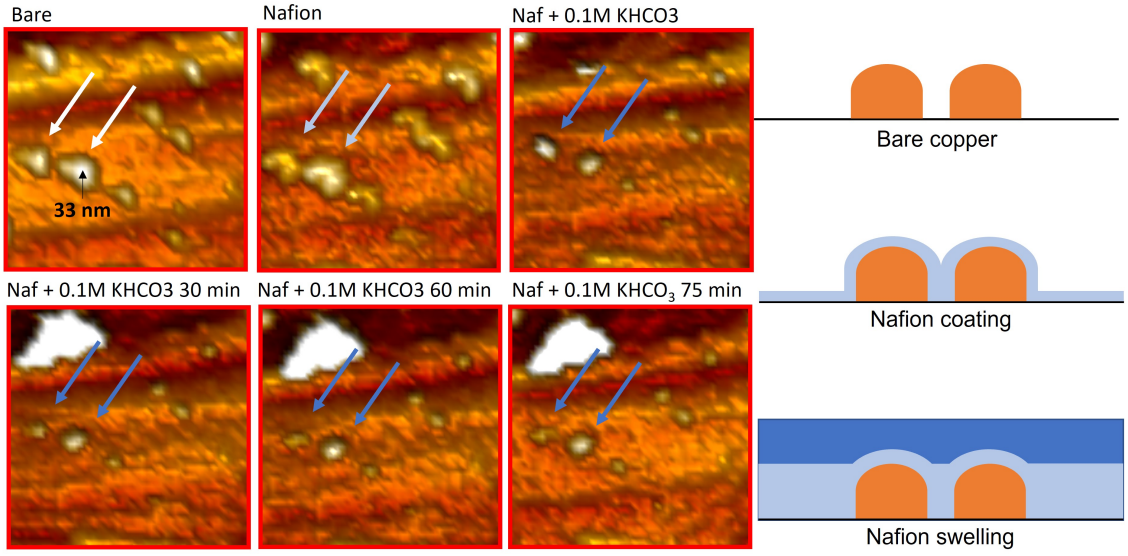

Figure 4.5: Swelling model for Nafion. These images are zoomed selections of the scans in figure 4.4. The feature indicated by 33 nm is with respect to its base.

For bare copper the hilly features in figure 4.5 are ≈ 33 nm with respect to its base. In comparison, the estimated calculated thickness (using equations 4.1 and 4.2) of the dry ionomer is 19.5 nm, and

increases to 26.7 nm when the ionomer maximally swelled (density of fully swelled Nafion is $\approx$ 1.5 g cm^{-3} [68]). It should be noted that the exact ionomer film thickness could not be deduced from these images, since the ionomer is expected to not only coat the hilly features, but also the flat surface. However, since the tops of the hilly features can still be seen when the ionomer is added, we deduce the ionomer is in the order of the height of these Cu hilly features.

Finally another interesting observation is the appearance of the white granules (see yellow arrows pointing down vertically), which appear after 30 min of exposure to the electrolyte. After 60 min some of these particles seemed to have disappeared, which suggest some sort of mobile contaminant particle and not part of the ionomer.

4.1.5. Ionomer restructuring during CO2R

In order to study the ionomer morphology as constant current was applied, in-situ AFM was applied. Under these CO_2R conditions, the ionomer morphology changed significantly. From figure 4.6 it can be seen that before inducing CO_2R conditions, a network of interconnected ionomer features can be seen. After 600 seconds of constant current conditioning, these features seem to disappear. Either the ionomer network restructured during CO_2R, resulting in a smoother surface or the ionomer parted from the copper surface to some degree. XPS measurements showed a lower ionomer signal (see chapter 4.5), which suggests ionomer dissolution to some degree.

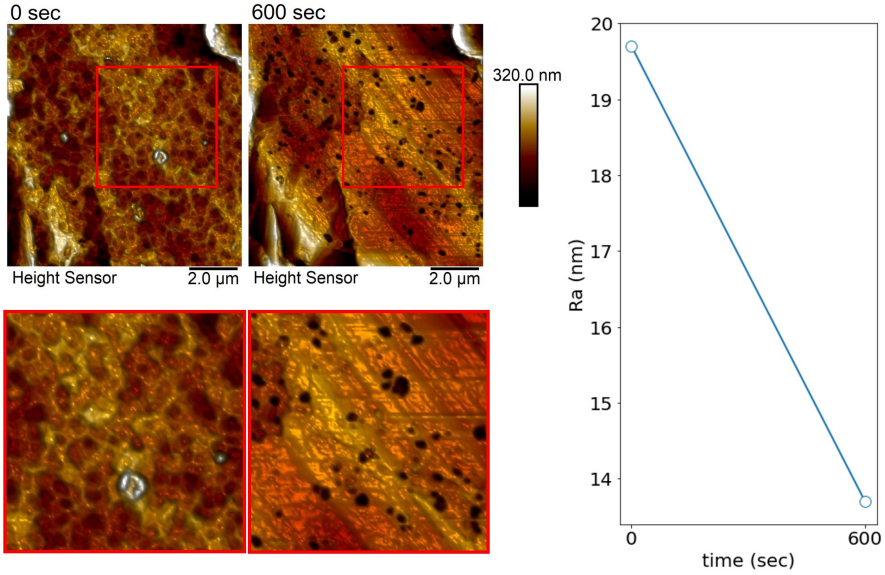

Figure 4.6: In-situ AFM images of ionomer-coated copper after applying constant current. 0.1 M $KHCO_3$ electrolyte, saturated with CO_2 was used. Red squares indicates the area over which the average roughness Ra, respectively 19.7 and 13.7 nm from left to right. was determined. Ionomer loading was 8 µg cm^{-2}, constant current of 2.85 mA cm^{-2} was applied. ScanAsyst Fluid+ probe was used.

In figure 4.7 a similar evolution of the ionomer is visible. Before applying a negative polarization on the copper electrode, relatively large agglomerates can be observed, which become smaller after 600

seconds of electro-conditioning. The ionomer seems to reorganize due to electro-conditioning of the copper. The ionomer surface initially becomes more rugged after 300 seconds of applying a constant current, and becomes smoother after more than 600 seconds of applying constant current. To link this micro-observation to the nanoscale phenomena, what follows is a proposition on the orientation of the ionomer aggregates. Nafion thin films (< 100 nm) form multilamellar structures on metal surfaces (figure 2.13) [47]. As the copper surface becomes more hydrophilic when negative polarization is applied, due to electrowetting properties [73], the orientation of the ionomer backbones become more horizontally aligned with the copper (see figure 2.13), where the hydrophilic side chains are perpendicular to the copper surface. Here the sulfonate groups, solvated in the hydrophilic domain, have a stronger interaction with the increasingly hydrophilic copper substrate expected by electrowetting theory. Due to confinement effect of thin films, the top layer of the thin film follows the same trend, hence resulting in a flatter surface as observed by AFM. The horizontal orientation of the backbones was investigated by Kusoglu *et al.* [60], where they used in-situ grazing-incidence X-ray scattering (GISAXS) for nanostructural characterization of thin films.

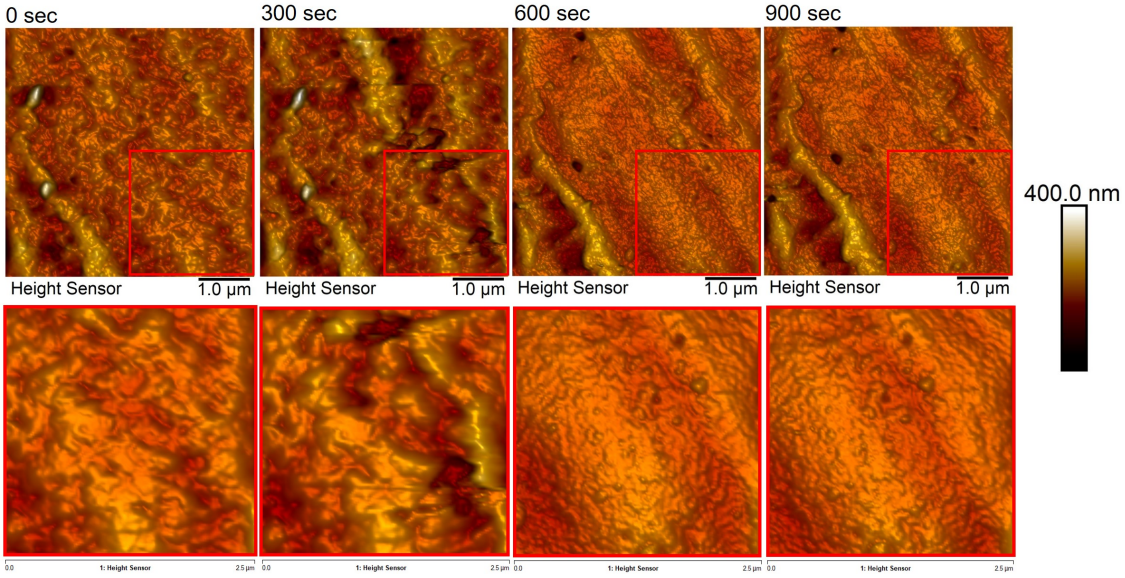

Figure 4.7: Time sequence of Nafion morphology on copper. The image size for the top row is 5x5 µm, the bottom row is 1x1 µm. Average roughness of the bottom row from left to right: 10.3, 17.6, 9.83, 8.66 nm. The Nafion loading was 8 µg cm^{-2}. A constant current of 2.85 mA cm^{-2} was applied.

Interestingly, this is in contrast with the results from bare copper surface roughness as a function of electro-conditioning (see figure 4.3), which show the exact opposite trend, i.e. the surface becomes rougher by applying a negative polarization on the copper. These results show that the ionomer coating smooths out during CO_2R conditions, proposedly due to the horizontal alignment of the ionomer. As has been explained in chapter 4.1.4, the estimated thin film thickness is between 20 and 30 nm. While the thickness is not confirmed by experimental methods in this thesis, the decline in ionomer intensity observed by XPS (see chapter 4.5) suggests partial ionomer dissolution. In the bottom part of figure 2.13 in chapter 2.3.7, this dissolution mechanism is shown.

4.2. Effect of ionomer on local reaction environment

The chemical interface between the ionomer and copper was studied using ATR-SEIRAS. The most important findings are:

- Nafion enhances adsorption of both atop-CO and bridged-CO. Atop-CO is considered the reactive species, in contrast with bridged-CO.
- The energy of the metal-C bond becomes stronger as potential is increased, resulting in a lower energy of the CO stretch vibration due to conservation of energy. This is observed by a red shift of atop-CO.

4.2.1. Nafion enhancing CO adsorption on Cu

In figure 4.8a and 4.8b the absorbance spectrum for Nafion coated and bare copper is shown respectively, as a function of applied potential. Here, absorbance is a measure of absorption of light with a certain wavelength by a species, and the wavenumber is defined as the number of wavelengths per unit of distance (cm). These results show how the absorbance of CO_2 ($\approx$ 2345 cm^{-1} [74]) and CO ($\approx$ 2100-1900 cm^{-1}) [65] change as a result of increasing potential of the copper surface. Multiple sources assigned the 2345 cm^{-1} to an asymmetric stretch of CO_2 [74–76]. Hence, the decreasing signal of this band indicates the disappearance of CO_2.

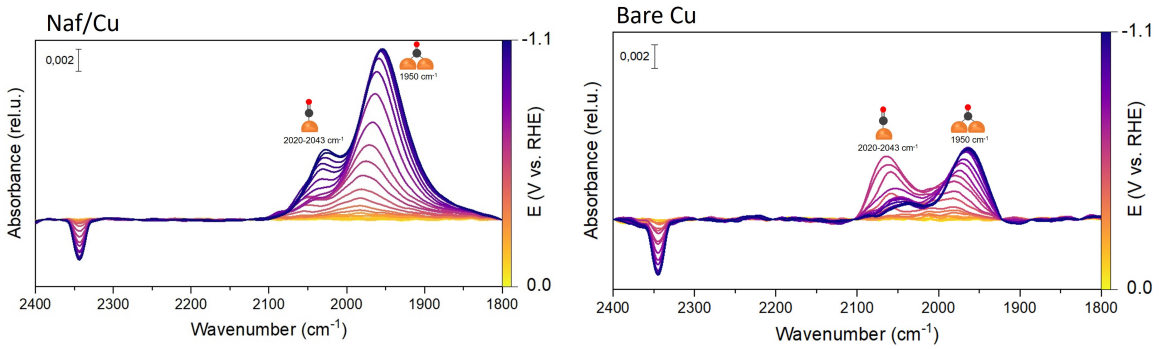

Figure 4.8: Left: Absorbance spectrum of Nafion coated Cu during CO_2R. Right: Absorbance spectrum of bare Cu. A 40 nm layer of copper was sputtered on a germanium crystal.

According to the Computational Hydrogen Electrode (CHE) approach, the proton-electron transfer of *CO is regarded as the potential-limiting step of CO_2R towards ethylene [37, 77, 78]. This makes the *CO a critical intermediate towards the formation of ethylene. What stands out from figure 4.8 is the increased absorbance of two CO bands (2100-1900 cm^{-1}) when a Nafion coating is applied on the copper, with respect to the bare copper. An increased absorbance of CO, could lead to a higher degree of dimerization, which is observed by the results in chapter 4.3. The CO intermediate can be adsorbed in different ways on the copper surface. In this text a distinction is made between atop-CO and bridged-CO, the former being adsorbed on one single copper atom and the latter on two or more copper atoms. Experimental and DFT calculations have pointed out atop-CO vibrational frequency in

the region 2100-2000 cm^{-1} and bridged-CO between 1900-1750 cm^{-1} [64, 66, 76, 79].

For bare copper (figure 4.8b) the band between 2100-2000 cm^{-1} initially increases, meaning more adsorption and declines when the potential is increased further, indicating reversibility. This change as the potential increases indicates the reactivity of this atop-CO species. For the Nafion coated Cu (figure 4.8 Naf/Cu), the absorbance of this band consecutively increases as potential is increased, indicating stabilization of this species. This stabilization is proposed to be due to the presence of the Nafion, which effectively promotes the formation to the products originating from this *CO species, observed from the results in chapter 4.3. We have three hypotheses that could explain this stabilization.

Firstly, desorped gaseous products could experience increased transport resistance through the membrane, compared to the aqueous bulk [6, 47]. The permeability, which is equal to the solubility S_{gas} [mol cm^{-1} s^{-1}] multiplied by the diffusion coefficient D_{gas} [cm^2 s^{-1}]:

$$P_{gas} = S_{gas} \cdot D_{gas} \tag{4.4}$$

P_{gas} for CO(g) in a Nafion membrane is $2.82 \cdot 10^{-12}$ mol cm^{-1} s^{-1} [80] versus $2.07 \cdot 10^{-11}$ mol cm^{-1} s^{-1} [81] in water. CO thus permeates 7.3 times slower in Nafion than in water. This could result in accumulation which could enhance re-adsorption of the products. Re-adsorption of CO for example, could lead to a higher degree *CO coverage, which leads to higher C-C coupling.

A second plausible explanation is that the Nafion results in an increased cation concentration in the local reaction environment to maintain electro-neutrality. Cations are known to influence CO_2R significantly [15, 72]. The increased cation concentration could stabilize the *CO intermediate and explain the observations of increased yields of ethylene, methane and carbon monoxide.

Thirdly, the sulfonate group could form dipole-dipole interactions with *CO. These interactions could stabilize the *CO intermediate and result in a higher product yield of ethylene, methane and carbon monoxide. Pan & Barile [7] proposed something similar, where the Nafion stabilizes the *CO intermediate.

2000-1900 cm^{-1} region

The other band is in the region of 2000-1900 cm^{-1}. Multiple sources assigned $CO_{bridged}$, considered an inert intermediate, to the band region 1900-1750 cm^{-1} [64, 66, 76]. From the results in figures 4.8a,b, there is no band between 1900-1750 cm^{-1}. However, the intensity of this peak (2000-1900 cm^{-1}) in both figures, irreversibly increases which could be an indication of the inert CO_{bridge}. From the heat maps in figure 4.9, one can see that the intensity of the 2000-1900 cm^{-1} band barely decreases as the potential goes to 0 V. This suggests that the adsorbed CO in this region is inert and does not contribute to CO_2R.

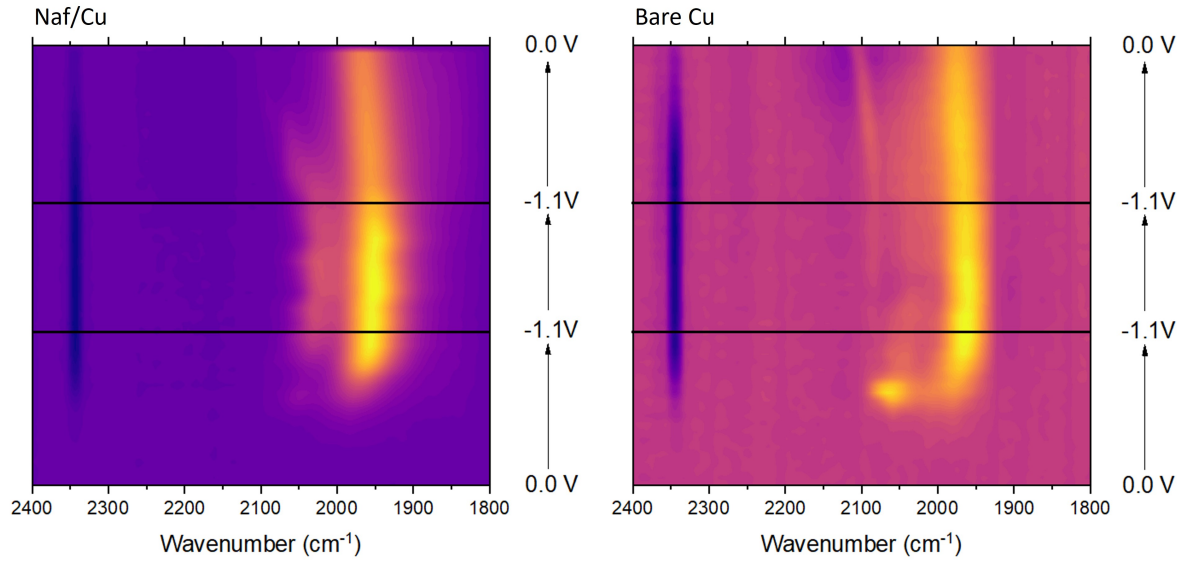

Figure 4.9: Absorbance heatmaps of Nafion coated copper (a) and bare copper (b).

Furthermore the heatmaps show a shift of the atop-CO to a lower wavenumber (moving to the right) as potential becomes more negative. Since the wavenumber is inversely proportional to the wavelength, this is a red shift and indicates a lower energy. This makes sense, since the metal-C bond increases in strength as potential is more negative, making the C-O stretch vibration lower in energy due to conservation of total vibrational energy. This red-shift is consistent with DFT calculated CO-stretch frequencies made by Gunathunge *et al.* [79].

4.2.2. Intermediate and carbonate region

Some important CO_2R intermediates are found in the region between 1600 and 1200 cm^{-1} [64, 74, 76]. DFT calculations performed by Katayama *et al.* [64] on Cu(111) revealed the following bands for adsorbed intermediates: $CO_{3,ad}$ at 1533 cm^{-1}, HCO_{ad} at 1477 cm^{-1}, $OCH_{3,ad}$ at 1396 cm^{-1}, $OC_2H_{5,ad}$ at 1321 cm^{-1}, $HCOO_{ad}$ at 1298 cm^{-1}. In figure 4.10 these intermediates are assigned to the corresponding peaks. Besides the CO_2R intermediates, presence of carbonate and bicarbonate species is also likely. Solution based carbonate (CO_3^-) typically has a band center at 1395 cm^{-1} [65, 82], which overlaps with the $OCH_{3,ad}$ at 1396 cm^{-1}, making it hard to distinguish these species. Same is true for bicarbonate, which finds its vibrational frequencies of COH bend between 1300-1320 cm^{-1}, symmetric CO_2 stretch around 1355−1364 cm^{-1} and symmetric CO_2 stretch around 1626 cm^{-1} [65, 82].

Hanawa *et al.* [83] assigned SO_3^- stretching mode from Nafion to 1060 cm^{-1}, unfortunately not present in spectrum 4.10 Naf/Cu, due to limited range of the Ge crystal that was used. Furthermore they found CF_2 vibrations related to the perfluoro couples in the backbone and side-chain between 1250-1100 cm^{-1}. The increasing shoulder between 1250-1200 cm^{-1} could indicate an increased absorbance of this CF_2 group near the surface. Because CF_2 is both present adjacent to the SO_3^- in the side-chain and in the perfluoro backbone, we could not deduce the ionomer orientation from this observation.

The bands between 1800-1600 cm^{-1} can be observed in both spectra, hence is not ionomer indicative. The related species could not be identified. The peak at 1533 cm^{-1} and 1477 cm^{-1} were assigned to $CO_{3,ad}$ and HCO_{ad} respectively. At 1396 cm^{-1}, corresponding to $OCH_{3,ad}$, there are no changes in absorbance observed in both spectra, indicating steady state or absence of this species. The decreasing peak at 1321 cm^{-1} is assigned to $OC_2H_{5,ad}$, an intermediate of ethylene, which shows a higher decreasing absorbance in the ionomer figure (Naf/Cu). The lower absorbance, starting below -1 V, of this intermediate indicates the beginning of desorption and thus formation of ethylene. This hypothesis is consistent with formation of ethylene at the Naf/Cu sample at around -0.81 V (figure 4.11).

The peak at 1298 cm^{-1} was assigned to $HCOO_{ad}$, where the intensity increases with the addition of the ionomer. From the reaction mechanism in chapter 2.2.2, one can see that $HCOO_{ad}$ is a crucial intermediate in the formation of formate. Furthermore when looking closely at this peak, one can see the absorbance at the highest potential (dark purple) is slightly lower than a previous potential (lighter purple), which indicates the reactivity of this species. The evolution in absorbance of this species supports the relatively high yield of formate in chapter 4.3.

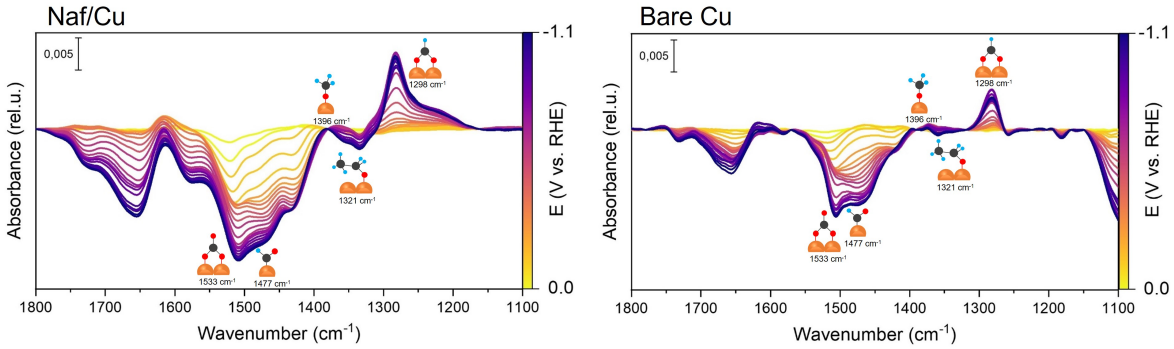

Figure 4.10: ATR SEIRAS spectra of common carbonate intermediates region during CO_2R. Left: ionomer coated copper, Right: bare copper.

4.3. Effect of the Nafion thin film on activity and selectivity

A flow cell was used to determine the effect of the ionomer on CO_2R. Five products were identified: H_2, CO, CH_4, C_2H_4 and $CHOO^-$. For analysing the gaseous products a GC was used, for liquid products both HPLC and H-NMR were employed. Formate was the only product identified from HPLC, which was confirmed by H-NMR. From the H-NMR also traces of ethylene glycol and methanol were identified (see appendix 6.1), but with insignificant amounts. HPLC was used for quantification of the only liquid product, formate. No ethanol was formed, confirmed by HPLC and H-NMR.

In the following sections, the ionomer coated sample is referred to as 'Naf/Cu' and bare copper 'Cu'. The most common product formed at the least negative potential -0.8 V for Naf/Cu and Cu, is formate and switches to hydrogen as the negative polarization is increased for both the Naf/Cu and Cu. This suggest that at higher potentials the tendency for HER is favored over CO_2R. Note that at the least negative potential almost exclusively hydrogen and formate was formed, and the Faradaic efficiencies at the two least negative potentials don't add up to 100%. This could be due to evaporation of products after prolonged storage of liquid samples not perfectly sealed.

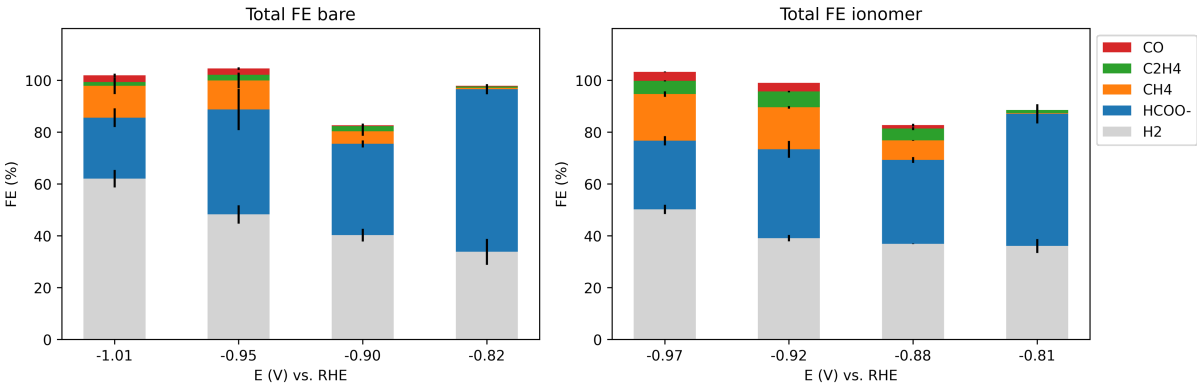

Figure 4.11: Accumulated faradaic efficiencies per potential for ionomer-coated (left) and bare copper (right). Note that the potential on the x-axis is spaced evenly, which is not the actual spacing.

4.3.1. CO, C_2H_4 and CH_4 product distribution

Ethylene and carbon monoxide production was higher for the Naf/Cu sample across all potentials, with an exception for the least negative potential. While there seems to be only a slightly higher activity and selectivity towards CO with the Naf/Cu, the enhanced activity and selectivity towards C_2H_4 with Naf/Cu is undisputed. This suggests that the Nafion layer stabilized the *CO intermediate, an important intermediate for the formation of C_{2+} products. This is supported by observations made by ATR-SEIRAS (chapter 4.2.1), which showed a clear increase in absorbance of CO_{atop} and CO_{bridge}. Since atop-CO is a fundamental reaction intermediate of the mechanisms towards CO, CH_4 and C_2H_4, the increased absorbance explains the higher production to CO, CH_4 and C_2H_4. The enhanced stabilization of the atop-CO intermediate allows for a higher degree of C-C coupling, leading to more ethylene, or alternatively a higher degree of proton-electron transfer steps leading to CH_4. A study by Pan & Barile [7], in

which a remarkably high methane production was achieved (88%), suggested that a Nafion overlayer stabilized the *CO reaction intermediate which can be further reduced to methane. They proposed that the sulfonate groups in Nafion stabilize the CO intermediate through hydrogen bonding interactions. The results in chapter 4.2.1, confirm stabilization of the *CO intermediate, while the exact mechanism remains elusive.

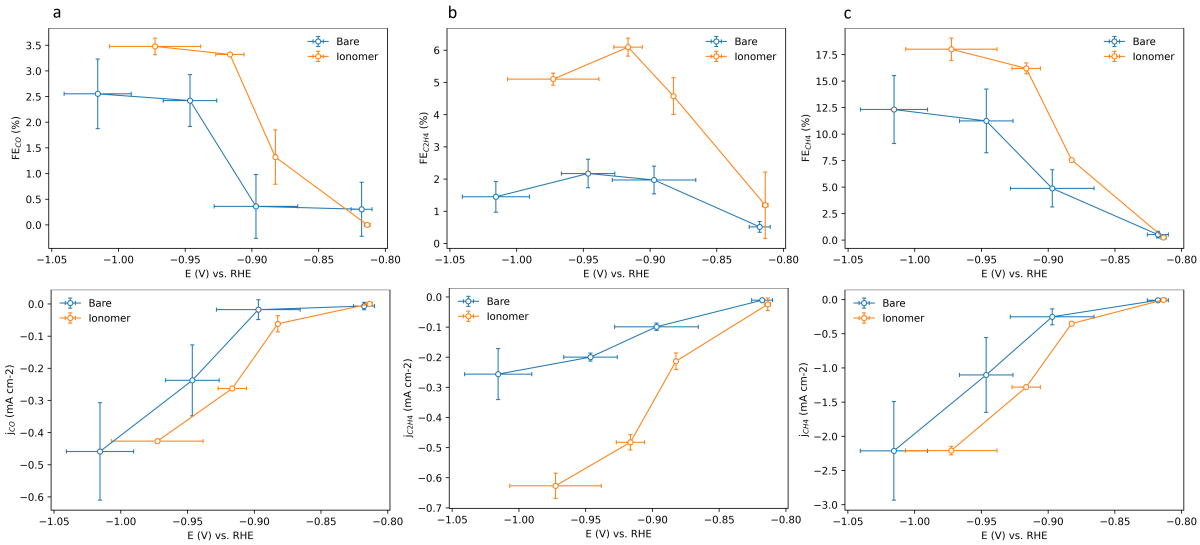

Figure 4.12: Faradaic efficiencies and partial current densities towards carbon monoxide (column a), ethylene (column b) and methane (column c).

4.3.2. H_2 and $HCOO^-$ product distribution

In figure 4.13 the FE and partial current density (j) of H_2 and $HCOO^-$ is shown. The ionomer showed strikingly similar activity towards hydrogen, while there seems to be a slight difference in formate activity, where bare Cu shows higher formation. Hydrogen formation starts with a proton-electron adsorption, the so-called Volmer step [84]. Subsequently this *H intermediate can combine with another adsorbed proton to form hydrogen (Tafel step), or a CO_2 molecule can be inserted into the metal-H bond to form an intermediate that eventually leads to formate upon desorption. Alternatively formate can be formed starting with the adsorption of CO_2 with two metal-O bonds. Similar activities at less reductive potential towards towards hydrogen and formate, indicate that the ionomer does not affect these reactions. There seems to be a suppression of formate evolution at more reductive potentials by the Naf/Cu. This difference increases even more when considering the intrinsic activity in the next chapter.

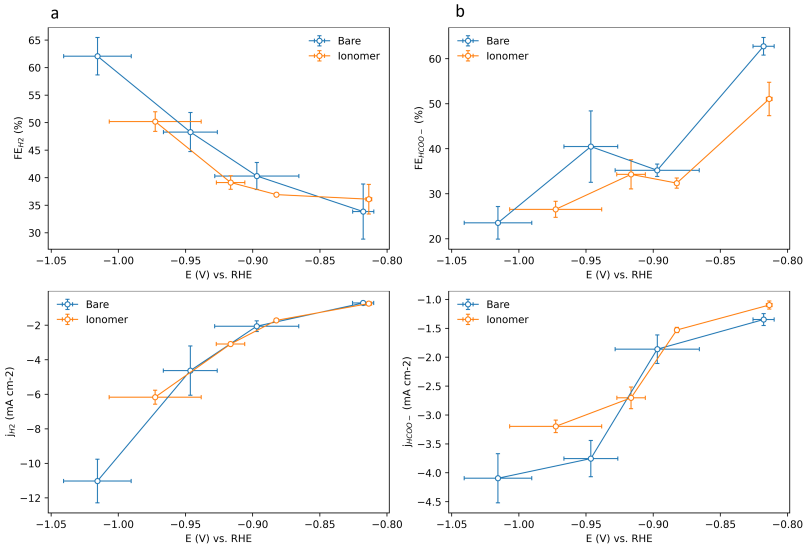

Figure 4.13: Faradaic efficiencies and partial current densities of hydrogen (column a) and formate (column b).

4.4. Intrinsic activities

The figures in 4.14 show the intrinsic activities, calculated using the the active surface areas shown in table 4.1. Ethylene shows biggest difference in intrinsic activity between the ionomer coated and bare copper. Across the entire potential range from -0.8 to -1.05, the formation towards ethylene is higher. Also formation towards CO and CH_4 seems to be a bit higher with the ionomer, even with considering the standard deviations. The difference in intrinsic activity towards hydrogen seems to increase as potential becomes more reductive, but unfortunately lacks more data points to confirm this. Formate production seems to be suppressed by the ionomer at the more reductive potentials.

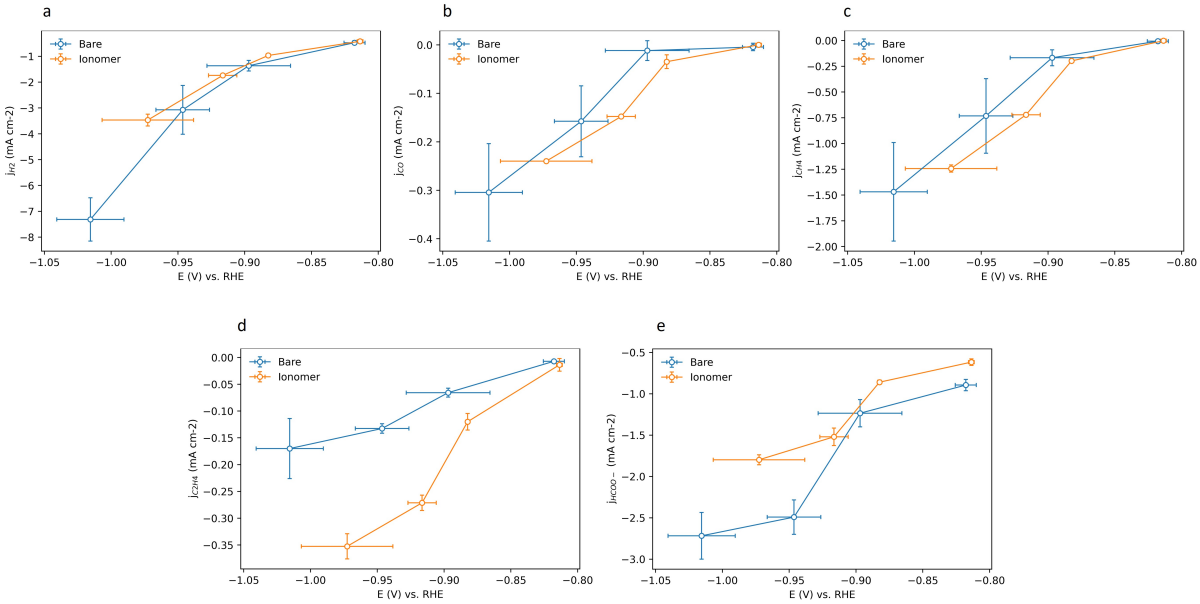

Figure 4.14: Intrinsic activities of a) hydrogen, b) carbon monoxide, c) methane, d) ethylene, e) formate.

4.5. Chemical composition analysis

XPS was used to study the chemical composition of the ionomer surface. In figure 4.15 shows an analysis of the atomic ratio's before and after CO_2R in the flow cell (see chapter 3.1). From this analysis, some conclusions can be drawn about the chemical composition and thickness of the Nafion layer. Firstly, the error bars show the variation of atomic ratio's at 6 random spots at the surface that were used for this analysis. Since there is little variation, it can be safely assumed that the data is representative for the average surface of the Naf/Cu. Secondly, since there is a copper signal before and after CO_2R and assuming the depth of information for the X-Ray source is 1-12 nm, it can be concluded that the thickness of the thin Nafion film is somewhere in this order. The drop-casting method, that has been used in this research, is known to produce an inconsistent layer thickness [47]. The estimate of a 20-30 nm layer thickness made in chapter 4.1.1 seems plausible, since the spot of evaluation for XPS is $\approx$ 400 µm in diameter, and less dense regions could be somewhere between 1-12 nm, hence photo-electrons from copper are detected. Moreover, since the fluorine atom is fairly specific to Nafion, the atomic ratio analysis of fluorine (F1s) gives an indication about the amount of Nafion on the surface. Furthermore, the atomic ratio of Cu (Cu2p) is an indication of the thickness of the ionomer layer, a lower atomic ratio of Cu indicates a thicker ionomer layer and vice versa. When comparing the F/Cu ratio, 14.3 for the sample before CO_2R and 0.72 after, it indicates that there is less ionomer present at the surface after CO_2R. For thin films with this thickness, ionomer delamination after a few hours of reaction operation, is not out of the ordinary. Another observation from the atomic ratio's, is a significant increase in C1s and O1s, which is indicative for adsorption of *CO, or other oxygenated carbon species. This might be another indication that bridged-CO is indeed inert and still present on the copper surface after CO_2R.

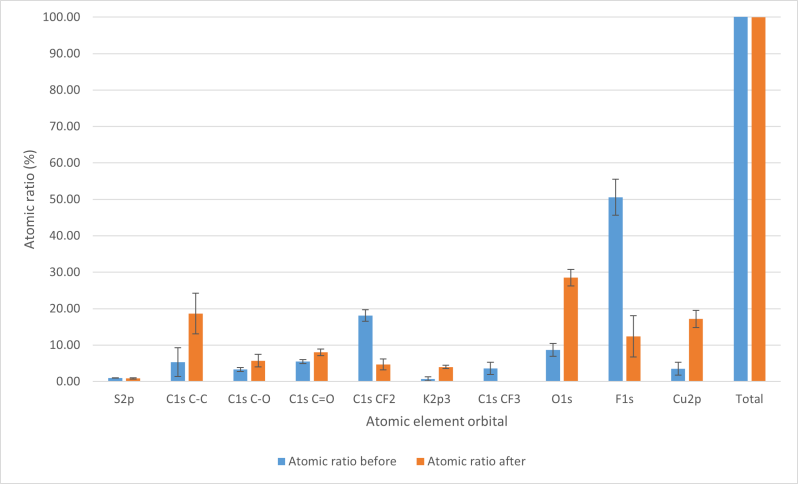

Figure 4.15: Comparison between atomic ratio's of Naf/Cu samples before and after experimental work. Chronoamperometry was performed at 4 potentials, each with a duration of 1800 sec. The data of four Naf/Cu samples were averaged in this analysis, each evaluated at three different spots of 400 µm in diameter. In appendix 6.2, two XPS survey spectra shown as example.

4.6. Relative double layer capacitance

Capacitance measurements were performed to elucidate the electrochemical active surface area before and after experiments. The capacitance is defined as the ratio of the amount of electric charge stored on a conductor to a difference in electric potential, which can be determined by plotting out the current [C/s] vs the scan rate [mV s^{-1}]. In figure 4.16 one can see these measurements, where the blue lines are before the CO_2R experiment, and orange is after. The capacitance for bare Cu (4.16a) before CO_2R is 0.157 mF, and after it increased to 0.237 mF, corresponding to a 50% increase. The bare Cu surface restructures during CO_2R, which is consistent with the AFM observations in chapter 4.1.3, where the average roughness increased. The increased roughness is proposed to give rise to the increased capacitance.

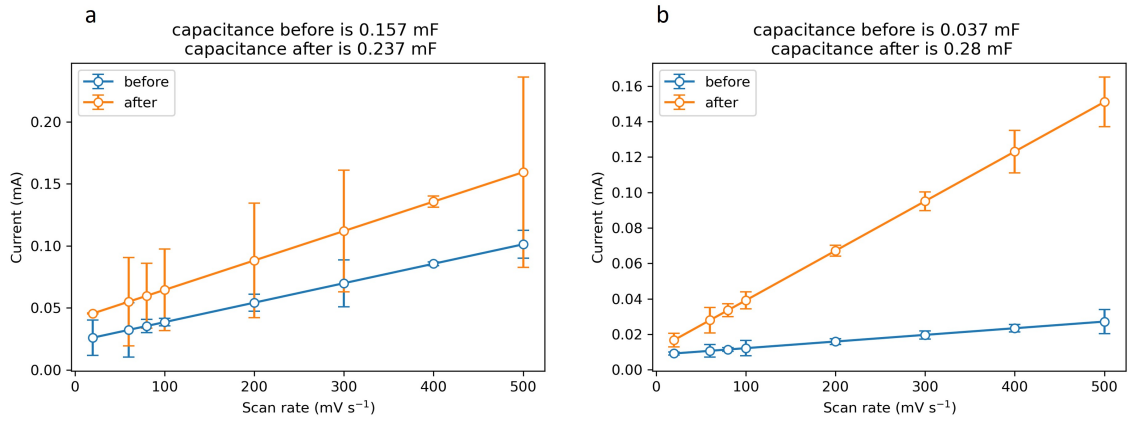

Figure 4.16: a) Bare Cu positive current vs scan rate (mV s^{-1}) for. b) Naf/Cu positive current vs scan rate (mV s^{-1}).

For the Naf/Cu sample the capacitance increased about 6.5 fold, from 0.037 to 0.28 mF. The capacitance before is relatively low, also when compared to the bare Cu samples. We suspect this low capacity is assumed to be due to the orientation of the ionomer, where before negative conditioning of the electrode, the hydrophobic backbone is oriented towards the copper surface. This results in less surface charge on the copper surface. After the experiment, the surface charge increased significantly as shown by the increased capacitance of 0.28 mF. We propose that the ionomer restructuring, observed from AFM, results in reorientation of the ionomer where the hydrophilic domains face the electrode surface instead of the hydrophobic backbone initially before negatively conditioning the electrode. This change results in an increased surface charge due to the accessibility of the hydrochannels of the ionomer layer to the copper surface.

The capacitance measurements can be used to calculate the 'electrochemical active surface area', or ECSA. Taking the capacitance of bare Cu before testing as a reference to calculate the specific capacitance, the normalized 'active surface areas' of the other samples can be calculated. So dividing the capacitance of bare Cu before testing (0.157 mF) by the geometric surface area of the electrode (2.25 cm^2), gives the normalized specific capacitance 0.07 mF cm^{-2}. In table 4.1 the capacitances and

normalized active surface areas are shown. These electrochemical active surface areas are used to calculate the intrinsic activities in chapter 4.4.

We should note that the capacitances measurements are calculated using a single dataset, separate from the actual CO_2R experiments from which product distributions were determined, which questions its reliability. Nevertheless, the strong difference in capacitance observed with the Naf/Cu gives a solid indication about an increasing surface charge during CO_2R.

Table 4.1: This table shows the capacitance of bare Cu and Naf/Cu before and after 1 hour chronoamperometry at -1.9V vs Ag/AgCl reference electrode.

Sample	Capacitance [mF]	Electrochemical active surface area [cm^2]
Bare Cu before	0.157	2.25
Bare Cu after	0.237	3.39
Naf/Cu before	0.037	0.53
Naf/Cu after	0.28	4.00

5

Conclusion

This thesis aimed at elucidating the ionomer-catalyst interfacial interactions, and its effect on electrochemical CO_2R performance. Specifically Nafion and copper were used, both promising materials for electrochemical CO_2R. To answer the research questions in the introduction, three experimental approaches have been used 1) AFM, 2) ATR-SEIRAS, 3) CO_2R experiments.

The dynamical change in ionomer thin film morphology during CO_2R was investigated using in-situ AFM. Applying a negative polarization on copper, resulted in significant reorganization of the nafion thin film morphology. Firstly, the morphology of the bare copper surface was investigated. Negatively polarizing the copper, resulted in a rougher copper surface, which is consistent with findings by other researchers [69–71]. Deposition of the ionomer and subsequent exposure to the electrolyte resulted in minor changes to the ionomer morphology, which is proposed to be due to swelling effects. Applying a negative polarization to the copper surface, resulted in a smoother surface, in contrast with bare copper. Since the hydrophilicity of the copper surface increases due to electrowetting, it is suspected that the interaction with the phase-separated hydrophilic part of the ionomer becomes stronger during CO_2R. This results in more a parallel orientation of the ionomer backbone relative to the copper surface. From the relative double layer capacitance measurements in chapter 4.6, the surface charge before negatively conditioning the electrode was much lower than after the CO_2R conditions. This is confirms the hypothesis that the ionomer's hydrophobic backbone first dominated the interactions with the catalyst, and after reorganization the hydrophilic domain faced the catalyst surface. Due to confinementment effects, expected from the estimated thickness of the thin film of 20-30 nm, reorganization of the ionomers results in a smoother surface, which has been observed on the micro- to nanoscale with AFM.

The effect of the ionomer on the local reaction environment was investigated with ATR SEIRAS. The addition of the ionomer resulted in a clear increase in absorbance of the $*CO_{ad}$ reaction intermediate. Two forms of the $*CO_{ad}$ intermediate were identified, atop-CO and bridged-CO, of which the both increased significantly with the addition of the ionomer. According to other research, the bridged-CO is a relatively inert species, and does not contribute to CO_2R. From the reverse scan from -1.1 to 0 V in the heatmaps (figures 4.9a,b) the intensity of the bridged-CO barely declines. This supports the assertion that bridged-CO is not an active species in CO_2R. The band between 2100-2000 cm^{-1}, corresponding to atop-CO, showed increased absorbance at high potentials. This indicates that the ionomer stabilizes this intermediate at these potentials. Stabilization of the atop-CO intermediate, explains the increased formation of the successive products CO, CH_4 and C_2H_4 evident from chapter 4.3. We propose three hypotheses that explain this stabilization of *CO:

Firstly, desorped gaseous products could experience increased mass transfer resistance through the membrane, compared to the aqueous bulk [6, 47]. The permeability of CO in Nafion is 7.3 times lower than in water, hence could lead to accumulation of CO(g) among other gasses. Accumulation could lead to more re-adsorption, which in turn could lead to a higher coverage of *CO on the copper surface (see figure 5.1). This higher coverage could allow for more C-C coupling and lead to higher ethylene yield, or alternatively could result in more methane formation.

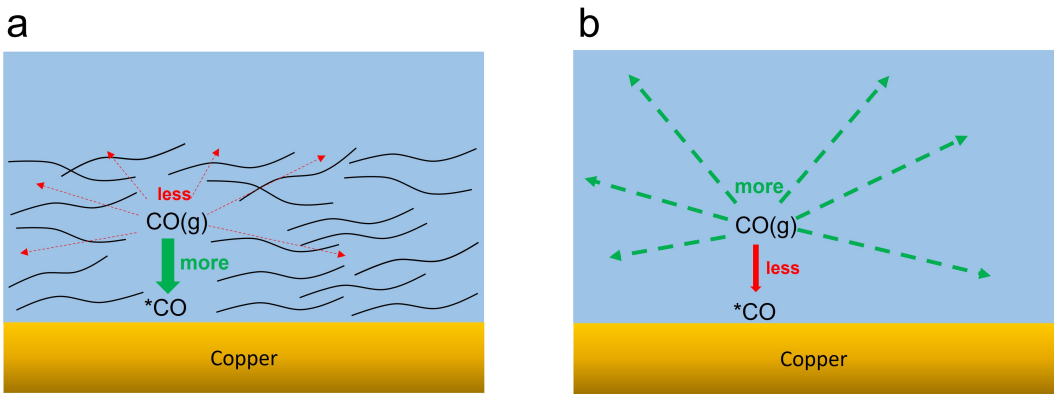

Figure 5.1: a) This figure shows how the ionomer limits CO permeability, which could lead to re-adsorption of CO. b) Case for bare copper

Secondly, the sulfonate groups, accompanied by cations, could influence CO_2R. It is well established that cations influence and stabilize CO_2R intermediates [10, 15, 72]. The presence of the sulfonate groups in Nafion introduces more cations into the local reaction environment to maintain electro-neutrality. A higher cation concentration could enhance stabilization of the *CO intermediate and explain the observations of increased yields of ethylene, methane and carbon monoxide (see figure 5.2). Resasco *et al.* [15] found that adsorbed species with large dipole moments, are stabilized by electrostatic interactions with solvated cations and it thus in line with our argumentation. Furthermore, the double layer capacitance measurements show that the surface charge of the Naf/Cu is higher than the bare

Cu after CO_2R. This suggests that the Nafion introduces more surface charge, which could be due to the cations accompanying the sulfonate groups.

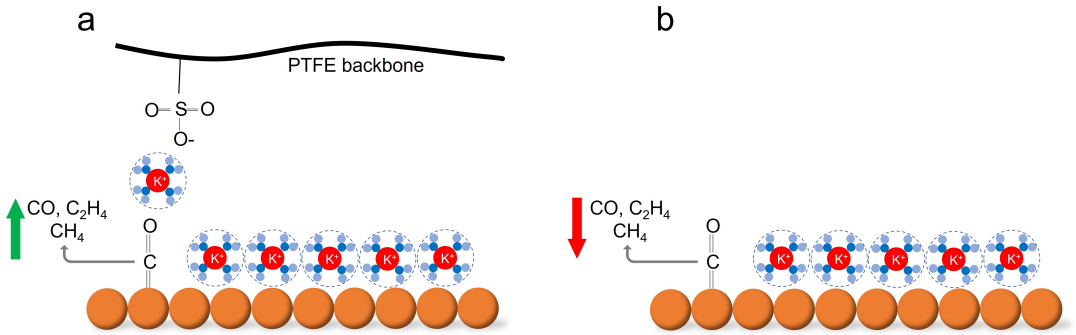

Figure 5.2: a) This figure shows how an increased cation concentration could stabilize the *CO. b) Case for bare copper.

Thirdly, a dipole-dipole bond between the sulfonate group on the Nafion and the *CO intermediate could form. Both the *CO and the SO_3^- group have dipole moments due to the difference in electronegativity of the atoms. The *CO and SO_3^- could form dipole-dipole interactions, which would result in stabilization of the *CO intermediate and higher yields of resulting products (see figure 5.3). Pan & Barile [7] suggested something similar, where they proposed Nafion interacts via hydrogen bonds with the *CO intermediate.

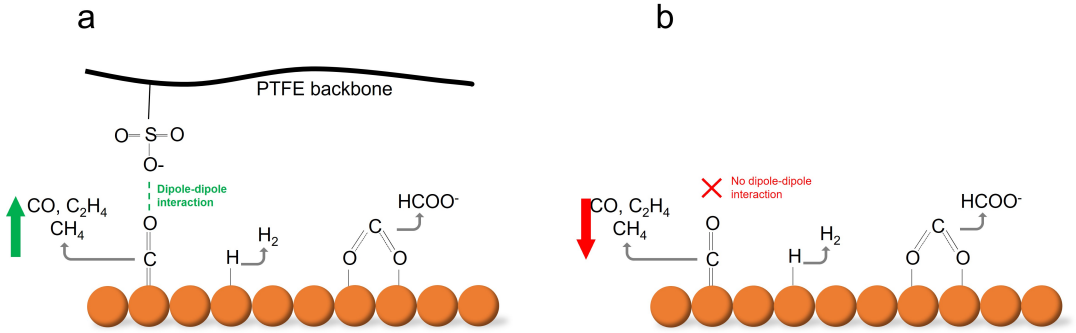

Figure 5.3: a) illustrates the proposed stabilization of Nafion of *CO intermediate with dipole-dipole bonds. b) Shows how bare copper results in a lower activity towards CO, C_2H_4 and CH_4.

Besides increased ethylene and carbon monoxide formation, methane was also promoted by the ionomer. Previous studies suggested that methane formation is pH-dependent and favored at lower pH values [85, 86]. The slightly acidic pH of 6.8 of CO_2-saturated 0.1 M $KHCO_3$, explains the relatively high formation of methane compared to ethylene which is favored at a higher pH [16, 87]. The higher methane formation effected by the ionomer, can also be attributed to the stabilization of the *CO intermediate. Furthermore the ionomer did not affect the activity towards hydrogen and formate. In essence, the ionomer resulted in additional formation of carbon monoxide, methane and ethylene in contrast with a similar formation of hydrogen and formate. In table 5.1 a comparison between bare Cu and Naf/Cu on products distribution is shown.

Table 5.1: Comparison of product distribution on bare Cu and Naf/Cu.

Product	Bare Cu	Naf/Cu
H_2	+	-
CO	-	+
C_2H_4	-	++
CH_4	-	+
$HCOO^-$	+	-

To conclude, we used a multifaceted experimental approach, with which we showed the Nafion ionomer promotes formation towards ethylene, a promising candidate product for industrial scale CO_2R. During CO_2R we observed significant reorganization of the ionomer layer, were hydrophilic interactions between the copper surface and sulfonate groups of Nafion are expected to be dominant. The Nafion stabilizes the *CO intermediate, for which three the proposed mechanisms are suggested. Figure 5.2 and 5.3 show two plausible *CO stabilization mechanisms, whereas the proposition in figure 5.1 suggests a higher re-adsorption of CO due to a lower permeability of CO(g) in the Nafion layer compared to water. These proposed mechanisms allow for a higher degree of *CO coverage on the copper surface and subsequently more C-C coupling, which explain the enhanced C_{2+} formation shown by the CO_2R experiments in chapter 4.3. With the insights gained in this thesis we elucidated the interactions between the ionomer and catalyst during electrochemical CO_2R, which relates to the fundamental understanding required for designing advanced catalyst layers in the gas diffusion electrode.

5.1. Recommendations

What follows is a list of recommendations for further investigation into the ionomer-catalyst interfacial interactions, with the aim to improve the current methodology used in this research.

- Compare a lower equivalent weight PFSA ionomer, like the one from 3M, with Nafion. The higher amount of sulfonate groups relative to the backbone, should result in even more stabilization, hence it challenges the proposition of the stabilization of the intermediate by the ionomer.
- Compare Nafion with different ionomers, including anion-exchange membranes like Sustainion. The difference in chemistry of other ionomers would result in different effects. Stacking of ionomer layers would be another interesting topic to look into, to promote C_{2+} formation even more.
- Performing ion chromatography to quantitatively determine ionomer degradation. In this thesis, XPS served only as a qualitative method for determining ionomer degradation, where a method like ionomer chromatography enables quantification.
- Look into the effect of different Cu crystal facets. The crystal facets were not investigated in this thesis, but it would be interesting to see how the different crystal facets interact with the ionomer. Gregorio *et al.* [88] showed how different Cu crystals result in dramatic difference in product selectivity, which could be combined with ionomers to enhance C_{2+} yields even more.

References

1. REN21. *Renewables 2021 Global Status Report* (2021).
2. IPCC. *Climate Change 2021: The Physical Science Basis* (2021).
3. Lee, M.-Y. *et al.* Current achievements and the future direction of electrochemical CO2 reduction: A short review. *Critical Reviews in Environmental Science and Technology* **50,** 769–815 (2020).
4. Lees, E. W., Mowbray, B. A., Parlane, F. G. & Berlinguette, C. P. Gas diffusion electrodes and membranes for CO2 reduction electrolysers. *Nature Reviews Materials 2021,* 1–10 (2021).
5. Jouny, M., Luc, W. & Jiao, F. General Techno-Economic Analysis of CO 2 Electrolysis Systems (2018).
6. Kim, C. *et al.* Tailored catalyst microenvironments for CO2 electroreduction to multicarbon products on copper using bilayer ionomer coatings. *Nature Energy 2021 6:11* **6,** 1026–1034 (11 2021).
7. Pan, H. & Barile, C. J. Electrochemical CO2 reduction to methane with remarkably high Faradaic efficiency in the presence of a proton permeable membrane. *Energy Environ. Sci.* **13,** 3567–3578 (10 2020).
8. De Arquer, F. P. G. *et al.* CO2 electrolysis to multicarbon products at activities greater than 1 A cm-2. *Science* **367,** 661–666 (2020).
9. Daintith, J. *Le Chatelier's principle* 2008.
10. Garg, S. *et al.* Advances and challenges in electrochemical CO 2 reduction processes: an engineering and design perspective looking beyond new catalyst materials. *Journal of Materials Chemistry A* **8,** 1511–1544 (4 2020).
11. Hu, L. *et al.* Tunable Selectivity and High Efficiency of CO2 Electroreduction via Borate-Enhanced Molten Salt Electrolysis. *iScience* **23,** 101607 (2020).
12. Razaghi, M. & Khorasani, M. Boosting the quaternary ammonium halides catalyzed CO2 coupling with epoxides on the hollow mesoporous silica sphere. *Journal of CO2 Utilization* **61,** 102028 (2022).
13. Kortlever, R., Tan, K., Kwon, Y. & Koper, M. Electrochemical carbon dioxide and bicarbonate reduction on copper in weakly alkaline media. *Journal of Solid State Electrochemistry* **17,** 1843 (2013).
14. Hong, S., Lee, S., Kim, S., Lee, J. K. & Lee, J. Anion dependent CO/H2 production ratio from CO2 reduction on Au electro-catalyst. *Catalysis Today* **295.** Water at Interfaces, 82–88 (2017).
15. Resasco, J. *et al.* Promoter Effects of Alkali Metal Cations on the Electrochemical Reduction of Carbon Dioxide. *Journal of the American Chemical Society* **139,** 11277–11287 (32 2017).
16. Nitopi, S. *et al.* Progress and Perspectives of Electrochemical CO2 Reduction on Copper in Aqueous Electrolyte. *Chemical Reviews* **119,** 7610–7672 (12 2019).
17. Burdyny, T. & Smith, W. A. CO2 reduction on gas-diffusion electrodes and why catalytic performance must be assessed at commercially-relevant conditions. *Energy & Environmental Science* **12,** 1442–1453 (5 2019).
18. Buchanan, B. & Wong, J. A conversation with Andrew Benson: Reflections on the discovery of the Calvin-Benson cycle. *Photosynthesis research* **114** (2012).
19. Yamada, H. Amine-based capture of CO2 for utilization and storage. *Polymer Journal 2020 53:1* **53,** 93–102 (1 2020).
20. Engel, T. *Physical chemistry / Thomas Engel, Philip Reid.* Third edition, Pearson New International Edition. eng (Pearson Education Limited, Harlow, Essex, 2014).

21. Jiang, H. *et al.* The anolyte matters: Towards highly efficient electrochemical CO2 reduction. *Chemical Engineering Journal* **422,** 129923 (2021).
22. Monteiro, M. C., Philips, M. F., Schouten, K. J. P. & Koper, M. T. Efficiency and selectivity of CO2 reduction to CO on gold gas diffusion electrodes in acidic media. *Nature Communications 2021 12:1* **12,** 1–7 (1 2021).
23. Vass, Á., Kormányos, A., Kószo, Z., Endrődi, B. & Janáky, C. Anode Catalysts in CO2 Electrolysis: Challenges and Untapped Opportunities. *ACS Catalysis* **12,** 1037–1051 (2 2022).
24. Hori, Y., Kikuchi, K. & Suzuki, S. Production of CO and CH4 in electrochemical reduction of CO2 at metal electrodes in aqueous hydrogencarbonate solution. *Chemistry Letters* **14,** 1695–1698 (11 1985).
25. Yin, Z. *et al.* An alkaline polymer electrolyte CO2 electrolyzer operated with pure water. *Energy Environ. Sci.* **12,** 2455–2462 (8 2019).
26. Salvatore, D. A. *et al.* Designing anion exchange membranes for CO2 electrolysers. *Nature Energy 2021 6:4* **6,** 339–348 (4 2021).
27. Nesbitt, N. T. *et al.* Liquid-Solid Boundaries Dominate Activity of CO2Reduction on Gas-Diffusion Electrodes. *ACS Catalysis* **10,** 14093–14106 (23 2020).
28. Kuo, L. & Dinh, C. T. Toward efficient catalysts for electrochemical CO2 conversion to C2 products. *Current Opinion in Electrochemistry* **30,** 100807 (2021).
29. Ni, Z. *et al.* Research progress of electrochemical CO2 reduction for copper-based catalysts to multicarbon products. *Coordination Chemistry Reviews* **441,** 213983 (2021).
30. Xing, Z., Shi, K., Hu, X. & Feng, X. Beyond catalytic materials: Controlling local gas/liquid environment in the catalyst layer for CO2 electrolysis. *Journal of Energy Chemistry* **66,** 45–51 (2022).
31. Popović, S. *et al.* Stability and Degradation Mechanisms of Copper□Based Catalysts for Electrochemical CO 2 Reduction. *Angewandte Chemie* **132,** 14844–14854 (35 2020).
32. Ye, W., Guo, X. & Ma, T. A review on electrochemical synthesized copper-based catalysts for electrochemical reduction of CO2 to C2+ products. *Chemical Engineering Journal* **414,** 128825 (2021).
33. Rutkowska, I. A. *et al.* Elucidation of activity of copper and copper oxide nanomaterials for electrocatalytic and photoelectrochemical reduction of carbon dioxide. *Current Opinion in Electrochemistry* **23.** Electrocatalysis ● Sensors and Biosensors, 131–138 (2020).
34. Simon, G. H., Kley, C. S. & Cuenya, B. R. Potential-Dependent Morphology of Copper Catalysts During CO2 Electroreduction Revealed by In Situ Atomic Force Microscopy. *Angewandte Chemie - International Edition* **60,** 2561–2568 (5 2021).
35. Grosse, P. *et al.* Dynamic transformation of cubic copper catalysts during CO2 electroreduction and its impact on catalytic selectivity. *Nature Communications 2021 12:1* **12,** 1–11 (1 2021).
36. Bagger, A., Ju, W., Varela, A. S., Strasser, P. & Rossmeisl, J. Electrochemical CO2 Reduction: A Classification Problem. *ChemPhysChem* **18,** 3266–3273 (22 2017).
37. Peterson, A. A., Abild-Pedersen, F., Studt, F., Rossmeisl, J. & Nørskov, J. K. How copper catalyzes the electroreduction of carbon dioxide into hydrocarbon fuels. *Energy and Environmental Science* **3,** 1311–1315 (9 2010).
38. Kortlever, R., Shen, J., Schouten, K. J. P., Calle-Vallejo, F. & Koper, M. T. Catalysts and Reaction Pathways for the Electrochemical Reduction of Carbon Dioxide. *Journal of Physical Chemistry Letters* **6,** 4073–4082 (20 2015).
39. Wan, Q. *et al.* Boosting the faradaic efficiency for carbon dioxide to monoxide on a phthalocyanine cobalt based gas diffusion electrode to higher than 99% via microstructure regulation of catalyst layer. *Electrochimica Acta* **392,** 139023 (2021).
40. Zeng, J., Fontana, M., Sacco, A., Sassone, D. & Pirri, C. F. A study of the effect of electrode composition on the electrochemical reduction of CO2. *Catalysis Today* (2021).
41. Chen, Y. *et al.* The effect of catholyte and catalyst layer binders on CO2 electroreduction selectivity. *Chem Catalysis* **2,** 400–421 (2022).

42. Koshy, D. M. *et al.* Chemical Modifications of Ag Catalyst Surfaces with Imidazolium Ionomers Modulate H2 Evolution Rates during Electrochemical CO2 Reduction. *Journal of the American Chemical Society* **143.** PMID: 34472346, 14712–14725 (2021).
43. Guzmán, H. *et al.* Investigation of Gas Diffusion Electrode Systems for the Electrochemical CO2 Conversion. *Catalysts* **11** (2021).
44. Puring, K. J. *et al.* Electrochemical CO2 Reduction: Tailoring Catalyst Layers in Gas Diffusion Electrodes. *Advanced Sustainable Systems* **5,** 2000088 (1 2021).
45. Yang, H., Kaczur, J. J., Sajjad, S. D. & Masel, R. I. Electrochemical conversion of CO2 to formic acid utilizing Sustainion™ membranes. *Journal of CO2 Utilization* **20,** 208–217 (2017).
46. Kutz, R. B. *et al.* Sustainion Imidazolium-Functionalized Polymers for Carbon Dioxide Electrolysis. *Energy Technology* **5,** 929–936 (6 2017).
47. Kusoglu, A. & Weber, A. Z. New Insights into Perfluorinated Sulfonic-Acid Ionomers. *Chemical Reviews* **117,** 987–1104 (3 2017).
48. Shin, S. H. *et al.* Improving the Mechanical Durability of Short-Side-Chain Perfluorinated Polymer Electrolyte Membranes by Annealing and Physical Reinforcement. *ACS Omega* (2019).
49. Fujinami, S. *et al.* Morphological changes of hydrophobic matrix and hydrophilic ionomers in water-swollen perfluorinated sulfonic acid membranes detected using small-angle X-ray scattering. *Polymer* **180,** 121699 (2019).
50. Xie, J. *et al.* Influence of ionomer content on the structure and performance of PEFC membrane electrode assemblies. *Electrochimica Acta* **55,** 7404–7412 (24 2010).
51. Kaddouri, A. E., Flandin, L. & Bas, C. Chemical degradation of PFSA ionomer binder in PEMFC's catalyst layer. *International Journal of Hydrogen Energy* **43,** 15386–15397 (32 2018).
52. Andersen, S. M. Nano carbon supported platinum catalyst interaction behavior with perfluorosulfonic acid ionomer and their interface structures. *Applied Catalysis B: Environmental* **181,** 146–155 (2016).
53. Hernandez-Aldave, S. & Andreoli, E. Fundamentals of Gas Diffusion Electrodes and Electrolysers for Carbon Dioxide Utilisation: Challenges and Opportunities. *Catalysts 2020, Vol. 10, Page 713* **10,** 713 (6 2020).
54. Allen, F. I. *et al.* Morphology of Hydrated As-Cast Nafion Revealed through Cryo Electron Tomography. *ACS Macro Letters* **4.** PMID: 35596390, 1–5 (2015).
55. Gebel, G., Aldebertt, P. & Pineri, M. Swelling study of perfluorosulphonated ionomer membranes (1993).
56. Collette, F. M., Lorentz, C., Gebel, G. & Thominette, F. Hygrothermal aging of Nafion®. *Journal of Membrane Science* **330,** 21–29 (2009).
57. Kusoglu, A., Kienitz, B. & Weber, A. Understanding the Effects of Compression and Constraints on Water Uptake of Fuel-Cell Membranes. *Journal of the Electrochemical Society* **158,** B1504–B1514 (2011).
58. Ogata, Y. *et al.* Impact of the Solid Interface on Proton Conductivity in Nafion Thin Films. *Langmuir* **34,** 15483–15489 (50 2018).
59. Kusoglu, A., Dursch, T. J. & Weber, A. Z. Nanostructure/Swelling Relationships of Bulk and Thin-Film PFSA Ionomers. *Advanced Functional Materials* **26,** 4961–4975 (27 2016).
60. Kusoglu, A. *et al.* Impact of Substrate and Processing on Confinement of Nafion Thin Films. *Advanced Functional Materials* **24,** 4763–4774 (30 2014).
61. Kushner, D. I. *et al.* Substrate-Dependent Molecular and Nanostructural Orientation of Nafion Thin Films. *Advanced Functional Materials* **29,** 1902699 (37 2019).
62. Paul, D. *Structure and Properties of Self-Assembled Sub-Micron Thin Nafion® Films* (Queen's University, 2013).
63. Berlinger, S. A., McCloskey, B. D. & Weber, A. Z. Probing Ionomer Interactions with Electrocatalyst Particles in Solution. *ACS Energy Letters* **6,** 2275–2282 (6 2021).

64. Katayama, Y. *et al.* An in Situ Surface-Enhanced Infrared Absorption Spectroscopy Study of Electrochemical CO2 Reduction: Selectivity Dependence on Surface C-Bound and O-Bound Reaction Intermediates. *Journal of Physical Chemistry C* **123,** 5951–5963 (10 2019).

65. Corson, E. R. *et al.* In Situ ATR–SEIRAS of Carbon Dioxide Reduction at a Plasmonic Silver Cathode. *Journal of the American Chemical Society* **142.** PMID: 32469508, 11750–11762 (2020).

66. Zhu, S., Li, T., Cai, W. B. & Shao, M. CO2 Electrochemical Reduction As Probed through Infrared Spectroscopy. *ACS Energy Letters* **4,** 682–689 (3 2019).

67. NL, T. F. S. .-. *X-Ray Photoelectron Spectroscopy | Thermo Fisher Scientific - NL*

68. Kusoglu, A. & Weber, A. Z. New Insights into Perfluorinated Sulfonic-Acid Ionomers. *Chemical Reviews* **117,** 1000 (3 2017).

69. Kim, Y. G., Baricuatro, J. H. & Soriaga, M. P. Surface Reconstruction of Polycrystalline Cu Electrodes in Aqueous KHCO3 Electrolyte at Potentials in the Early Stages of CO2 Reduction. *Electrocatalysis* **9,** 526–530 (4 2018).

70. Huang, J. *et al.* Potential-induced nanoclustering of metallic catalysts during electrochemical CO2 reduction. *Nature Communications 2018 9:1* **9,** 1–9 (1 2018).

71. Velasco-Velez, J. J. *et al.* Revealing the Active Phase of Copper during the Electroreduction of CO2in Aqueous Electrolyte by Correlating in Situ X-ray Spectroscopy and in Situ Electron Microscopy. *ACS Energy Letters* **5,** 2106–2111 (6 2020).

72. Bui, J. C. *et al.* Engineering Catalyst-Electrolyte Microenvironments to Optimize the Activity and Selectivity for the Electrochemical Reduction of CO2on Cu and Ag. *Accounts of Chemical Research* **55,** 484–494 (4 2022).

73. Li, M. *et al.* The role of electrode wettability in electrochemical reduction of carbon dioxide. *Journal of Materials Chemistry A* **9,** 19369–19409 (35 2021).

74. Papasizza, M. & Cuesta, A. In Situ Monitoring Using ATR-SEIRAS of the Electrocatalytic Reduction of CO2 on Au in an Ionic Liquid/Water Mixture. *ACS Catalysis* **8,** 6345–6352 (7 2018).

75. Braunschweig, B., Mukherjee, P., Haan, J. L. & Dlott, D. D. Vibrational sum-frequency generation study of the CO2 electrochemical reduction at Pt/EMIM-BF4 solid/liquid interfaces. *Journal of Electroanalytical Chemistry* **800.** Special Issue in honor of Masatoshi Osawa, 144–150 (2017).

76. Zhu, S., Jiang, B., Cai, W. B. & Shao, M. Direct Observation on Reaction Intermediates and the Role of Bicarbonate Anions in CO2 Electrochemical Reduction Reaction on Cu Surfaces. *Journal of the American Chemical Society* **139,** 15664–15667 (44 2017).

77. Hori, Y., Murata, A., Takahashi, R. & Suzuki, S. Electrochemical Reduction of Carbon Monoxide to Hydrocarbons at Various Metal Electrodes in Aqueous Solution. *Chemistry Letters* **16,** 1665–1668 (1987).

78. Durand, W. J., Peterson, A. A., Studt, F., Abild-Pedersen, F. & Nørskov, J. K. Structure effects on the energetics of the electrochemical reduction of CO2 by copper surfaces. *Surface Science* **605,** 1354–1359 (2011).

79. Gunathunge, C. M., Ovalle, V. J., Li, Y., Janik, M. J. & Waegele, M. M. Existence of an Electrochemically Inert CO Population on Cu Electrodes in Alkaline pH. *ACS Catalysis* **8,** 7507–7516 (8 2018).

80. Sethuraman, V. A., Khan, S., Jur, J. S., Haug, A. T. & Weidner, J. W. Measuring oxygen, carbon monoxide and hydrogen sulfide diffusion coefficient and solubility in Nafion membranes. *Electrochimica Acta* **54,** 6850–6860 (2009).

81. *Solubility of Gases in Water vs. Temperature*

82. Moradzaman, M. & Mul, G. Infrared Analysis of Interfacial Phenomena during Electrochemical Reduction of CO 2 over Polycrystalline Copper Electrodes (2020).

83. Hanawa, H., Kunimatsu, K., Watanabe, M. & Uchida, H. In situ ATR-FTIR analysis of the structure of Nafion-Pt/C and Nafion-Pt 3Co/C interfaces in fuel cell. *Journal of Physical Chemistry C* **116,** 21401–21406 (40 2012).

84. Wei, J. *et al.* Heterostructured Electrocatalysts for Hydrogen Evolution Reaction Under Alkaline Conditions. *Nano-Micro Letters* **10,** 1–15 (4 2018).

85. Schouten, K. J. P., Gallent, E. P. & Koper, M. T. The influence of pH on the reduction of CO and CO2 to hydrocarbons on copper electrodes. *Journal of Electroanalytical Chemistry* **716,** 53–57 (2014).

86. Kas, R. *et al.* Manipulating the Hydrocarbon Selectivity of Copper Nanoparticles in CO2 Electroreduction by Process Conditions. *ChemElectroChem* **2,** 354–358 (3 2015).

87. Deng, B., Huang, M., Zhao, X., Mou, S. & Dong, F. Interfacial Electrolyte Effects on Electrocatalytic CO2 Reduction. *ACS Catalysis* **12,** 331–362 (1 2022).

88. Gregorio, G. L. D. *et al.* Facet-Dependent Selectivity of Cu Catalysts in Electrochemical CO2 Reduction at Commercially Viable Current Densities. *ACS Catalysis* **10,** 4854–4862 (9 2020).

6 Appendix

6.1. NMR spectra

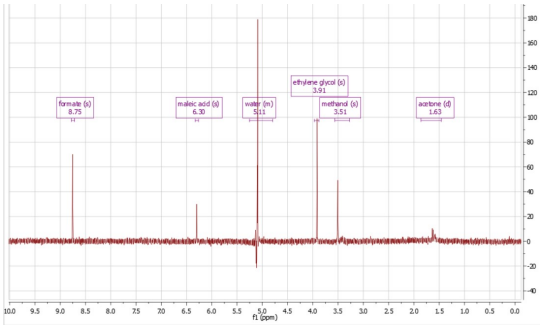

(a) NMR spectrum of bare Cu sample belonging to the -0.9 V vs RHE averaged potential.

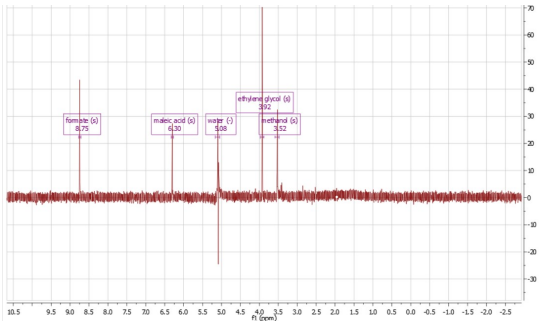

(b) NMR spectrum of Naf/Cu sample belonging to the -0.88 V vs RHE averaged potential.

Figure 6.1: NMR spectra

6.2. XPS

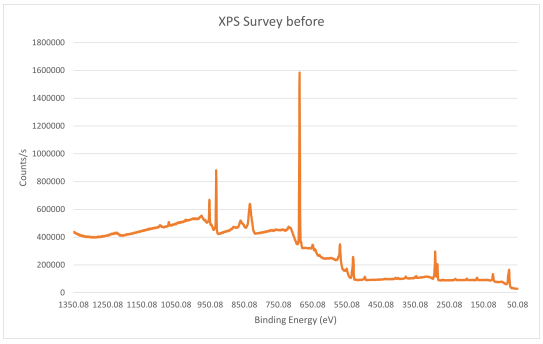

(a) XPS survey of Naf/Cu sample before CO_2R in flow cell.

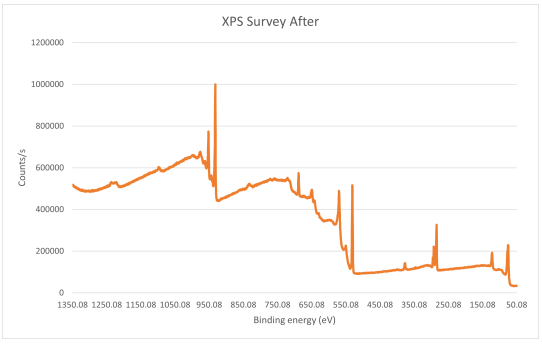

(b) XPS survey of Naf/Cu sample after CO_2R in flow cell.

Figure 6.2: XPS surveys

6.3. Cyclic voltammetry

In figure 6.3 the cyclic voltammetry (CV) measurement of both samples is shown. The CV was performed before the chronoamperometry measurements. The onset potential is around -0.4V for both

samples. Here the Naf/Cu has a slightly higher current density (more negative) than Cu. This can be attributed to the high proton-conductivity of Nafion.

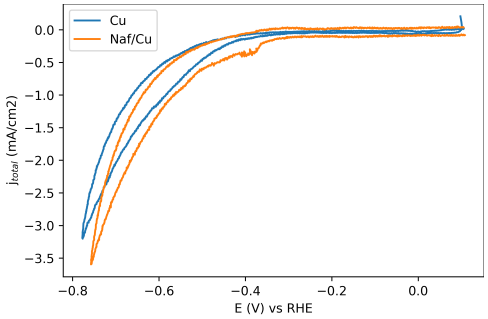

Figure 6.3: Cyclic voltammetry averaged for bare and the ionomer coated copper.

6.4. EIS measurements

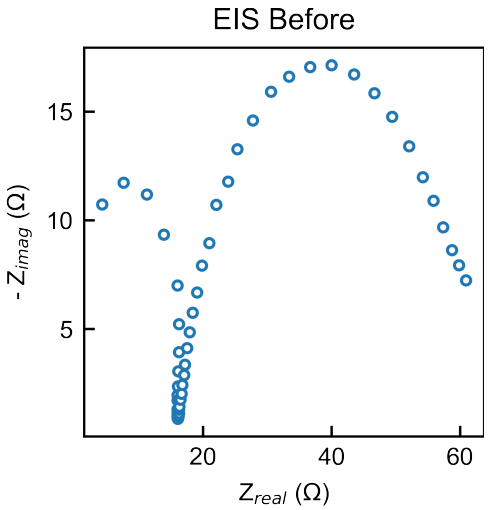

Figure 6.4: EIS measurement. Solution resistances were typically between 15 and 25 ohms, both both Naf/Cu as well as